Sizing of Non-Carbonaceous Nanoparticles by Time-Resolved Laser-Induced Incandescence

by

Timothy A. Sipkens

A thesis
presented to the University of Waterloo
in fulfillment of the
thesis requirement for the degree of
Masters of Applied Science
in
Mechanical Engineering

Waterloo, Ontario, Canada, 2014

Author's Decleration

I hereby declare that I am the sole author of this thesis. This is a true copy of the thesis, including any required final revisions, as accepted by my examiners.

I understand that my thesis may be made electronically available to the public.

Abstract

Non-carbonaceous nanoparticles represent a growing field in science and technology. Their applications range from medicine to environmental remediation to information technology. As the functionality of nanoparticles in these roles is highly size dependent, it is critical that diagnostics be developed to accurately measure the size of these nanoparticles. Time-resolved laser-induced incandescence (TiRe-LII) is an *in situ* technique that can measure the size of nanoparticles without physically probing a system. The technique operates using a laser pulse that heats the nanoparticle to incandescent temperatures. The incandescence is then measured from the nanoparticles as they equilibrate with the surrounding gas. As smaller particles will cool more quickly, the size of the nanoparticles can be inferred by modeling the incandescence or, more commonly, the effective temperature decay of the nanoparticles.

The present work summarizes attempts to extend the use of TiRe-LII from its original application on soot to non-carbonaceous particles. This will be done by examining experimental data from three non-carbonaceous nanoparticles: molybdenum, silicon, and iron. This includes descriptions of the TiRe-LII models and statistical techniques required to robustly infer parameters and their uncertainties. As one of the major setbacks in extending this technique to other materials is the determination of the thermal accommodation coefficient (TAC), this work also focusses on determining that parameter both from experimental data and molecular dynamics simulations.

Acknowledgements

I would firstly like to thank my supervisor, Dr. Kyle Daun, for his insights. In particular, I would like to thank him for his support and understanding in the latter part of the completion of this degree.

I would also like to acknowledge my collaborators the Center of Nanointegration Duisburg-Essen for their support during the times I spent there. The work on silicon presented herein was done with a considerable amount of help from their staff. I would like to particularly thank Raphael Mansmann and Nils Petermann for their active work on the reactor, both during the around the time I spent at the University of Duisburg-Essen. I would also like to thank Dr. Thomas Drier, Dr. Christof Schultz, and Dr. Hartmund Wiggers for their insights during those same periods.

I would also like to thank Dr. Mikko Karttunen and Dr. John Titantah for their support in the molecular dynamics work. It was their direct efforts that provided us with interatomic potentials derived from density functions theory (DFT) used in the present work.

I would also like to acknowledge Dr. Yoshiaki Murakami for lending us use of his experimental TiRe-LII molybdenum data for reanalysis.

I would like to thank Nigel Singh for his help in completing the iron experiments contained in this work. This work would not have been nearly as effective without his laboratory expertise.

I would like to thank my readers, Dr. Kyle Daun, Dr. Sean Peterson, and Dr. John Wen, for their time and insight as well as their positive feedback.

Finally, I would also like to thank my family, colleagues (including Joshua Rasera, Matthew Twynstra, Farzan Memarian, Noel Chester, Nigel Singh, Kamalpreet Jhajj, Roger Tsang, Sam Grauer, Natalie Field, Jeff Hou, Jeff Labahn, Dominic Ma, and Daniele Dovizio), and Starbucks (including their baristas) for their support throughout the progression of this degree.

Table of Contents

List of Figures

List of Tables

Nomenclature

Latin Symbols

Symbol	Unit	Definition
a	eV	QCSC potential parameter
A	-	SW potential parameter
b	-	Observed data
B	-	SW potential parameter
c	nm	EAM potential parameter
C	Pa	Clausius-Clapeyron material constant
$c_{g,t}$	$m \cdot s^{-1}$	Mean thermal speed of gas molecules
$c_{v,t}$	$m \cdot s^{-1}$	Mean thermal speed of vapor molecules
c_o	$m \cdot s^{-1}$	Speed of light in a vacuum, 3.00e8
c_p	$J \cdot kg^{-1} \cdot K^{-1}$	Specific heat capacity
c_v	$m \cdot s^{-1}$	Thermal speed of evaporating atoms
c_0, c_1, c_2	-	FS pairwise potential parameters
$C_2(t_i)$	-	Fitting parameter in spectral incandescence
d	nm	FS electron density function parameter
D	-	Diffusion coefficient
D	meV	Potential well depth
d_p	nm	Particle diameter
$d_{p,g}$	nm	Geometric mean particle diameter
$d_{p,32}$	nm	Sauter mean diameter
E	J	Energy

E_i	J	Pre-collision energy of gas molecule
E_o	J	Post-collision energy of gas molecule
$E(\mathbf{m}_\lambda)$	-	Complex absorption function
h	J·s	Planck's constant, 6.626e−34
Δh_v	$J \cdot atom^{-1}$	Enthalpy of vaporization
$\Delta h_{v,b}$	$J \cdot atom^{-1}$	Enthalpy of vaporization at the boiling point
$I_{b,\lambda}$	W	Blackbody radiation at wavelength λ
J_λ	a.u.	Incandescence at wavelength λ
$K(d_p,t)$	-	Kernal of integral equation
K	$J \cdot atom^{-1}$	Material constant in Waton's equation
k_B	$J \cdot molecule^{-1} \cdot K^{-1}$	Boltzmann constant, 1.38e-23
Kn	-	Knudsen number
K_{opt}	-	Optical inefficiencies in pyrometric temperature
L	nm	Length scale
m	-	QCSC potential parameter
m_g	$kg \cdot molecule^{-1}$	Molecular mass of a gas molecule
m_s	$kg \cdot atom^{-1}$	Mass of a surface atom
m_v	$kg \cdot atom^{-1}$	Mass of vapor atoms
M_v	$kg \cdot mol^{-1}$	Molar mass of vapor
$\mathbf{m}_\lambda$	-	Complex index of refraction
n	-	QCSC potential parameter
N_A	$items \cdot mol^{-1}$	Avogadro's number
n_g	$atoms \cdot m^{-3}$	Gas number density
N_g	$atoms \cdot s^{-1} \cdot m^{-2}$	Incident number flux of gas atoms

N_v	$atoms \cdot s^{-1} \cdot m^{-2}$	Vapor molecular umber flux
n_λ	-	Real component of complex index of refraction
p	-	SW potential parameter
$P(\mathbf{b})$	-	Evidence
$P(\mathbf{b}\|\mathbf{x})$	-	Likelihood
$P(d_p)$, $P(d_p,\mathbf{x})$	-	Probability density of nanoparticles having size d_p
$P(\mathbf{x}\|\mathbf{b})$	-	Posterior distribution
p_g	Pa	Gas pressure
$P_{pr}(\mathbf{x})$	-	Prior distribution
p_v	Pa	Vapor pressure
$p_{v,o}$	Pa	Vapor pressure of bulk material
q	-	SW potential parameter
$Q_{abs,\lambda}(d_p)$	-	Absorption efficiency at wavelength λ
q_{cond}	W	Conduction heat transfer
q_{evap}	W	Evaporation heat transfer
q_{rad}	W	Radiation heat transfer
r	nm	Interatomic distance
R	$J \cdot kg^{-1} \cdot K^{-1}$	Specific gas constant
r_c	nm	Cutoff distance
r_e	nm	Morse potential equilibrium interatomic distance
r_{gs}	nm	Interatomic distance between gas and surface atoms
r_p	nm	Particle radius
t	ns	Time
T_b	K	Boiling temperature

T_{cr}	K	Critical temeprature
T_{eff}	K	Effective temperature
T_g	K	Gas temperature
T_i	K	Initial temperature
T_o	K	Thermostat heat bath temperature
T_p	K	Particle temperature
T_r	-	Reduced temperature
T_s	K	Surface temperature
U	meV	Interatomic potential
U_{gs}	meV	Gas-surface interatomic potential
$V(r_{ij})$	meV	Pairwise potential between i^{th} and j^{th} atoms
v_g	$m \cdot s^{-1}$	Gas velocity
w_{cond}	-	Weight of conduction resulting from gas components
w_g	$m \cdot s^{-1}$	Velocity of gas molecule normal to the surface
x	-	Size parameter
x	-	Vector of parameters of interest
z	nm	Height of gas molecule above surface

Greek Symbols

Symbol	Unit	Definition
α	-	Thermal accommodation coefficient (TAC)
α_n	-	Normal thermal accommodation coefficient
α_n	-	Translational thermal accommodation coefficient
β	-	Collision efficiency

χ^2	-	Chi-squared function
β	-	FS electron density function parameter
δ	Nm	Tolman length
ε	meV	EAM potential well depth parameter
ε	meV	SW two-body well depth
ε_{gs}	meV	LJ 6-12 potential well depth
ϕ	-	Model/input parameter
$\phi(r_{ij})$	meV	EAM electron density function
ϕ_2	meV	SW two-body contribution
ϕ_1	meV	SW three-body contribution
γ	-	Specific heat ratio
γ	-	SW potential parameter
γ_s	$N \cdot m^{-1}$	Surface tension of nanoparticle surface
$\gamma_{s,o}$	$N \cdot m^{-1}$	Surface tension of bulk material
κ_λ	-	Imaginary component of the complex index of refraction
λ	nm	Wavelength
λ	nm	More potential width parameter
λ	-	Lowe-Andersen parameter relating to Maxwellian distribution
λ	-	SW potential parameter
λ_g	nm	Mean free path of gas atoms
μ	-	Reduced mass
μ_i	K, a.u.	Expected value of observed data

ν	s^{-1}	Stochastic collision frequency in Poisson distribution
$\cos(\theta_b)$	-	SW potential parameter
θ_{ijk}	rad	Angle between the i^{th} and k^{th} atom from the j^{th} atom
$\pi(x)$	-	Sample distribution
ρ	$kg \cdot m^{-3}$	Density
ρ_i	-	Local electron density
σ	nm	SW potential parameter
σ	nm	Standard deviation of particle sizes
σ_g	nm	Geometric standard deviation
σ_g	nm^2	Variable hard sphere (VHS) gas atom collision cross sectional area
σ_{gs}	nm	LJ 6-12 interatomic equilibrium distance
σ_i	K, a.u.	Standard deviation/noise in observed data
$\hat{\sigma}_{ij}$	nm	Unit separation vector
τ	ps	Berendsen thermostat parameter
ζ_{rot}	-	Rotational degrees of freedom of a gas molecule
ζ_{tot}	-	Total degrees of freedom of a gas molecule
ζ_{trans}	-	Translational degrees of freedom of a gas molecule
ζ_{vib}	-	Vibrational degrees of freedom of a gas molecule

Subscripts

Subscript	Definition
exp	Experimental
g	Gas

i	Initial
i, j, k	Indices
mod	Modelled
o	Out/final
p	Particle
s	Surface
v	Vapor

Abbreviations

Abbreviation	Definition
BCC	Body-centered cubic
BET	Brunauer-Emmett-Teller
CENIDE	Center for Nanointegration Duisburg-Essen
CMC	Carboxylmethyl cellulose
CMD	Count median diameter
DFT	Density functional theory
DLS	Dynamic light scattering
EAM	Embedded atom model
FS	Finnis-Sinclair
GGA	Generalized gradient approximation
LAMMPS	Large-scale Atomic/Molecular Massively Parallel Simulator
LDA	Local density approximation
LJ 6-12	Lennard-Jones 6-12
MCMC	Marcov chain Monte Carlo

MD	Molecular dynamics
PE	Percent error
RSC	Relative sensitivity coefficient
SW	Stillinger-Weber
TAC	Thermal accommodation ceofficient
TEM	Transmission electron microscopy
TiRe-LII	Time-resolved laser-induced incadescence
QCSC	Quantum-correct Sutton-Chen

Chapter 1

Introduction

1.1 Motivation

Non-carbonaceous nanoparticles are being considered for a variety of applications in science and technology. Metal nanoparticles have many practical and emerging applications in materials science. They can be extremely effective catalysts due to their large surface area to volume ratio, for example, and are an efficient way to synthesize large quantities of single-walled carbon nanotubes [1]. The strong phonon-plasmon resonance of metal nanoparticles in the visible spectrum can also be exploited to engineer the optical and radiative properties of surfaces, such as photovoltaic and thermophotovoltaic materials [2,3]. Iron nanoparticles in particular are being considered for targeted drug delivery, medical imaging, environmental remediation, and magnetic-based recording media [4], primarily due to their magnetic behavior.

The unique electromagnetic properties of silicon nanoparticles have also led to many interesting applications. In medicine, for example, silicon nanoparticles may be used for biomedical diagnostics, targeted drug delivery, cancer therapy, cell tracking and labelling, and tissue engineering [5]. Photovoltaic device performance has undergone a paradigm shift with the introduction of nanoscale films containing silicon quantum dots, which can greatly increase photoelectric conversion efficiency [6]. Silicon nanoparticles also enhance the performance of other electronic equipment, including lithium-ion batteries [7] solid-state devices, LEDs, and printable electronics [8].

As the electromagnetic, transport, and chemical properties of these nanoparticles (and hence their functionality in these applications) are size dependent, it is critical that diagnostics be developed to size them. This is particularly important for aerosolized nanoparticles, since gas-phase synthesis is the most economical ways to manufacture nanoparticles in large quantities. These particles are most often sized by *ex situ* analysis. For example, transmission electron microscopy (TEM) has the capability of imaging nanoparticles at various magnifications to identify particle morphology, composition, and even, in more modern microscopes, atomic structure. Scanning electron microscopes provide similar images with greater depth-of-field but

with poorer resolution. Brunauer-Emmett-Teller (BET) analysis infers the specific surface area of nanoparticles from the physisorption of N_2 by a sample of nanoparticle powder. Assuming that the nanoparticles are monodisperse spheres, these measurements can be converted to a representative nanoparticle diameter based on knowledge of the sample mass. However, these techniques are time consuming and require the collection of a sample for *ex situ* measurement.

Time-resolved laser-induced incandescence (TiRe-LII), originally developed as a diagnostic for soot, is an *in situ* technique that can be performed in real time. As such, this technique provides various advantages over typical sizing techniques. As it does not require any physical probing, this technique has been used extensively to explore the combustion dynamics of everything from small-scale combustion environments, such as internal combustion engines [9], to large-scale combustion in aero-engines [10,11]. The *in situ* nature of TiRe-LII allows practitioners to temporarily and spatially resolve the volume fraction and/or primary particle size of soot formation in combustion applications [12,13,14,15,16,17,9], generating soot distributions such as those seen in Figure 1-1 [9]. TiRe-LII may also allow for closed-loop control of gas-phase synthetic nanoparticle synthesis, an area of active research.

TiRe-LII uses a laser pulse to heat the nanoparticles within an aerosol sample to incandescent temperatures; the incandescence is then measured as the nanoparticles equilibrate with the ambient gas. Since larger nanoparticles cool more slowly than smaller nanoparticles, the nanoparticle size distribution can be inferred by regressing simulated incandescence curves (or, more often a pyrometric temperature derived from incandescence measurements at multiple wavelengths) to corresponding experimental data. The simulated LII data is generated using a model of the heat transfer between the nanoparticles and the surrounding gas. In the case of

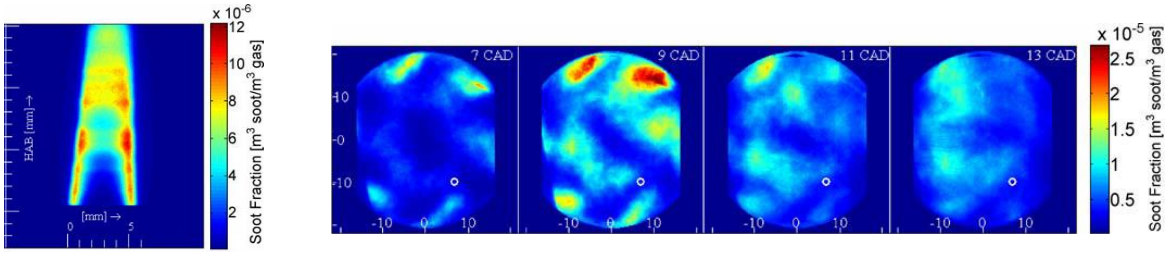

Figure 1-1: Images of two-dimensional TiRe-LII on soot (left) in flame at 10.5 mm height above burner (HAB) and (right) from inside the engine combustion chamber at various crank-angle-degree (CAD) before-top-dead-center. Images taken from Boiarciuc et al. [8].

non-carbonaceous nanoparticles, heat transfer is usually dominated by evaporation from the nanoparticle immediately after the pulse, and free-molecular heat conduction at longer cooling times. Calculating heat conduction requires knowledge of the thermal accommodation coefficient, which specifies the average energy transfer when a gas molecule scatters from a surface. As it remains one of the major challenges in extending TiRe-LII to non-carbonaceous nanoparticles, it has received specific attention in several studies and will be discussed more thoroughly in this thesis.

1.2 Literature Review

The earliest references to TiRe-LII are generally attributed to Weeks and Duley in 1974 [18] and Eckbreth in 1977 [19]. Despite the technique now being four decades old, TiRe-LII remains an area of active research. The technique remains primarily a combustion diagnostic with much of the active research investigating the physical processes involved in applying the technique to soot, such as the effects of nanoparticle aggregation [20,21,22] and incomplete thermal accommodation [23,24,25,26,27,28].

Vander Wal et al. [29] made some of the first TiRe-LII measurements on non-carbonaceous nanoparticles considering tungsten, iron, molybdenum, and titanium; while they did not infer nanoparticle sizes from the TiRe-LII data, the incandescence decay suggested that this would be possible provided that nanoparticle cooling could be modeled accurately.

The earliest attempt to recover the size of metallic nanoparticles was by Filippov et al. [30], who investigated silver nanoparticles formed by inert gas condensation in argon. Unfortunately, their size calculation relied on a conduction model that was later shown to be flawed because it neglects the temperature-dependence of gas transport properties and implicitly assumes a thermal accommodation coefficient (TAC) of unity, which later studies have shown to be unlikely [31].

Starke et al. [32] carried out LII measurements on iron nanoparticles formed by passing a shockwave through argon doped with $Fe(CO)_5$. By comparing monochromatic TiRe-LII traces to a limited number of TEM images of extracted nanoparticles, they estimated $\alpha = 0.33$ for iron nanoparticles in argon. Kock et al. [33] also performed TiRe-LII on iron nanoparticles formed in shock tubes containing pure argon and nitrogen as carrier gases. While they also conducted a

complementary TEM study, unlike Starke et al. [32], Kock et al. [33] did not incorporate these results directly into their analysis of the TiRe-LII data. Instead, they assumed that the nanoparticle sizes obeyed a lognormal distribution characterized by the geometric mean, $d_{p,g}$, and geometric standard deviation, σ_g, and then attempted to infer both α and $d_{p,g}$ from the TiRe-LII data by specifying a distribution width of σ_g = 1.5, typical of self-preserving distributions that arise when the coalescence and fragmentation processes responsible for nanoparticle growth stability [34]. Their analysis predicted TAC to be approximately 0.13 for iron nanoparticles in both argon and nitrogen (assuming that surface energy is accommodated exclusively into the translational energy mode of the nitrogen molecule), and the TEM study suggested that nanoparticles generated in argon were considerably larger than those formed in nitrogen.

Eremin et al. [35] used TiRe-LII and transmission electron microscopy to study iron nanoparticles formed by photolysis of $Fe(CO)_5$ in carbon monoxide, argon, and helium. By comparing TiRe-LII data to TEM-derived particle sizes, they found the TAC to vary widely depending on the bath gas, with values of 0.01 for helium, 0.1 for argon, and 0.2 for carbon monoxide, again assuming that surface energy is accommodated only into the translational mode of the gas molecule. Moreover, in their study Eremin et al. [35] also found that the particle sizes (hence coalescence rates) were related to the TAC, in contrast to the findings of Kock et al. [33]. Eremin et al. also expanded the scope of their study to focus on deriving parameters important to TiRe-LII analysis of iron nanoparticles, more specifically the optical constants [36] and vaporization properties [37].

Reimann et al. [38] conducted preliminary TiRe-LII measurements on nickel nanoparticles formed by inert gas condensation with argon as a carrier gas. This experimental study was complemented by a molecular dynamics study carried out by Daun et al. [39] in an attempt to quantify the TAC. To this date, nanoparticle sizes have yet to be accurately inferred from this data.

Murakami et al. applied TiRe-LII to size molybdenum nanoparticles in argon, helium, carbon dioxide, and helium. Unfortunately, the model made several false assumptions, not the least of which was assuming α = 1, which led to poor fits in most of the gases. The study did, however, provide proof that TiRe-LII is possible for molybdenum nanoparticles and collected spectrally resolved signals that could also elucidate information regarding possible spectral abnormalities in the laser-induced signals.

TiRe-LII practioners have also examined various oxides, including MgO [40], TiO_2 [41,42], Fe_2O_3 [43], and SiO_2 [44], with varying degrees of success.

1.3 Present Work

The present work summarizes attempts to extend the use of TiRe-LII from its original application on soot to molybdenum, silicon, and iron and generally refine the TiRe-LII model. Chapter 2 summarizes the concepts underlying TiRe-LII analysis, including theoretical modeling of nanoparticle incandescence (§2.1) and cooling (§2.2). This includes defining some of the material properties, such as the TAC, which will receive more intensive study in subsequent chapters.

As the TAC is one of the major obstacles in applying TiRe-LII to both soot and synthetic nanoparticles, Chapter 3 focuses on a molecular dynamics (MD) technique to calculate the TAC using classical dynamics and atomic trajectories. This chapter seeks to provide background information on the MD technique used (§3.1), provide historical information on how the technique has been used (§3.2), and present the results of applying the technique to iron, molybdenum, and silicon using two independent codes (§3.3 and §3.4).

Having developed a theoretical model to define the physical processes involved, Chapter 4 describes the various uncertainties inherent to this model and the statistical methods used to relate the theory to the experimental data. It is complimented by a discussion of several of the statistical techniques that the author used found in Appendix C.

Chapter 5 describes a reinterpretation of data from Murakami et al. [45], wherein the authors sized molybdenum nanoparticles in various buffer gases. The analysis presented in this work attempts to simultaneously infer the TAC and lognormal distribution parameters (geometric mean and geometric standard deviation) from the data. The results show that it is impossible to simultaneously infer the geometric mean and TAC. As a consequence, the results incorporate TACs calculated in Chapter 3 to infer the two remaining parameters.

Chapter 6 presents one of the first attempts to size silicon nanoparticles within a plasma reactor by TiRe-LII. The nanoparticle diameters were inferred from the experimentally-observed temperature decay, using a conduction model with separate terms for H_2 and Ar and an evaporation model using Watson's equation for the heat of vaporization. Maximum likelihood estimates of lognormal distribution parameters were found through Bayesian analysis. The

Sauter mean diameter inferred from the TiRe-LII data was compared to measurements by BET (Brunauer-Emmett-Teller) analysis on a sample nanoparticle powder.

Chapter 7 presents preliminary work using an in-house apparatus to size iron nanoparticles. The iron nanoparticles are formed in solution and then aerosolized with a pneumatic atomizer using various carrier gases, so the nanoparticle size is the same for each aerosol and the TiRe-LII signal only differs due to the different TAC for each aerosol. This facilitates a comparison of the molecular dynamics determined TAC to the experimentally determined TAC for the Fe-Ar and Fe-He aerosols.

Chapter 8 presents areas of future work broken down into three categories: molecular dynamics simulations, experimental work, and model development.

Chapter 2

Time-Resolved Laser-Induced Incandescence Theory

TiRe-LII requires knowledge of several physical phenomenon to recover any parameters from collected data. The models used to interpret this data vary widely in literature [46], especially when considering the numerous material properties used in the analysis. The Melton model [47] is generally considered to be one of the first models used to interpret particle sizes in TiRe-LII experimentation and is widely cited throughout the literature. This model incorporated a heat transfer model with three cooling modes: conduction; evaporation; and radiation. The original model did not, however, correctly account for size-dependent effects, including Rayleigh-regime optical properties, free molecular conduction, and free molecular evaporation. Subsequently, TiRe-LII practitioners have improved the models used to calculate the cooling rate and incandescence of the nanoparticles. This chapter gives an overview of the models used in TiRe-LII analysis in the present work.

2.1 Incandescence Theory

The incandescence signal measured by the spectrometer is due to the collective emission from the laser-energized nanoparticles [48] over all particle sizes

$$J_\lambda(t) = C\int_0^\infty \frac{\pi d_p^2}{4} P(d_p) Q_{abs,\lambda}(d_p) I_{b,\lambda}\left[T_p(t,d_p)\right] d(d_p) \tag{2.1}$$

where C is a calibration constant that depends on the particle volume fraction and detector optics, $P(d_p)$ is the probability density of nanoparticles having a size d_p, $Q_{abs,\lambda}(d_p)$ is their absorption efficiency, $T_p(t,d_p)$ is the temperature of these particles at time t, and $I_{b,\lambda}$ is the corresponding blackbody intensity,

$$I_{b,\lambda}(T_p) = \frac{2hc_o^2}{\lambda^5} \frac{1}{\exp\left(\frac{hc_o}{\lambda k_B T_p}\right) - 1} \tag{2.2}$$

where h is Planck's constant, c_o is the speed of light in a vacuum, and k_B is Boltzmann's constant. Coalescence and aggregation processes arising from diffusion-limited Brownian motion show that an aerosol particle distribution can often be described by a lognormal distribution [34]

$$P\left(d_p,\mathbf{x}\right)=\frac{1}{d_p\sqrt{2\pi\left(\ln\sigma_g\right)^2}}\exp\left[\frac{-\left(\ln d_p-\ln d_{p,g}\right)^2}{2\left(\ln\sigma_g\right)^2}\right] \tag{2.3}$$

where $\mathbf{x} = [d_{p,g}, \sigma_g]^T$. The radiative properties of the nanoparticles are dependent on the regime in which the nanoparticles reside, determined by the size parameter, x, [49,50]

$$x=\frac{\pi d_p}{\lambda} \tag{2.4}$$

In the Rayleigh limit, where $\lambda \gg d_p$ (as is the case in this work), the absorption efficiency is defined as

$$Q_{abs,\lambda}\left(d_p\right)\equiv -4xE\left(\mathbf{m}_\lambda\right)=4\frac{\pi d_p}{\lambda}\mathrm{Im}\left(\frac{\mathbf{m}_\lambda^2-1}{\mathbf{m}_\lambda^2+2}\right) \tag{2.5}$$

where $\mathbf{m}_\lambda = n_\lambda + i\cdot\kappa_\lambda$ is the complex index of refraction. The optical constants are a function of both temperature and wavelength and can usually be found from experimental data in literature. There are various experimental conditions under which the optical constants have been determined in literature. Several TiRe-LII practioners have used room temperature values [32,38], frequently from Palik [51], primarily due to the lack of available sources of high temperature optical properties. It is important to note, however, that several sources do report different optical constants at higher temperatures for the various synthetic materials being examined in TiRe-LII, including silicon [52,53,54,55], iron [56,57], and nickel [56,57]. This is of great important when considering that, unlike soot, these materials frequently exist in the molten state at temperatures typical of TiRe-LII experiments. Most of these studies used ellipsometry to determine these optical properties.

2.1.1 Pyrometric Temperature

While it is possible to do particle sizing by regressing modeled spectral incandescence data directly to experimentally-measured values, it is often more convenient to work with an

intermediate, pyrometrically-defined effective temperature, $T_{eff}(t)$. For a full spectrum, the effective temperature can be defined at the i^{th} timestep by fitting

$$J_\lambda(t_i) = C_2(t_i)\frac{E(\mathbf{m}_\lambda)}{\lambda} I_{b,\lambda}\left[T_{eff}(t_i)\right] \tag{2.6}$$

to the corresponding experimental spectral incandescence data where $C_2(t_i)$ is a fitting parameter that absorbs all the remaining variables, including the integral and particle size dependent properties. In a hypothetical aerosol containing identically-sized nanoparticles, $T_{eff}(t_i)$ would match the true particle temperature and C_2 would be identical at each measurement time. In most aerosols, however, d_p obeys an unknown probability density $P(d_p)$ and $T_{eff}(t_i)$ will represent an average temperature of the nanoparticles, weighted more heavily towards the larger nanoparticles due to their larger surface area and absorption efficiency. In the case of only two wavelengths, $T_{eff}(t_i)$ can be explicitly calculated by taking the ratio of $J_\lambda(t_i)$ allowing one to define

$$T_{eff}(t_i) = \frac{hc_o}{k_B}\left(\frac{1}{\lambda_2} - \frac{1}{\lambda_1}\right)\frac{1}{\ln\left\{K_{opt}\left(\frac{J_{\lambda_1}(t_i)}{J_{\lambda_2}(t_i)}\right)\left(\frac{E_{m_{\lambda_2}}}{E_{m_{\lambda_1}}}\right)\left(\frac{\lambda_1}{\lambda_2}\right)^6\right\}} \tag{2.7}$$

where K_{opt} primarily accounts for the transmissivity of the windows or other optical inefficiencies if present. It is useful to note that since K_{opt} and $E_{m\lambda 2}/E_{m\lambda 1}$ are inside a logarithm, changes in their values will only cause a shift in the entire effective temperature curve.

2.2 Heat Transfer Modelling

The heat transfer model is central to the analysis of the incandescence data as it relates the rate of temperature decay to the nanoparticle size and other unknown parameters. This section describes the generic heat transfer model used in this work. Detailed discussion regarding how the model is applied to the different materials is deferred to §5.2, §6.2, and §7.2.

The temperature decay of the nanoparticles can be defined based on an energy balance. Assuming the nanoparticles are spherical and isothermal, as the cooling time scale is much larger than the phonon relaxation time which is generally on the order of femtoseconds [58], the energy balance is defined as [33]

$$\frac{d}{dt}\left(\rho c_p T_p \frac{\pi d_p^3}{6}\right) = -q_{cond}\left(t, d_p\right) - q_{evap}\left(t, d_p\right) - q_{rad}\left(t, d_p\right) \tag{2.8}$$

where ρ is the density, c_p is the specific heat capacity, T_p is the particle temperature, d_p is the particle size, q_{cond} is heat transfer due to conduction, q_{evap} is heat transfer due to evaporation, and q_{rad} is heat transfer due to radiation. For the purposes of this work, ρ, c_p, and d_p are assumed to change weakly with temperature (and consequently time), allowing for simplification to

$$\frac{dT_p}{dt} = \frac{6}{\rho c_p \pi d_p^3}\left[-q_{cond}\left(t, d_p\right) - q_{evap}\left(t, d_p\right) - q_{rad}\left(t, d_p\right)\right] \tag{2.9}$$

Discussion of the values of ρ and c_p are deferred to subsequent sections specific to the nanoparticle material.

2.2.1 Conduction

In order to accurately model the conduction from the nanoparticles, it is first important to identify the regime in which the heat transfer is occurring. The different regimes are defined using the dimensionless Knudsen number, *Kn*, calculated by

$$Kn = \frac{\lambda_g}{L} \tag{2.10}$$

where λ_g is the mean free path of the gas atoms and L is the length scale, in this case corresponding to the nanoparticle radius, r_p [59]. Treated as an ideal gas, the mean free path of the gas atoms can be estimated multiple ways. One such way is [60]

$$\lambda_g = \frac{k_B T_g}{\sqrt{2}\sigma_g p_g} \tag{2.11}$$

where k_B is the Boltzmann constant, σ_g is the variable hard sphere (VHS) gas atom collision cross sectional area taken from Bird [61] and derived from viscosity data, p_g is the gas pressure, and T_g is the gas temperature. In this case, the cross sectional area is defined based on the gas atom of interest, including helium, argon, and others. The Knudsen number for several gases for particles with d_p = 30 nm and p_g = 10,000 Pa have been tabulated in Table 2-1.

Table 2-1: The Knudsen number of various gases as a function of temperature for d_p = 30 nm and p_g = 10,000 Pa.

Gas	Atomic Diameter [pm]	Kn	
		T_g = 273 K	T_g = 1000 K
He	233	26.0	95.3
Ar/N_2	417	8.13	29.8
CO_2	562	4.48	16.4

Having determined the Knudsen numbers, three unique regimes can be identified. When the mean free path length is much smaller than the particle size, that is, $Kn \ll 1$, conduction occurs in the continuum regime, wherein the gas can be treated as a continuous fluid rather than individual particles. Moreover, heat transfer away from the surface is a diffusion limited process as the mean free path and number density effects cancel each other out. Consequently, the magnitude of the heat transfer or, equivalently, the Nusselt number is not a function of gas pressure. Further discussion of this regime is deferred to external works such as Incopera and DeWitt [62] as it is not within the scope of the present work.

When the mean free path length is much greater than the particles size, that is, $Kn \gg 1$, conduction occurs in the free molecular regime where heat transfer away from the surface is limited by collisions between gas molecules and the surface. In this regime, the more gas molecules that are present the more collisions with the surface and, consequently, the more heat transfer away from the surface. As such, the Nusselt number is directly proportional to the gas pressure, as shown in Figure 2-1.

In the case where Kn ≈ 1, conduction occurs in the transition regime where the heat transfer is limited by both diffusion of the gas molecules away from the surface as well as the number of gas molecules present near the surface. This is often treated using Fuchs method, in which the particle is considered to be surrounded by a Knudsen layer of thickness, Δ, which is set equal to the mean free path length, λ_g [63]. As a consequence, gas molecules in the Knudsen layer are not expected to collide with any other molecules effectively transferring heat by free molecular conduction. Further, as the addition of the Knudsen layer creates an effective particle with a size greater than the path length, conduction outside of the layer will be dominated by continuum regime conduction. As the First Law of Thermodynamics requires that the gas temperature and

heat transfer be the same on either side of the boundary of the Knudsen layer, one can solve for a temperature, T_Δ, that satisfies $q_{FMR} = q_{cont}$ at the boundary. The heat transfer from the particle is then set equal to this solved value. In the case that $\Delta \to 0$, that is $Kn \ll 1$, the layer will be virtually non-existent and $T_\Delta \to T_p$, equivalent to continuum regime conduction. Conversely, if $\Delta \to \infty$, that is $Kn \gg 1$, the gas molecules will never collide with any other gas molecules and $T_\Delta \to T_g$, equivalent to the free molecular regime. As such, this transition regime conduction will smoothly transition between free molecular and continuum regime conduction, as is shown in Figure 2-1.

Given that the $Kn \gg 1$, which is appropriate for most TiRe-LII experiments as seen in Table 2-1, the conduction from the nanoparticle is in the free molecular regime

$$\dot{q}_{cond} = \pi d_p^2 N_g \left\langle E_o - E_i \right\rangle \qquad 2.12$$

where $N_g = n_g c_{g,t}/4$ is the incident number flux of gas atoms, $n_g = p_g/k_B T_g$ is the gas number density, $c_{g,t} = [8k_B T_g/(\pi m_g)]^{1/2}$ is the gas thermal velocity, and $\langle E_o - E_i \rangle$ is the average change in energy of scattered gas atoms.

This energy transfer term is generally defined using the thermal accommodation coefficient

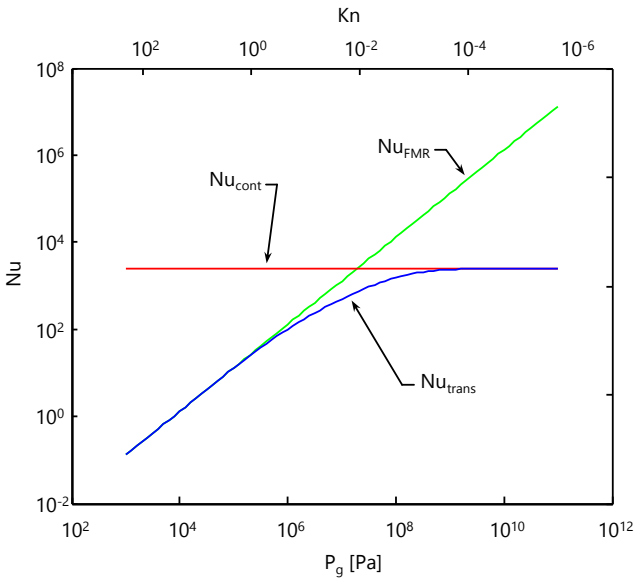

Figure 2-1: Heat conduction from a particle can take place in the free molecular, transition, or continuum regimes, depending on the Knudsen number, Kn. Case shown is for iron with d_p = 30 nm, T_p = 3000 K, T_g = 300 K, α = 0.3.

$$\alpha = \frac{\langle E_o - E_i \rangle}{\langle E_o - E_i \rangle_{max}} \tag{2.13}$$

where $\langle E_o - E_i \rangle_{max}$ is the maximum energy transfer allowed by the Second Law of Thermodynamics, defined based on the energy available between the gas and particle temperature. The average energy that can be accommodated by a gas molecule, $\bar{E}$, is given by

$$\bar{E} = \frac{1}{2} k_B T_g \zeta_{tot} = \frac{1}{2} k_B T_g \left(\zeta_{trans} + \zeta_{rot} + \zeta_{vib} \right) \tag{2.14}$$

where ζ_{trans}, ζ_{rot}, and ζ_{vib} are the available degrees of freedom in the translational, rotational, and vibrational modes respectively. Effectively, this expression states that each degree of freedom available to a gas molecule corresponds to its ability to store $\frac{1}{2} k_B T_g$ of energy. Unfortunately, defining the number of degrees of freedom available to a gas molecule is not always trivial.

The translational mode refers to the energy contained in the movement of the center of mass of a gas molecule. In an unconstrained gas, gas molecules are free to move in any of the three dimensions of space, such that $\zeta_{trans} = 3$. When a surface is introduced, however, the energy of the gas molecules is shifted such that twice the normal amount of energy is transferred in the direction perpendicular to the surface. This is due to the fact that molecules with higher speeds in the translational direction are more likely to cross the boundary. Although not actually an increase in the number of degrees of freedom, this can be accommodated by setting

$$\zeta_{trans} = 2 + \zeta_{trans,t} \tag{2.15}$$

where $\zeta_{trans,t} = 2$ is the tangential translational degrees of freedom. As all gas molecules, regardless of the number of atoms and orientation are allowed to have this bulk motion, this applies to any gas molecules.

The rotational degrees of freedom come as a result of relative motion of gas atoms where the distance between the gas atoms does not change, that is, the gas molecule rotates about its center of mass along the axis in any of the three dimensions allowing for a maximum of $\zeta_{rot} = 3$. As this requires multiple atoms, monatomic gas molecules, such as Ar and He, cannot accommodate energy into these modes, such that $\zeta_{rot} = 0$. Further, the moment of inertia along the axis parallel to the bonds in linear polyatomic molecules, such as N_2, CO_2, and CO, is negligible, reducing one of the degrees of freedom such that $\zeta_{rot} = 2$.

The vibrational degrees of freedom are more difficult to determine as their accessibility during collisions is highly dependent on temperature due to quantum effects. In attempts to accommodate this, many LII practitioners have determined the total degrees of freedom using the temperature dependent ratio of the heat capacities, γ, such that

$$\zeta_{tot} = \frac{\gamma\left(T_g\right)+1}{\gamma\left(T_g\right)-1} \qquad 2.16$$

This allows for any number of the possible degrees of freedom to be inaccessible to heat transfer and be quantified using a well-known quantity. There has been some dissention in the LII literature over what value of γ should be used in Eqn. 2.16. Many researchers (e.g. [33], [33], [35]) assume that surface energy only enters the translational mode of the gas molecule corresponding to $\gamma = 5/3 \approx 1.7$ or $\zeta_{tot} = 4$. Filippov and Rosner [64] recommend a value of γ defined by

$$\frac{1}{\gamma-1} = \frac{1}{T_p - T_g}\int_{T_g}^{T_p} \frac{dT}{\gamma^*\left(T\right)-1} \qquad 2.17$$

which accounts for the temperature dependence of γ, mainly due to the large spacing of vibrational quanta relative to the energy transfer. The origin of this equation is described in greater detail by Liu et al. [31]. The results of recent molecular dynamics (MD) simulations of the gas-surface scattering that underlies particle cooling in LII [65] cast doubt on this treatment, however. The simulations showed that: (i) the very brief interaction between the gas molecule and soot surface precludes energy transfer into the vibrational mode of the gas molecule, and;

Table 2-2: The number of degrees of freedom available to gas molecules of different types during collisions with a nanoparticle surface under the conditions typical of TiRe-LII.

Gas Molecule Type	Examples	$\zeta_{trans,t}$	ζ_{rot}	ζ_{vib}
Montatomic	Ar, He, Ne, Xe	2	0	0
Linear Polatomic	N_2, CO_2, CO, N_2O	2	2	0
Nonlinear Polyatomic	CH_4, C_2H_6	2	3	0

(ii) while the vibrational mode of the gas molecules is "frozen", the rotational mode is active. Based on these findings, a more realistic treatment is to set [65]

$$\bar{E} = \left(2 + \frac{\zeta_{rot}}{2}\right) k_B T_g \tag{2.18}$$

where, ζ_{rot} = 0 for monatomic gas molecules, ζ_{rot} = 2 for the linear polyatomic gas molecules, and ζ_{rot} = 3 for non-linear polyatomic gas molecules following above. In Eq. 2.16, this corresponds to setting γ = 5/3 ≈ 1.7 for monatomic gas molecules, γ = 7/5 = 1.4 for the linear polyatomic molecules, and γ = 4/3 ≈ 1.3 for non-linear polyatomic gas molecules, as summarized in Table 2-2.

Consequently heat conduction from the nanoparticles is given by

$$q_{cond}\left(t, d_p\right) = \alpha \pi d_p^2 \left(\frac{p_g c_{g,t}}{4T_g}\right)\left(2 + \frac{\zeta_{rot}}{2}\right)\left(T_p - T_g\right) \tag{2.19}$$

The thermal accommodation coefficient can also be found using molecular dynamics (MD), as described in Chapter 3 of this work.

2.2.2 Evaporation

The Knudsen number is also relevant in deciding how to treat evaporation from the nanoparticles. However, in this case λ is defined slightly differently [59]

$$\lambda_v = 2D\sqrt{\frac{M_v}{2k_B N_A T_p}} \tag{2.20}$$

where $D = (1/3)\lambda_g c_{v,t}$ is the diffusion coefficient of the vapor described in terms of the mean free path considering the species in bulk as defined by Eq. 2.11 [66] and $c_{v,t} = [8k_B T_p/(\pi m_v)]^{1/2}$ is the thermal speed of the vaporized species [60]. Evaluating the Knudsen number for iron, molybdenum, and silicon, the particles used in this work, we find the values stated in Table 2-3 at p_g = 10,000 Pa and d_p = 30 nm. Similar regimes exist as to those observed in conduction. In this case, however, the particles are well within the free molecular regime where $Kn \gg 1$.

Assuming equilibrium and spherical nanoparticles, evaporation in the free molecular regime is given by the product of the evaporating molecular number flux, N_v, the nanoparticle surface area, the heat of vaporization, Δh_v, and collision efficacy, β,

Table 2-3: The Knudsen number of various materials as a function of temperature for d_p = 30 nm and p_g = 10,000 Pa.

Gas	Atomic Diameter [pm]	Kn		
		T_p = 500 K	T_p = 1500 K	T_p = 2500 K
Si	220	242	725	1210
Fe	280	1490	4470	7450
Mo	290	1390	4170	6950

$$\dot{q}_{evap} = N_v \pi d_p^2 \Delta h_v \beta \tag{2.21}$$

The evaporating molecular number flux can be given by $N_v = n_v c_{v,t}/4$ where $n_v = p_v/(k_B T_p)$ is the molecular number density of vaporized species. This gives

$$\dot{q}_{evap} = \left(\frac{p_v c_{v,t}}{4 k_B T_p} \right) \pi d_p^2 \Delta h_v \beta \tag{2.22}$$

where $c_{v,t} = [8 k_B T_p/(\pi m_v)]^{1/2}$. The vapor pressure, p_v, is generally given by the Clausius-Clapeyron equation [36]

$$\ln\left(p_v\right) = -\frac{\Delta h_v}{R}\frac{1}{T_p} + C \tag{2.23}$$

where R is the specific gas constant and C is a material constant. This relates the vapor pressure to the enthalpy of vaporization provided that the process is approximately in phase equilibrium. This means that one must only quantify one of either the enthalpy of vaporization or the vapor pressure to have knowledge of both. There have not been thorough studies quantifying the validity of this equilibrium assumption, but it has been applied extensively in TiRe-LII literature [46]. It is normally easier to work with the heat of vaporization with many TiRe-LII practitioners picking either a constant value or expressions as a function of temperature [46]. A common way of calculating the heat of vaporization is Watson's equation [67,68]

$$\Delta h_v = K\left(1 - T_r\right)^{0.38} \tag{2.24}$$

where K is a material constant, generally determined by the heat of vaporization at atmospheric pressure, and $T_r = T_p/T_{cr}$ is the reduced temperature. Although this equation has seen extensive use in literature [67] it has yet to be implemented in TiRe-LII.

More recently, TiRe-LII practitioners have included corrections in the vapor pressure for surface curvature. In 2006, Kuhlmann et al. [28] introduced the Kelvin equation to TiRe-LII analysis on soot particles. The Kelvin equation corrects the bulk vapor pressure, $p_{v,o}$, given in this case by Eq. 2.23, for curvature using the surface tension, γ_s, such that

$$p_v = p_{v,o} \exp\left[\frac{4\gamma_s}{d_p \rho R T_p}\right] \tag{2.25}$$

They found that even if they considered substantial changes in the surface tension suggested by Nanda et al. [69], the effects on the cooling were negligible. More recently, in 2013, Eremin et al. [37] applied the same correction to TiRe-LII analysis of iron nanoparticles. They found that the effect was more significant with effects being noticeable for nanoparticles below 10 nm. Moreover, they too discussed the possibility of changes in the surface tension due to deviations in the surface tension from its bulk value, citing a more recent paper by Nanda et al. [70] from 2003. The difference between soot and iron can be attributed to the larger value of the vaporization term for iron nanoparticles. As such, it can be concluded that the Kelvin effect should at least be considered for nanoparticles of different materials, as its effect may be significant. Moreover, possible changes in the surface tension at smaller nanoparticle sizes may enhance this effect. Though other works, such as Lu and Jiang [71], cast doubt on Nanda et al., suggesting that changes to the surface can be accounted for using the Tolman equation

$$\gamma_s = \frac{\gamma_{s,o}}{1 + 4\delta / d_p} \tag{2.26}$$

where δ is the Tolman length taken as the atomic dimater for $\delta/d_p \geq 20$ and $\gamma_{s,o}$ is the bulk surface tension, generally taken from literature. Discussion of how these effects were implemented specific to each material is deferred to subsequent chapters.

2.2.3 Radiation

Radiation heat transfer from the nanoparticles in the Rayleigh regime is obtained by solving

$$q_{rad}\left(t, d_p\right) = \int_0^\infty \frac{\pi d_p^2}{4} Q_{abs,\lambda}\left(d_p\right) \pi I_{b,\lambda}\left[T_p\left(t, d_p\right), \lambda\right] d\lambda \tag{2.27}$$

where $Q_{abs,\lambda}$ is the aforementioned absorption efficiency, present to modify blackbody radiation based on the particle size and wavelength. This term corresponds to the previously discussed incandescence evaluated at a single nanoparticle size and integrated to accommodate for emission across all wavelengths.

2.2.4 Mode Comparison

Figure 2-2 shows the significance of the various heat transfer modes as a function of temperature for various particles in argon. The figures are evaluated at a gas temperature and pressure of 298 K and 101 kPa respectively. Changes to these conditions could also have an effect on the significance of the conduction from the particle to the gas, but the main trends are still observed. In all cases, except for large molybdenum particles (~100 nm) at high temperatures, radiation is

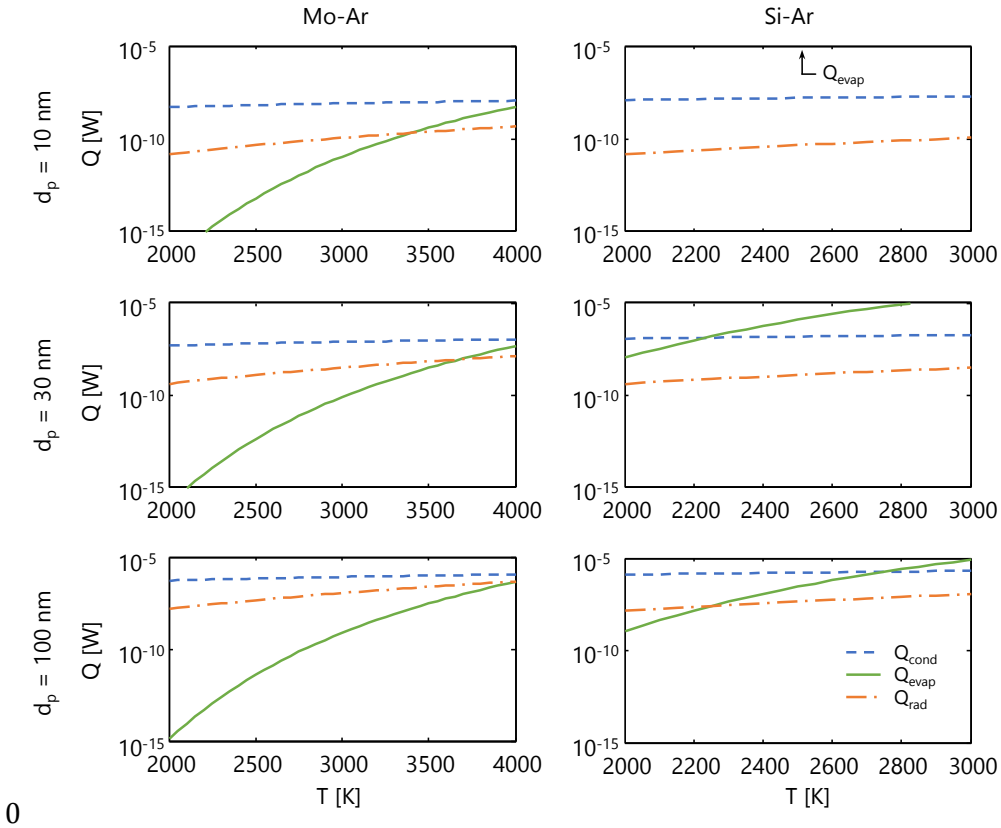

0

Figure 2-2: Value of heat transfer modes plotted as a function of particle temperature for a series of surface-gas pairs and particle sizes. Vertical dashed lines correspond to temperatures at which two modes overlap. The gas temperature and pressure were 298 K and 101 KPa respectively.

at least two orders of magnitude less than any other heat transfer mode. As this condition does not occur in this study, radiative heat transfer will be ignored throughout this work. It is also useful to note that evaporation is not significant for molybdenum in the range of temperatures and particle sizes considered Figure 2-2. The ramifications of this will be discussed further in Chapter 5. Increases in particles size result in a shift in the dominant heat transfer mode, with evaporation not being relevant until higher temperatures for larger particles. Fe-Ar shows the same features as Si-Ar, with evaporation being dominant at small particles a high temperatures. As such, evaporation is expected to play a significant role in Si and Fe signals.

Chapter 3

Thermal Accommodation Coefficient

An important step in applying the model described in Chapter 2 is to accurately define the properties used in the model. The thermal accommodation coefficient (TAC) is one such property that represents one of the major obstacles in accurately modeling TiRe-LII data, particularly when extending time-resolved laser-induced incandescence to other materials. Saxena and Joshi [72] consolidated the thermal accommodation coefficient from multiple studies. In these studies, however, the surface temperatures (typically 10-1000 K) are much lower than those typical of TiRe-LII experiments. Moreover, these experimental results are often subject to considerable experimental uncertainty due to the presence of desorbed species that contaminate the surface. Molecular beam studies [73] are an alternative, but in this scenario the energies of the incident gas molecules are much larger (sometimes orders of magnitude) compared to the ambient gases typical of LII experiments.

In 2008, Daun et al. [74] performed an experimental TiRe-LII study on soot in various gases in an attempt to observe possible trends in the TAC. Plotting the TAC against the reduced mass, $\mu = m_g/m_s$, Daun et al. were able to make the following major observations: (i) the TAC of the monatomic gases increases monotonically with increasing μ, and (ii) the TAC decreases as the complexity of the gas molecule increases, to the fact that energy is accommodated less efficiently into the internal energy modes of the gas molecule.

In order to expedite the process of determining the TAC for various materials, Daun et al. [75] used molecular dynamics (MD) to predict the TAC for multiple gas-surface pairs. Molecular dynamics uses classical mechanics and the potential energy of atoms to describe atomic trajectories. By allowing gas molecules to scatter from a heated surface of atoms, which represent the laser-energized nanoparticle, molecular dynamics is able to predict the average energy that is transferred to gas atoms during the collision. A similar technique was used by Hu and MacGaughey [76] to quantify the thermal accommodation coefficient between carbon and a number of gases for various carbon nanotube applications including gas sensors [77,78], enhanced heat transferring surfaces [79], hydrogen storage [80,81], and field emitters [82].

This chapter describes this technique and how it was applied to various gas-surface pairs, including some values that will be used in subsequent chapters.

3.1 Simulation Details

3.1.1 Interatomic Potentials

In molecular dynamics simulations, the atoms interact using potentials defined between the atoms that constitute the nanoparticle surface and a pairwise potentials between the surface atom and the atoms that constitute the gas molecule.

The interatomic potentials defined between the atoms in the surface depends on the material being considered. Rigorously-derived potentials have been developed for the materials considered in the TiRe-LII experiments. Further discussion is deferred to §3.3 and §3.4 for specific materials.

The surface-gas pairwise potential is more problematic since, in contrast to homogeneous systems, rigorously-derived interatomic potentials between gas molecules and surface atoms are not generally available in the literature. Instead, many studies employ the Lorentz-Berthelot combining rules [83] to define the surface-gas potential. In this approach, the interaction between dissimilar atoms is represented with a pairwise Lennard-Jones 6-12 potential

$$U_{gs}\left(r_{gs}\right) = 4\varepsilon_{gs}\left[\left(\frac{\sigma_{gs}}{r_{gs}}\right)^{12} - \left(\frac{\sigma_{gs}}{r_{gs}}\right)^{6}\right] \qquad 3.1$$

where the parameters for the heterogeneous system are the arithmetic and harmonic averages of those from the corresponding homogeneous systems, $\sigma_{gs} = (\sigma_{ss}+\sigma_{gg})/2$ and $\varepsilon_{gs} = (\varepsilon_{ss}\times\varepsilon_{gg})/2$ and r_{gs} is the distance between the gas and surface atoms. Many studies, among them [84,85,86], have used this technique to model gas molecules scattering from metal surfaces. When Daun et al. used this potential to model α for laser-energized nickel nanoparticles in argon, however, they obtained $\alpha \approx 1$ [39], due to the exceptionally large potential well shown in Figure 3-1. Other studies have also shown that the Lorentz-Berthelot combining rules produce non-physical results in MD simulations [87,88,89,90]. For example, Chase et al. [90] were only able to reproduce experimentally-observed results from low incident energy scattering of argon from liquid indium using a potential that was approximately an order of magnitude less than that predicted by the

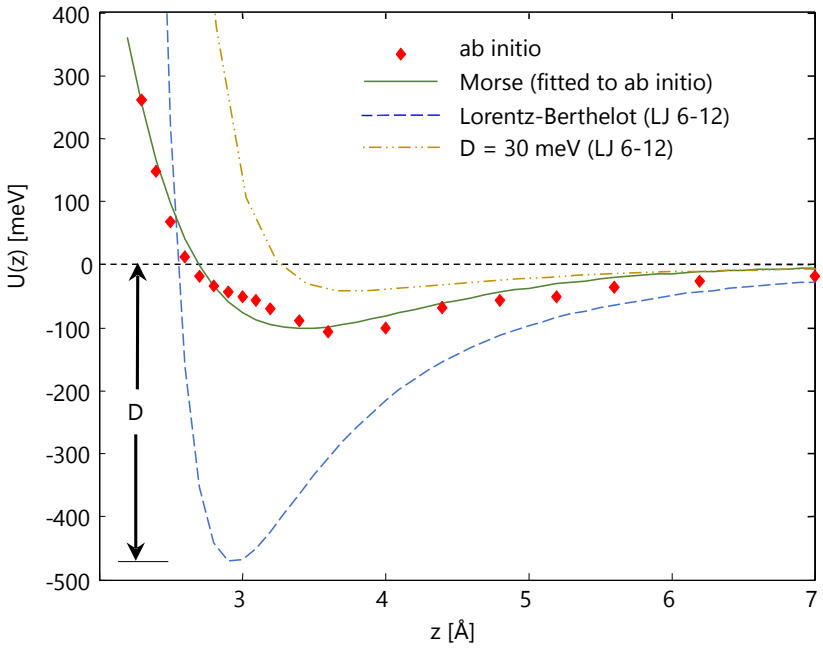

Figure 3-1: The surface-gas potential defined for Ni-Ar showing the potential resulting from the Lorentz-Berthelot combining rules, a Lennard-Jones 6-12 potential with a well depth of 30 meV, the raw data from the DFT calculation, and the Morse potential fit to the DFT calculations.

Lorentz-Berthelot rules. The inadequacy of the Lorentz-Berthelot combining rules should not be surprising, since the interatomic potentials between metal atoms, dominated by electron sharing, are completely unlike metal-gas potentials, in which charge transfer is likely.

In this work we instead fit a pairwise Morse potential, having the general form

$$U_{gs}\left(r_{gs}\right) = D\left[e^{-2\lambda\left(r_{gs}-r_e\right)} - 2e^{-\lambda\left(r_{gs}-r_e\right)}\right] \qquad 3.2$$

where D, λ, and r_e are specific to the gas/surface molecular pair. The parameters are found by fitting superimposed pairwise potentials to *ab initio* derived ground state energies of a gas molecule at various heights above 2 × 2 × 2 supercell with periodic boundary conditions along the lateral surfaces. The ground state energies are calculated using WIEN2k [91] density functional theory program with a generalized gradient approximation (DFT-GGA) and the parameterization of Perdew et al. [92] for the exchange and correlation potentials. In this approach, the unit cell is divided into muffin-tin spheres that are centered on atoms and the interstitial region. The calculation then uses a linear combination of atomic orbitals for the muffin-tin spheres and plane waves in the interstitial region. Figure 3-1 shows the ground state

Table 3-1: The DFT-drived Morse potential parameters used to define the gas/surface interactions in the classical molecular dynamics simulations.

	Fe/Ar	Fe/He	Mo/Ar	Mo/He	Si/Ar	Si/He
D [meV]	2.238	2.483	3.027	0.548	4.669	1.130
r_e [Å]	0.4779	0.4281	0.4629	0.5264	0.4647	0.4534
λ [Å]	0.1204	0.1290	0.1065	0.0945	0.1256	0.1398

energy for various argon molecule heights above a Ni surface, along with the best fit obtained by summing Morse potentials over the gas/surface pairs [39]. The resultant Morse potential parameters used in the classical molecular dynamics simulations are given in Table 3-1. As the WIEM2k calculations were performed by a collaborating researcher (J. Titantah), further discussion of the DFT calculations are deemed out of the scope of the present work.

No interatomic potential is defined between the atoms within gas molecules. When considering polyatomic gas molecules, the atoms are considered to be rigid. Although this is not actually true, it has been shown that the internal vibrational modes of the gas molecules are unable to accommodate any of the energy transfer and are thus irrelevant in the collision dynamics [65], primarily due to the small spacing of the vibrational quantum levels.

3.1.2 Predicting Atomic Trajectories

Having defined the interatomic potentials, the pairwise potentials are differentiated with respect to atomic displacement to obtain forces. Newton's equations of motions are then integrated by any variation of techniques depending on the specific goal of the simulation. In general, simulations can be defined based on the ensemble that they predict. The most common is the microcanoncial ensemble (NVE) which attempts to keep the energy of the system constant whilst allowing for fluctuations representative of a physical system. The velocity-Verlet algorithm [93,94], summarized in Appendix A, produces atomic trajectories consistent with this ensemble and is used throughout this work. An alternative is the canonical ensemble (NVT) which attempts to keep the temperature of the system constant instead of its energy. This is generally accomplished by introducing one of any number of thermostats with the effectiveness of any number of thermostats being an area of active research. The present work uses both ensembles to predict the TAC.

Initially the simulation employs a thermostat to set the temperature of the surface to one representative of TiRe-LII. Daun et al. [75] considered using the Berendsen thermostat, which weakly couples the system to an external heat bath at a constant specified temperature, T_o [95]. The velocities are scaled such that the fluctuations in the temperature are suppressed by

$$\frac{dT(t)}{dt} = \frac{1}{\tau}\left[T_o - T(t)\right] \tag{3.3}$$

limiting the total change in temperature per timestep. The value chosen for τ is incredibly important as very large values remove the effect of the thermostat and values near the timestep size reduce the thermostat to simple velocity scaling. It is generally recommended that τ = 0.1 ps [96]. Unfortunately, this thermostat is susceptible to the flying ice cube effect where the center of mass of the simulations changes over time, causing non-physical bulk motion of the system. This thermostat also doesn't create an accurate canonical ensemble, essentially meaning that the temperature of the system will never reach complete thermal equilibrium with the applied heat bath. Rather, the system will simply reach a constant total energy in which the kinetic energy resembles that of the specified temperature.

In implementing the code, Daun et al. [75] previously resolved this using the Lowe-Anderson thermostat. The Anderson thermostat couples a system to an external heat bath by stochastic collisions that occasionally act on random particles in the system. The number or frequency of these collisions is sampled from a Poisson distribution

$$P(t) = \nu \exp(-\nu t) \tag{3.4}$$

with parameter ν being the stochastic collision frequency. Collisions themselves involve sampling a new atomic velocity from the Maxwell distribution at a specified temperature. Lowe [97] updated this thermostat by changing the velocity sampling method to sampling from the Maxwellian of the relative velocities between a pair of particles such that new velocity of the i^{th} particle is given by

$$v_i(t) = v_i + \left(\frac{\mu_{ij}}{m_i}\right)\left[\lambda - \left(v_i - v_j\right)\cdot\hat{\sigma}_{ij}\right]\hat{\sigma}_{ij} \tag{3.5}$$

where $\hat{\sigma}_{ij}$ is the unit separation vector between the i^{th} and j^{th} particles, μ_{ij} is the reduced mass of the particle pair, and λ relates the Maxwell distribution. This presents several advantages, including that it is less disruptive at shorter time scales and conserves momentum for longer time scales [97]. Some simulations contained in this work use this thermostat.

An alternative is to use the Nosé-Hoover thermostat. The Nosé-Hoover thermostat modifies the velocity algorithm by adding an additional degree of freedom accounting for the heat bath. This is equivalent to adding a single virtual particle to the simulation at the specified temperature. As the Nosé-Hoover thermostat is not susceptible to the flying ice cube effect and is the preferred thermostat in LAMMPS, it is used throughout this work when performing simulations in LAMMPS.

In this work, thermostats are applied to an initial simulation such that the surface only needed to be warmed once. At the end of the warming period the atomic positions and trajectories are stored in a restart file, which are then loaded when solving for a gas-surface scattering trajectory. The degree to which a thermostat predicts a correct surface is gauged by comparing the density of the simulation, ρ, to that reported in literature for the same material and temperature, ρ_{exp}, and the temperature of the simulation, T, to the goal temperature, T_s. A sample of these outputs for the duration of the warming period is shown in Figure 3-2.

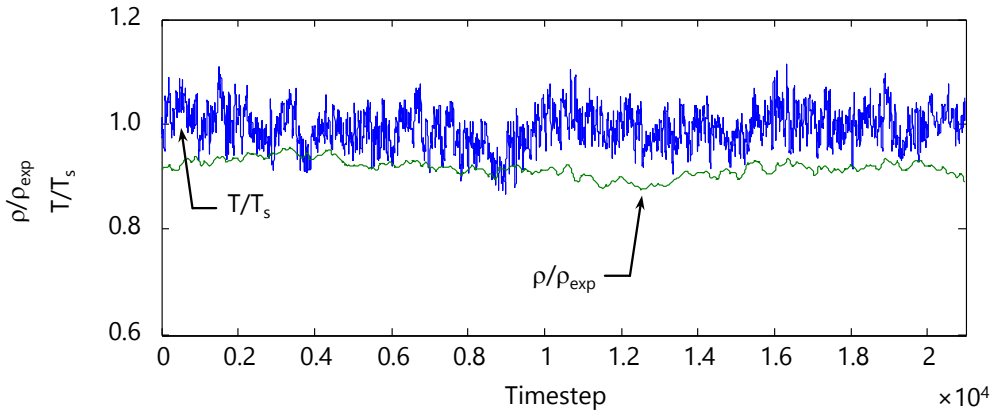

Figure 3-2: Normalized temperature and density during the warming of a molybdenum surface.

3.1.3 Estimating the Accommodation Coefficient

Having reset the surface atoms, gas molecules of various types are added to the simulation at a height of approximately 1 nm above the surface, beyond the range of the potential well of the surface. Gas molecule velocities are sampled as outlined in Appendix B, forming the kernel of a Monte Carlo integration to estimate α. The trajectories of the gas molecule and surface atoms are then tracked through the scattering process until the gas molecule reemerges from the surface with a constant escape velocity. Figure 3-3 shows a sample trajectory of an argon atom scattering from a nickel surface. The atom accelerates as it enters the potential well, and then "hops" along the potential surface until it receives enough translational energy from the vibrating surface atoms to overcome the potential well and scatter from the surface. The accommodation coefficient can then be evaluated based on Eq. 2.13

$$\alpha = \frac{\langle E_o - E_i \rangle}{\langle E_o - E_i \rangle_{max}} \tag{3.6}$$

where E_i and E_o are the initial and final energies of the gas molecule and <...> denotes the average. Appendix B shows that this can be expressed more specifically as

$$\alpha = \frac{\frac{1}{2}\left\langle \sum_j m_j \left(\mathbf{v}_{j,o} \cdot \mathbf{v}_{j,o} - \mathbf{v}_{j,i} \cdot \mathbf{v}_{j,i} \right) \right\rangle}{(2 + \zeta_{rot}/2) k_B \left(T_p - T_g \right)} \tag{3.7}$$

where $\mathbf{v}_{j,o}$ and $\mathbf{v}_{j,i}$ are the final and initial velocities vectors of the j^{th} atom of the gas molecule, respectively. For polyatomic molecules this can be decomposed into the different energy modes described in §2.2.1. The energy in each of the modes can also be categorized into the normal and tangential components of the velocity. A complete summary of the different modes and expressions for α for each is given in Appendix B.

Inherent in the present model are the assumption that there are no interstitial or surface defects and no curvature in the surface as it is expected that the particle size is much greater than the size of the simulation.

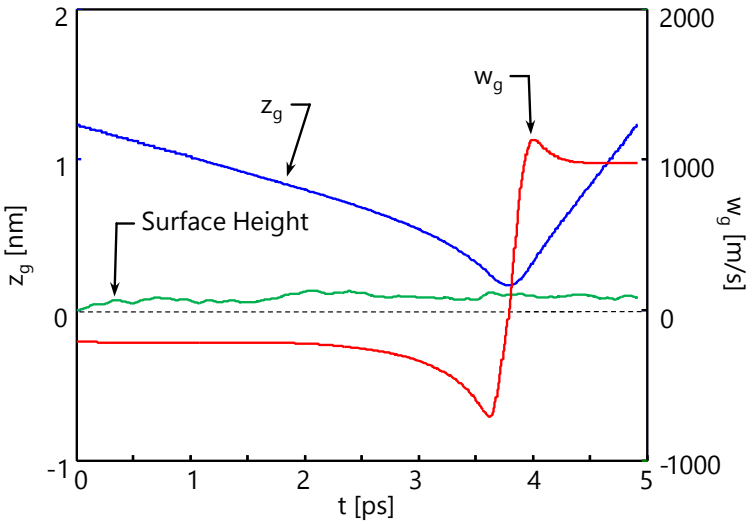

Figure 3-3: Trajectory of an argon atom scattering from a nickel surface where z_g and w_g are the absolute height and vertical speed of the argon atom.

3.2 Historical Treatment

This molecular dynamics technique has successfully been applied to several gas-surface pairs, mentioned above. The first study to quantity TACs for use in TiRe-LII was completed by Daun et al. [75] in 2009, using an in-house C++ code. In this study, the authors described the technique and applied it to five monatomic gases over sheets of graphite, chosen as a surrogate for soot. In these simulations, the boundaries of the cell were considered to be harmonic and the bottommost sheet of graphite was kept rigid to simulate the inertia of the larger soot particle. A harmonic and Morse (following Någård et al. [98]) potential were used to model the covalent bonds between carbon atoms within the hexagonally-structured graphite sheets and the dispersion forces that hold the graphene sheets together respectively. The potential between the gases and carbon were defined by the aforementioned Lennard-Jones 6-12 potential [99]

$$U_{gs}(r) = 4\varepsilon_{gs}\left[\left(\frac{\sigma_{gs}}{r_{gs}}\right)^{12} - \left(\frac{\sigma_{gs}}{r_{gs}}\right)^{6}\right] \qquad 3.8$$

where ε_{gs} and σ_{gs} are material dependent parameters defining based on the potential well depth and equilibrium distance respectively. In this case, the parameters determined using a method defined by Steele [100], in which the parameters were calculated based on experimental equilibrium distances and dissociation energies between the gas molecules and graphite. The

graphene sheets were heated using the aforementioned Lowe-Anderson thermostat [97] and allowed to equilibrate. The study found a good correlation between previous experimentally derived results [74] and MD results. Daun et al. also explored the dynamics of the gas-surface collision, including the number of times the gas atoms bounced across the surface, the distribution of scattering energy, and comparing the incident and scattering kernels.

Daun et al. [65] subsequently used the same technique to model the interactions between graphite and polyatomic gas molecules, including N_2, CO, N_2O, and CO_2, employing parameters from multiple sources [101,102,103,104,105], including the Lorentz-Berthlot combining rules described above in §3.1.1. This study included the added complexity of considering the rotational degree of freedom allowed in these molecules. The study primarily focused on the relative magnitude of the rotational and translational modes of energy transfer. They also showed good correlation to experimentally derived values [74].

Daun et al. [39,106] first examined non-carbonaceous surfaces in considering how argon would interact with nickel. In this case, the sheets of graphite were replaced by a face-centered cubic lattice of nickel atoms. The nickel atoms interacted using the relatively complicated quantum-corrected Sutton-Chen (QCSC) potential [107,108] defined as

$$U_{ij}\left(r_{ij}\right)=\varepsilon\sum_i\left[\frac{1}{2}\sum_{j\neq i}V\left(r_{ij}\right)-c\sqrt{\rho_i}\right] \tag{3.9}$$

where ε is related to the potential well depth, $V(r_{ij})$ is a pairwise potential describing the attraction between the atoms, defined by

$$V\left(r_{ij}\right)=\begin{cases}\left(a/r_{ij}\right)^n & \text{if } r_{ij}\le r_c\\ 0 & \text{if } r_{ij}>r_c\end{cases} \tag{3.10}$$

where r_c is the cutoff radius, and ρ_i is a many-body term accounting for the local electron density

$$\rho_i=\begin{cases}\sum_{k\neq i}\left(a/r_{ik}\right)^m & \text{if } r_{ik}\le r_c\\ 0 & \text{if } r_{ik}>r_c\end{cases} \tag{3.11}$$

There was particular difficulty in defining the potential between the nickel and argon atoms. As previously mentioned in §3.1.1, Daun et al. [39] initially attempted to use the Lennard-Jones 6-

12 potential employing the Lorentz-Berthelot combining rules. However, it was found that these parameters miss an important bond-order effect between nickel and argon, and consequently overpredict the potential well depth and TAC. To determine a more appropriate parameterization for the nickel-argon potential, *ab initio* simulations were performed in which quantum mechanics was used to solve for a suitable parameterization for the Morse potential (featuring a much shallower potential well). The resultant simulation revealed a great deal of accommodation proposed to be as a result of the Casmir-Polder forces [109], highlighting the need for accurate estimation of the gas-surface potential when calculating the TAC through molecular dynamics.

The TAC from these previous studies are summarized in Table 3-2 and plotted against the reduced mass, μ, in Figure 3-4. It is particularly useful to note the monotonically increasing trend observed in the monatomic gas molecules and the reduction in accommodation observed in more complex gas molecules, matching the experimental trends observed by Daun et al. [74].

3.3 Iron and Molybdenum: In-House Code

Simulations on molybdenum and iron were performed considering argon and helium using the same code created by Daun et al. [39] to simulate the interactions between nickel and argon.

Table 3-2: MD-derived thermal accommodation coefficients from prior studies [74,64,38,104].

Surface	Gas	$\mu = \mu_g/\mu_s$	α_{trans}		α_{rot}	α_{tot}
			α_{norm}	α_{tang}		
C [74,64]	He	0.33	0.22	0.22	-	0.22
	CH_4	1.32	0.59	0.08	0.19	0.11
	Ne	1.68	0.65	0.60	-	0.35
	CO	2.33	0.67	0.07	0.34	0.30
	N2	2.33	0.66	0.07	0.23	0.26
	C_2H_6	2.50	0.74	0.14	0.47	0.111
	Ar	3.33	0.77	0.06	-	0.45
	CO_2	3.67	0.68	0.09	0.48	0.20
	N_2O	3.66	0.68	0.08	0.48	0.19
	Kr	6.98	0.80	0.04	-	0.42
	Xe	10.9	0.86	0.04	-	0.45
Ni [92]	Ar	0.68	0.60	0.42	-	0.51

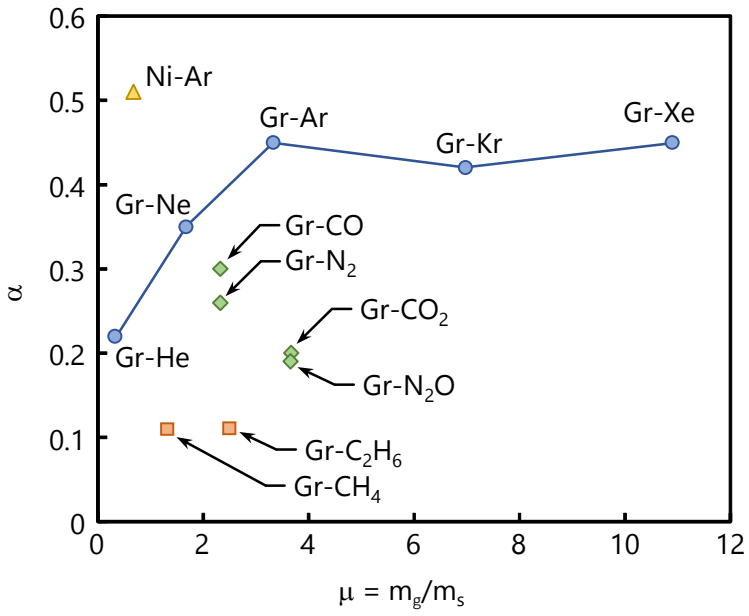

Figure 3-4: Historical molecular dynamics-derived thermal accommodation coefficients as a function of reduced mass for various surface pairs.

3.3.1 Simulation Setup

Interatomic potentials of metals are often expressed in terms of multi-body potentials such as embedded atom model (EAM) potentials which have the form

$$U_{tot} = \sum_i \left[\frac{1}{2} \sum_{j \neq i} V(r_{ij}) - c\sqrt{\rho_i} \right] \tag{3.12}$$

where U_{tot} is the total potential, r_{ij} is the distance between the i^{th} and j^{th} atoms, $V(r_{ij})$ is the pairwise (repulsive) potential between the i^{th} atom and the j^{th} atom, and ρ_i is the electron cloud density of the i^{th} atom,

$$\rho_i = \sum_{j \neq i} \phi(r_{ij}) \tag{3.13}$$

The functional form of $V(r_{ij})$ and $\phi(r_{ij})$ depend on the type of metal. The aforementioned Sutton-Chen potential [107,108], being an example of such a potential, uses

$$V_{ij}(r_{ij}) = \begin{cases} (a/r_{ij})^n & \text{if } r_{ij} \leq r_c \\ 0 & \text{if } r_{ij} > r_c \end{cases} \tag{3.14}$$

and

$$\phi(r_{ij}) = \begin{cases} (a/r_{ij})^m & \text{if } r_{ij} \le r_c \\ 0 & \text{if } r_{ij} > r_c \end{cases} \quad 3.15$$

with various parameterizations including the one used by Daun et al. [39], Cagin et al. [110], and Qi et al. [111] which corrected for quantum mechanical effects between the nickel atoms.

When considering body-centered cubic (BCC) metals, like iron and molybdenum, the Finnis-Sinclair (FS) potential [112,113] is often used and has successfully predicted the melting behavior of these metals [114]. In this potential, $V(r_{ij})$ is defined as

$$V(r_{ij}) = \begin{cases} (r_{ij} - c)^2 (c_0 + c_1 r_{ij} + c_2 r_{ij}^2) & \text{if } r_{ij} \le c \\ 0 & \text{if } r_{ij} > c \end{cases} \quad 3.16$$

and $\phi(r_{ij})$ is given by

$$\phi(r_{ij}) = \begin{cases} (r_{ij} - d)^2 + \beta \dfrac{(r_{ij} - d)^2}{d} & \text{if } r_{ij} \le d \\ 0 & \text{if } r_{ij} > d \end{cases} \quad 3.17$$

where the coefficients for molybdenum and iron, as given in Finnis and Sinclair [112,113], are summarized in Table 3-3.

3.3.2 Simulation Results

The resulting MD-derived thermal accommodation coefficients, including their normal and tangential components, are listed in Table 3-4. Each parameter is found by averaging 500 Monte

Table 3-3: The Finnis-Sinclair potential parameters used in the classical molecular dynamics simulations of iron and molybdenum [110,111].

	Fe	Mo
d [nm]	0.3569745	0.4114824
a [eV]	1.828905	4.114824
β	1.8	0
c [nm]	0.34	0.325
c_0	1.2371147	43.4475218
c_1	-0.3592185	-31.7665655
c_2	-0.0385607	6.0904249

Table 3-4: MD-derived thermal accommodation coefficients resulting from this study, with T_s = 2500 K.

Gas	$D/(k_B T_s)$	$\mu = m_g/m_s$	α_n	α_t	α
Fe/He	0.07	0.07	0.14 ±0.02	0.08 ±0.01	0.11 ±0.01
Fe/Ar	0.08	0.71	0.30 ±0.04	0.15 ±0.03	0.23 ±0.03
Mo/He	0.02	0.04	0.05 ±0.01	0.01 ±0.01	0.03 ±0.01
Mo/Ar	0.09	0.42	0.19 ±0.03	0.11 ±0.02	0.15 ±0.02

Carlo trials. Error bars correspond to two standard deviations of the mean. As noted in previous studies, α_n is consistently larger than α_t because the energized surface atoms oscillate primarily in the normal direction [75,65,106]. This effect is less pronounced for liquid surfaces (Fe, Ni) compared to solid surfaces (Mo, Gr), due to the increased surface roughness of the liquids.

The majority of pioneering TiRe-LII studies on metal aerosols focused on iron nanoparticles, particularly the Fe-Ar system. These studies each report different TACs: α = 0.33 [32]; α = 0.13 [33]; and α = 0.1 [35], which are generally in line with α = 0.23 ±0.03 found in this study. Eremin et al. [35] also report α = 0.01 for Fe/He, which is considerably smaller than the value found by MD, α = 0.11 ±0.03, although the relative magnitudes of the thermal accommodation coefficients reported in Ref. [35] for Fe/He and Fe/Ar follow the general trend of the MD-derived values.

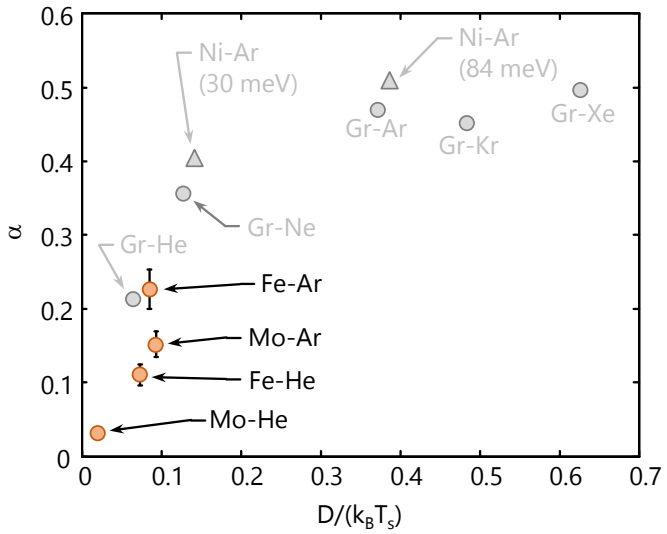

Figure 3-5: Thermal accommodation coefficient as a function of potential well depth for various gas surface pairs.

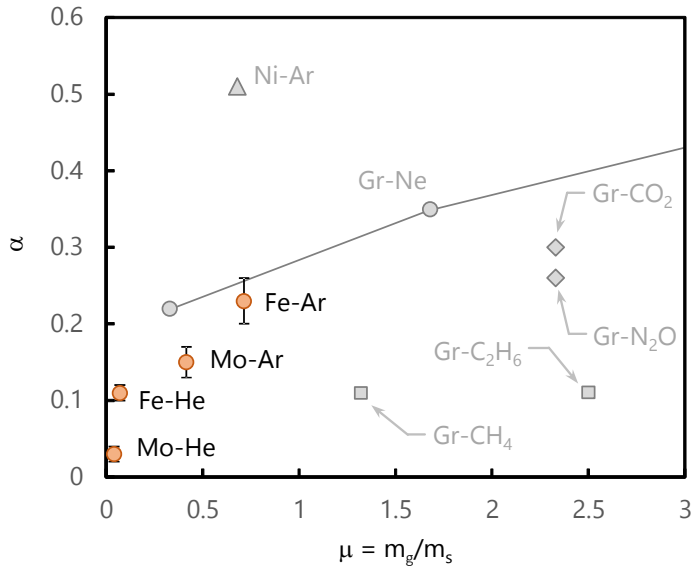

Figure 3-6: Thermal accommodation coefficient as a function of reduced mass for various gas surface pairs.

Figure 3-5 shows α plotted as a function of the potential well depth, D, scaled by $k_B T_s$, which represents the energy of the vibrating surface atoms. The TAC of the monatomic gases increases monotonically with potential well depth, but becomes less sensitive at large values of D. This trend is generally consistent with TACs for other systems as summarized in [72]. In classical gas-surface scattering theory (e.g. [115]) TACs are often presented in terms of the reduced mass, $\mu = m_g/m_s$. Figure 3-6 shows that α generally increases with respect to μ. This does not necessarily imply that μ plays a strong role in the collision dynamics, however, since D also tends to scale with μ. The exception to the trend is the Ni-Ar system. While some other gas-surface potentials are mainly due to dispersive effects, the Ni-Ar interaction is dominated by Casimir-Polder forces [109,116], resulting in a much deeper potential well compared to other gas-metal systems having a similar μ. This result suggests that D has a much larger effect on α compared to μ.

The relative influences of μ and D on α are investigated further through a parametric study on the Fe-Ar system. Figure 3-7 shows that the TAC increases with both μ and D, although α is more sensitive to D; also, however, the sensitivity of α to D drops with increasing D, which is consistent with the overall trend shown in Figure 3-5. The normalized sensitivities of α to μ and D are approximated by taking the derivative of a quadratic function fitted to the MD-derived TACs, as shown in Figure 3-7. The results show that, at the nominal values of μ and D for the Fe-Ar system, $\mu(\partial\alpha/\partial\mu) = 0.06$ and $D(\partial\alpha/\partial D) = 0.12$.

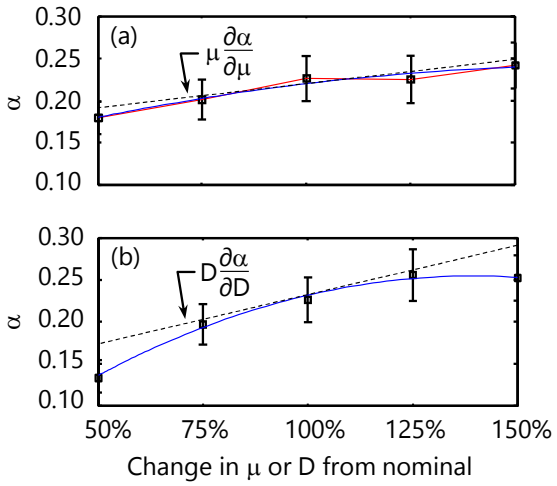

Figure 3-7: Sensitivity of α to (a) μ and (b) D for the Fe-Ar system.

Figure 3-8 shows the normal and tangential scattering energies across a range of initial gas temperatures. In cases where the surface is warmer than the gas, energy is transferred to the gas giving a total scattering energy greater than the initial gas energy. Conversely, it is observed that energy is transferred to the surface when the gas is warmer than the surface. This is expected in agreement with the 2nd Law of Thermodynamics. It is also observed that energy is preferentially transferred to and from the normal mode, matching what was observed for soot by Daun et al. [75]. The tangential mode for Fe-Ar is, however, considerably more important than for soot in that it accounts for a third of the total energy transfer. This discrepancy is likely cause by roughness in the surface due to the liquid phase of iron.

We also examine the sensitivity of α to D for the Ni-Ar system. As noted above, the Lorentz-Berthelot combining rules severely overestimate the true potential well depth for this system, resulting in a strong trapping/desorption channel and consequently near-perfect thermal accommodation [39]. The *ab initio* derived potential well depth of 83 meV is supported by Kao et al. [117] who inferred D = 84 meV based on the results of a low-energy molecular beam experiment. In contrast to these values, two older experimental studies, [118,119], reported in [120], cite a shallower potential well of 30 meV for the Ni-Ar system. We investigate this shallower potential by scaling a Lennard-Jones 6-12 pairwise potential to maintain the same equilibrium distance predicted by the Lorentz-Berthelot combining rules, but a potential well depth of 30 meV; this potential is also plotted above in Figure 3-1. This scaled potential results in α = 0.40 ±0.04, versus α = 0.50 ±0.04 using the DFT-derived value of D = 84 meV. Reducing D by

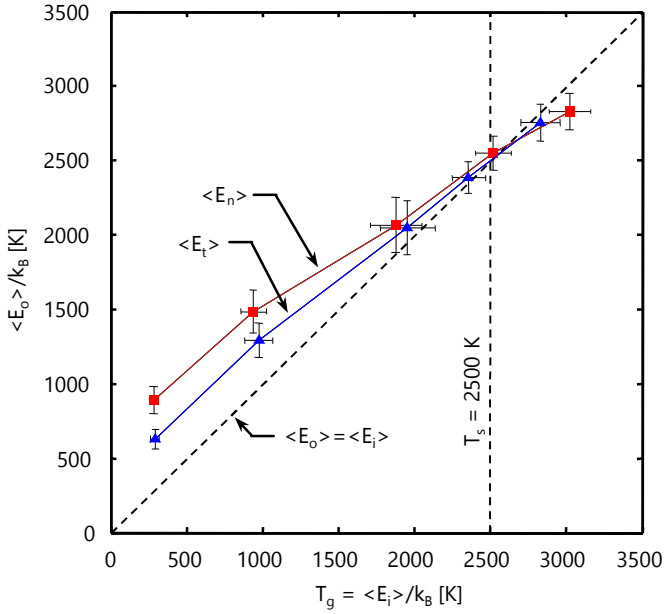

Figure 3-8: Total scattering energy as a function of gas temperature for the normal and tangential components of the gas velocity.

nearly 1/3 causes a small change in α compared to the Fe-Ar sensitivity study because the potential well depth for the Ni-Ar system is in the region where α is relatively insensitive to D as shown in Figure 3-5.

The most common and important source of uncertainty in DFT-calculated binding energies comes from the single particle approximation of the Kohn-Sham equations. Often, within the local density approximation (LDA) formulation of the exchange and correlation energy, this approximation tends to underestimate the binding energy. The extent of the underestimation varies, generally ranging from a few percent to 10% and above. Gradient corrections using the GGS to overestimation. Colleague's experience on carbonaceous materials [121], III-V semiconductors [122], and noble metals Au and Ag put the error to less than 8%. Another source of error, related to the method of linearized-augmented plane-wave used here, is related to the incompleteness of basis set. We have checked this by performing calculations with various values of the RK_{max} parameter (the product of the smallest muffin-tin radius in the system and the maximum plane-wave vector) and the total number of k-points in the irreducible Brillouin zone. The error resulting from this is below 0.5%. For the former source of error, attempts have been made to improve upon this. Among the methods used are many-body effects included through

the GW approximation [123] and empirical van der Waals correction (e.g. [124]) While this latter correction is straightforward, the former is extremely computationally expensive and is feasible only on systems made of few atoms. The empirical approach tends to strongly overestimate the binding energy of metal-noble gas pair as we have found for the case of Ni-Ar. Further discussion is deemed out of the scope of this work as it was primarily completed by a collaborator.

An additional source of uncertainty is the finite number of metal atoms used to represent the surface. To remain computationally-tractable, MD simulations must use far fewer atoms than would be contained in a moderately-sized metal nanoparticle; for example, a 30 nm nickel nanoparticle is composed of approximately 8 million nickel atoms. This could lead to two potential errors: underestimation of the potential well between the gas molecule and the surface; and an incorrect sampling of the dynamics of the laser-energized metal atoms due to the finite simulation domain. Periodic boundary conditions applied to the lateral surfaces of the metal contribute to an accurate representation of the potential well and ensure that the motion of the metal atoms in the MD simulation are representative of those in the nanoparticle.

3.4 Silicon: LAMMPS Code

Silicon was modeled using the open source Large-scale Atomic/Molecular Massively Parallel Simulator (LAMMPS) code [125], which provided a substantial time advantage over the previous in-house code and allowed access to various pre-built libraries. Again, the first step in performing a simulation is to define the interatomic potentials. The potential energy of the silicon atoms are defined using the Stillinger-Weber (SW) potential [126], consisting of two-body and three-body terms

$$U_{ij}\left(r_{ij}\right)=\frac{1}{2}\sum_{i}\sum_{j>i}\phi_2\left(r_{ij}\right)+\sum_{i}\sum_{j\neq i}\sum_{k>j}\phi_3\left(r_{ij},r_{ik},\theta_{ijk}\right) \tag{3.18}$$

The two body term, ϕ_2, describes the Si-Si bonding within the crystal

$$\phi_2=\varepsilon A\left[B\left(\frac{\sigma}{r_{ij}}\right)^p-\left(\frac{\sigma}{r_{ij}}\right)^q\right]\exp\left(\frac{\sigma}{r_{ij}-a\sigma}\right) \tag{3.19}$$

where r_{ij} is the distance between the i^{th} and j^{th} atoms. The three body term, ϕ_3, promotes the bond angle, θ_{ijk}, between three silicon atoms,

$$\phi_3 = \lambda\varepsilon\left(\cos\theta_{ijk} - \cos\theta_b\right)^2 \exp\left(\frac{\gamma\sigma}{r_{ij} - a\sigma} + \frac{\gamma\sigma}{r_{ik} - a\sigma}\right) \quad 3.20$$

The three-body component keeps the silicon crystal in its diamond structure below its melting temperature. The parameterization for the Stillinger-Weber potential [126], summarized in Table 3-5, has been shown to replicate the empirically-observed melting temperature and molten density of silicon [127]. To verify the physicality of the Stillinger-Weber potential for the range of temperatures important to TiRe-LII analysis, the simulation density was compared to the experimental density from electrostatic levitation measurements over a range of temperatures [128]. Figure 3-9 confirms that the density predicted by MD is within 10% of the experimentally-derived value over the temperature range important in TiRe-LII.

Figure 3-10a shows the progression of the initial warming process from a perfect silicon crystal lattice to an amorphous silicon molten surface at 2500 K and Figure 3-10b shows an argon molecule directly scattering from the silicon surface. For this MD study a surface temperature of 2500 K and gas temperature of 1300 K were considered to be representative of TiRe-LII conditions, following previous MD studies [75,65,39]. Under these conditions the accommodation coefficients for Si/He and Si/Ar were found to be 0.11 ±0.01 and 0.36 ±0.02 respectively, using 1500 Monte Carlo trials. (Uncertainties correspond to two standard

Table 3-5: Parameterization for the Stillinger-Weber potential for silicon [119].

Param.	Value
ε	2.17 eV
σ	0.201 nm
a	1.80
λ	21.0
γ	1.20
$\cos(\theta_b)$	−1/3
A	7.049556277
B	0.6022245584
p	4
q	0

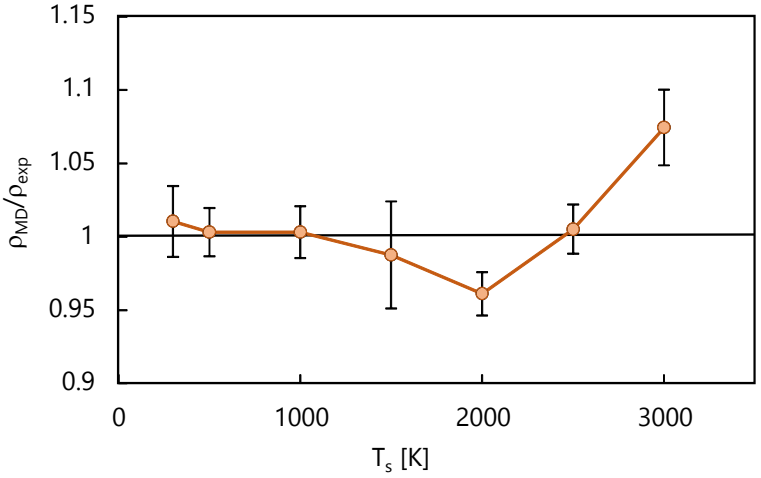

Figure 3-9: MD-derived density of molten silicon averaged over the final 5000 timesteps of the warming procedure, normalized by the published density over a range of surface temperatures [126].

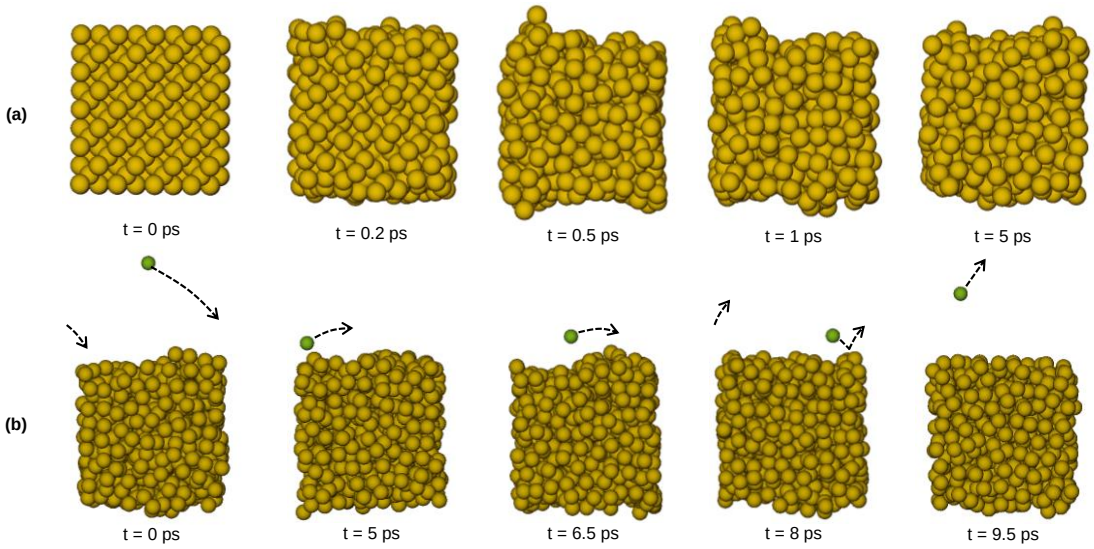

Figure 3-10: Visualization of the molecular dynamics simulation: (a) a Nosé-Hoover thermostat is used to transform the silicon surface from its initial crystal configuration to amorphous molten silicon at 2500 K, and; (b) an argon molecule scatters directly from the silicon surface. Illustrated particles sizes are 70% of the Van der Waals diameter.

deviations of the mean.) These results follow the same general trend seen in the thermal accommodation coefficients versus potential well depth and reduced molecular mass calculated between monatomic gases and metals and graphite [106], as shown in Figure 3-11.

The effect of gas temperature on the average energy transferred to the gas molecule, $\Delta E = \langle E_o - E_i \rangle$, is plotted in Figure 3-12 with T_s held at 2500 K. The change in translational normal and tangential energy components of the gas molecule are also plotted. While the increase in tangential translational energy is considerably less than the normal component, it is larger than that observed by Daun et al. between the graphite and both the monatomic gases [75] and N_2 [65]. This is almost certainly due to the comparatively greater surface roughness of liquid silicon

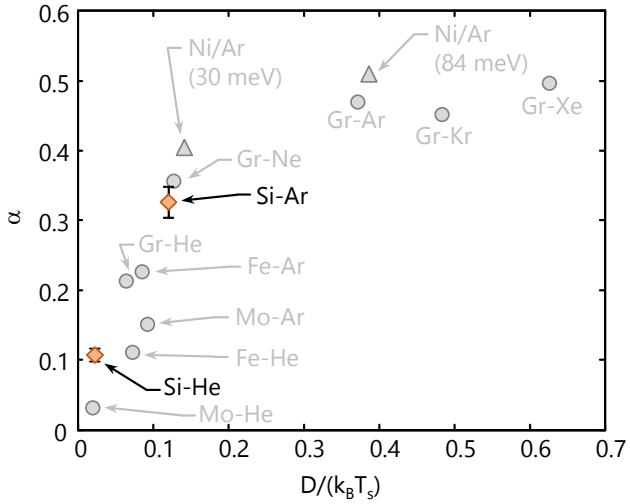

Figure 3-11: MD-derived values of α versus potential well-depth. Data for graphite is from ref. [74] and ref. [64], values for molybdenum, iron, and nickel is reported above in §3.3, and values for silicon are the present study.

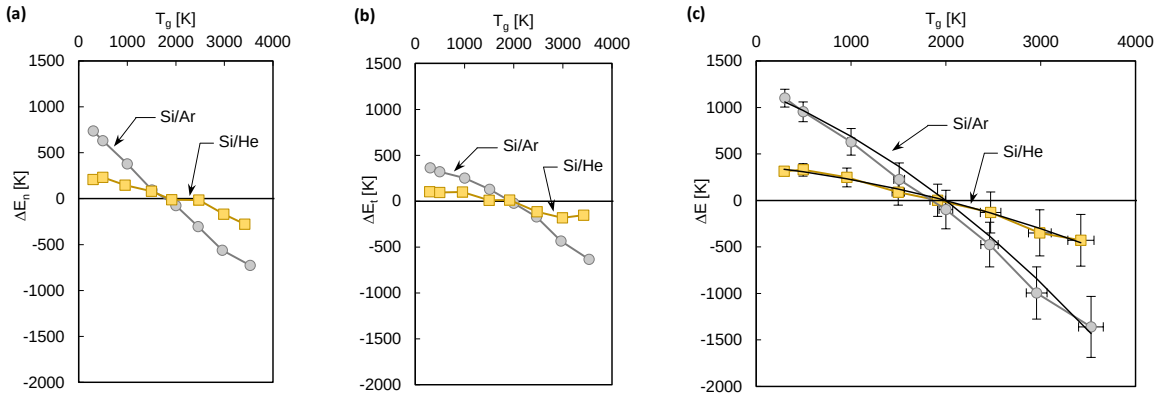

Figure 3-12: Variation of $\Delta E = \langle E_o - E_i \rangle$ of Si/Ar and Si/He with T_g at T_s = 2500 K decomposed into: (a) the normal component; (b) the tangential component; and (c) the sum of both components. Error bars correspond to two standard deviations of the mean.

compared to solid graphite. Similar trends were observed when comparing the MD-derived normal and tangential modes of the accommodation coefficients for molten Fe and Ni nanoparticles with those for molybdenum nanoparticles, which remain solid in TiRe-LII experiments. Figure 3-12 also shows that the average energy increase is zero when $T_s = T_g$, in accordance with the 2nd Law of Thermodynamics. The individual normal and tangential components of translational energy also appear to follow the same rule, suggesting that the normal and tangential modes of the gas molecule are uncoupled.

Figure 3-13 shows accommodation coefficients corresponding to change in gas molecular energies shown in Figure 3-12. Because the denominator of Eq. 3.7 becomes very small when $T_s \approx T_g$, a quadratic curve is fit to the points in Figure 3-12, and is forced to cross zero when $T_s = T_g$ in accordance with the 2nd Law. Substituting this expression into Eq. 3.7 gives a linear relationship between α and T_g that is plotted in Figure 3-13. The fitted curves generally lie within the error bounds (two standard deviations of the mean of the Monte Carlo trials) in the entire range of considered gas temperatures.

Figure 3-14 shows the simulated change in energy transfer considering surface temperatures from 200 K to 3000 K for T_g = 300 K. This plot reveals an inflection in the normal and tangential components of the gas molecular energies occurring when $T_s \approx T_{melt}$, represented by the vertical dashed line in Figure 3-14. This is expected, particularly for the tangential component, due to increased mobility of the surface atoms in the liquid state. Figure 3-14 shows that the thermal accommodation coefficients can be approximated by constant values above and below the melting temperature,

$$\alpha_{\mathrm{Si/Ar}} = \begin{cases} 0.100 & \text{if } T_s < T_m \\ 0.347 & \text{if } T_s > T_m \end{cases}$$
$$\alpha_{\mathrm{Si/He}} = \begin{cases} 0.078 & \text{if } T_s < T_m \\ 0.107 & \text{if } T_s > T_m \end{cases} \qquad 3.21$$

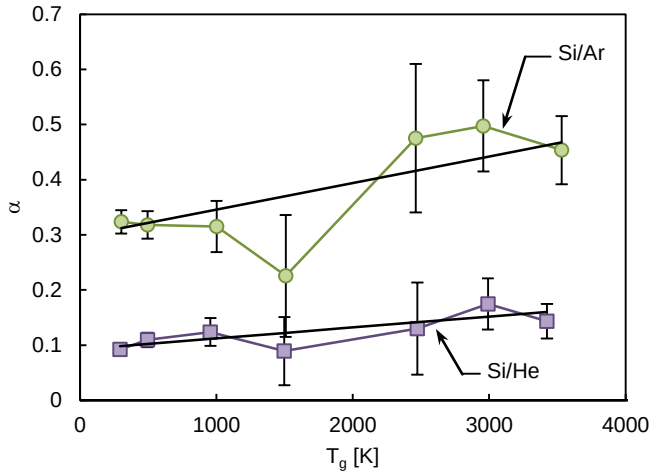

Figure 3-13: Variation of α for Si/Ar and Si/He with T_g at T_s = 2500 K.

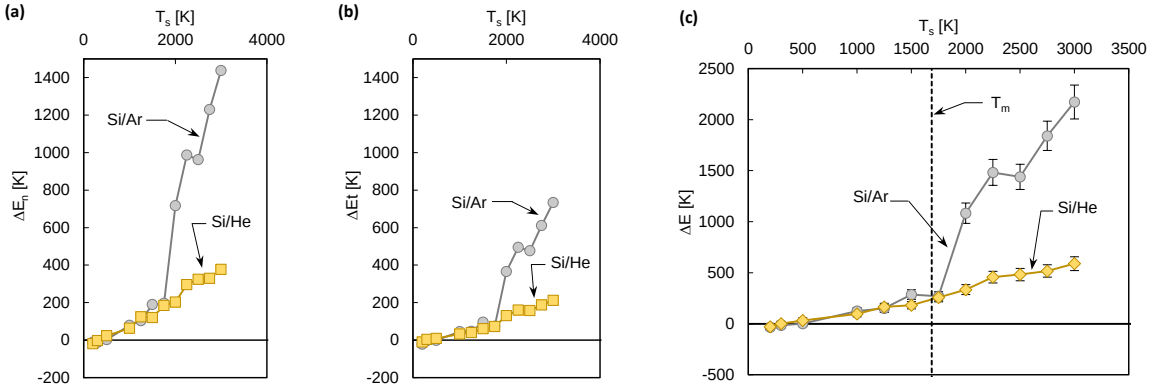

Figure 3-14: Variation of $\Delta E = \langle E_o - E_i \rangle$ of Si/Ar and Si/He with surface temperature at T_g = 300 K decomposed into: (a) the normal component; (b) the tangential component, and; (c) the sum of both components. Error bars correspond to two standard deviations of the mean.

with the change being considerably more dramatic for argon, likely due to the larger atomic diameter.

Chapter 4

TiRe-LII Data Analysis and Uncertainty Treatment

Independently calculating the TAC only goes so far in reducing the uncertainty in values inferred in TiRe-LII analyses. It is important, particularly when developing diagnostics, to have an understanding of the uncertainties associated with your mathematical models and to quantify them when possible. Most TiRe-LII analyses do not include any form of uncertainty in inferring parameters. When inferring the particle sizes of molybdenum, Murakami et al. [45] included error bounds on the particle sizes with little discussion of their origin or what they include. Analysis on the data in this work and summarized in [129], also shows that these results are very ill-posed to the point that the particle size is not recoverable in helium and uncertain in the other gases. In the studies on iron nanoparticles by Kock et al. [33] and Eremin et al. [35], particle sizes were inferred by naive least squares and not accompanied by any form of error bounds. This is very important to note in particular in the case of Kock et al. [33], in which the TAC is inferred simultaneous to the particle size, a method that will later be shown to be unreliable on most materials. The present chapter gives some background on statistical treatment of TiRe-LII problems in the past and discusses how the various kinds of uncertainty influence TiRe-LII analysis. In particular, this chapter distinguishes between aleatoric uncertainties, statistical uncertainty inherent to a particular phenomenon, and epistemic uncertainties, uncertainties resulting from a lack of knowledge about a phenomenon [130,131]. Where possible, the present work puts forward statistically-robust methods to be applied in analyzing TiRe-LII data.

4.1 Aleatoric Uncertainty

Aleatoric uncertainty is uncertainty that is intrinsic to a given phenomenon [130,131]. In this case, we consider what Kennedy et al. [132] refer to as experimental and structural uncertainty, that is, uncertainty resulting from randomness inherent to the data and uncertainty resulting from inadequacy or bias within mathematical models.

Roth and Filippov [133] were one of the first to notice the role of this uncertainty in TiRe-LII measurements. They identified that when considering polydisperse distributions in TiRe-LII problems, Eq. 2.1 can be expressed as a Fredholm integral equation of the first kind

$$J_\lambda(t) = \int_0^\infty K(d_p, t) P(d_p) d(d_p) \tag{4.1}$$

where the kernel, $K(d_p,t)$ is given by

$$K(d_p, t) = C \frac{\pi d_p^2}{4} Q_{abs,\lambda}(d_p) I_{b,\lambda}\left[T_p(t, d_p)\right] \tag{4.2}$$

These problems are well-known for being ill-posed where there is a great deal of uncertainty in any inferred solution. In particular, it can be observed that smaller particles in a distribution are overwhelmed by incandescence emitted by larger particles. As such, signal noise makes it very difficult to discern small changes in the distribution shape at smaller particle sizes. Roth and Filippov attempt to solve this problem using regularization in a minimization scheme developed by Twomey [134] and improved by Markowski [135], which, although accounting for noise while inferring solutions, was not used to develop credibility intervals (or uncertainty) for inferred parameters.

More recent work by Daun et al. [48], examined solution schemes for solving TiRe-LII problems, initially describing naïve least squares before moving to more complicated minimization schemes. They generated figures such as Figure 4-1 that graphically showed how there is a large range of solutions that could satisfy Eq. 4.2 in TiRe-LII experiments. The authors suggest that this set of solutions may in fact be described by a single parameter, the Sauter mean diameter, d_{p32}, which for a lognormal distribution is given by

$$d_{p,32} = \frac{\int_0^\infty d_p^3 P(d_p) \mathrm{d}\, d_p}{\int_0^\infty d_p^2 P(d_p) \mathrm{d}\, d_p} = d_{p,g} \exp\left[\frac{5}{2} \ln\left(\sigma_g\right)^2\right] \tag{4.3}$$

Although, as Figure 4-1 shows, Eq. 4.3 is not perfectly aligned with the valley of solutions, the authors do show how this could potentially improve the robustness of inferring parameters from TiRe-LII data.

In all of these observations, very little work has been done to quantify the aleatoric uncertainty of values inferred in TiRe-LII analyses. The present work includes the first attempts to apply

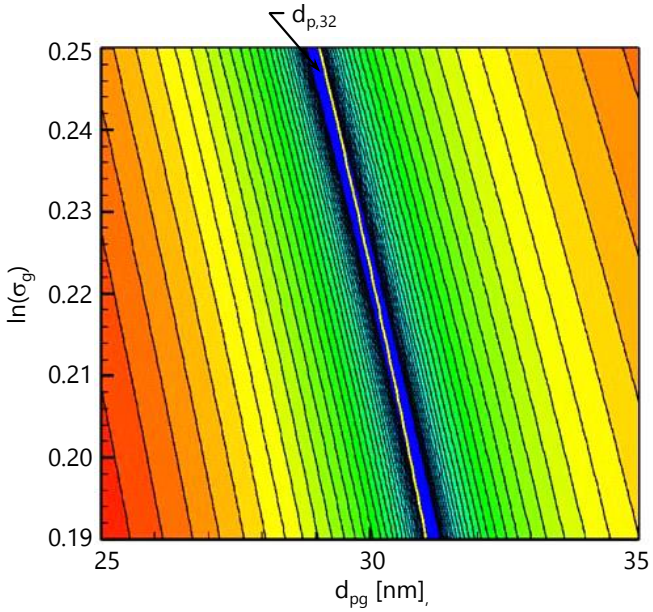

Figure 4-1: Contour plot portraying the sum of the square of residuals for solutions with different values of σ_g and $d_{p,g}$ in the lognormal distribution. The line in the valley of solutions with low residual represents a set of solutions that shares a single $d_{p,32}$ as defined by Eq. 4.3. This plot is taken from Daun et al. [135].

various techniques to both quantify and best accommodate these uncertainties into TiRe-LII analyses.

4.1.1 Bayesian Framework

The Bayesian framework is a structure in which the true state of system is defined based on probabilities or degrees of belief. Charnigo et al. [136] generally show how one could apply this framework to quantify aleatoric uncertainty while inferring nanoparticle characteristics from laser-based diagnostics. In particular, they show how one can estimate credible intervals on the nanoparticle size for surface plasmon-polariton scattering measurements. The subsequent paragraphs disucss the framework and how it will be applied to TiRe-LII measurements.

In the Bayesian approach, the posterior probability, $P(\mathbf{x}|\mathbf{b})$, of the hypothesized set of unknown parameters, such as $\mathbf{x} = [d_{p,g}, \sigma_g]^T$, is defined by

$$P(\mathbf{x}|\mathbf{b}) = \frac{P(\mathbf{b}|\mathbf{x})P_{pr}(\mathbf{x})}{P(\mathbf{b})} \tag{4.4}$$

where $P(\mathbf{b}|\mathbf{x})$ is the likelihood of the observed data in **b** occurring for a hypothetical **x**, $P_{pr}(\mathbf{x})$ is the probability of **x** being correct based on prior knowledge of the distribution parameters, and $P(\mathbf{b})$ scales the posterior probability so that the Law of Total Probability is satisfied. If the spectral incandescence data is contaminated with independent, normally-distributed error, the likelihood is given by

$$P(\mathbf{b}|\mathbf{x}) = \prod_i \frac{1}{\sqrt{2\pi\sigma_i^2}} \exp\left[-\left(\frac{b_{exp,i} - b_{mod,i}}{\sqrt{2}\sigma_i^2} \right)^2 \right] \tag{4.5}$$

where σ_j is the expected standard deviation of the measured incandescence at the j^{th} measurement time and **b** can be either the incandescence signal or effective temperature. It is often more effective to use the log likelihood and state the likelihood as a sum rather than a product

$$\ln\left[P(\mathbf{b}|\mathbf{x}) \right] = \sum_i \ln\left[\frac{1}{\sqrt{2\pi\sigma_i^2}} \right] - \sum_i \left(\frac{b_{exp,i} - b_{mod,i}}{\sqrt{2}\sigma_i} \right)^2 \tag{4.6}$$

The standard deviation is expected to increase at longer cooling times, as the signal-to-noise ratio in the incandescence traces drops [137].

The prior probability is constructed as the product of three restrictions: (i) $d_p > 0$ or equivalently, in the case of a lognormal distribution, $d_{p,g} > 1$; (ii) $\sigma > 0$ or equivalently, in the case of a lognormal distribution, $\sigma_g > 1$; and (iii) $0 \le \alpha \le 1$. In the present work, the given parameters are allowed to hold any value outside of the restricted range without discrimination, a uniform distribution is defined in those regions such that the prior is given by

$$P_{pr}(\mathbf{x}) = \begin{cases} 1 & \text{if } \left\{ \mathbf{x} | \left(d_{p,g} > 0 \right) \bigcap \left(\sigma_g > 1 \right) \bigcap \left(0 \le \alpha \le 1 \right) \right\} \\ 0 & \text{else} \end{cases} \tag{4.7}$$

As the distributions are uniform within certain ranges, if any algorithm is restricted to those regions independently, the prior performs no function resulting in

$$P(\mathbf{x}|\mathbf{b}) \propto P(\mathbf{b}|\mathbf{x}) \tag{4.8}$$

Additional priors could be introduced depending on the circumstances, however are generally not required as the distribution shape is generally specified restricting the number of unknown variables.

4.1.2 Bayesian Inference

The simplest method of inferring parameter from experimental data used in TiRe-LII analysis is least squares fitting. In this method, parameters are inferred based on how they minimize the square of the residual. In this application of the Bayesian framework, this is equivalent to maximizing the posterior distribution that is, finding the maximum a posteriori (MAP) estimate. Given Eqn. 4.8, the MAP becomes equivalent to the maximum likelihood estimator (MLE) given by

$$\arg\max\left[P(\mathbf{b}|\mathbf{x})\right] = \arg\max\left\{\ln\left[P(\mathbf{b}|\mathbf{x})\right]\right\} = \arg\min\left\|\frac{b_{exp,i} - b_{mod,i}}{\sigma_i}\right\|_2^2 \tag{4.9}$$

which is equivalent to weighted least squares where the weight is inversely proportional to the noise in the experimental data at each data point. Historically, TiRe-LII practitioners have normally applied naïve least squares to problems, making this approach more robust than the typical analysis. In this work, this least squares problem is solved using the Levenberg-Marquardt algorithm [138,139], a non-linear minimization technique summarized in greater detail in Appendix C.

4.1.3 Inferred Parameter Uncertainty

One of the major advantages to the Bayesian framework is that it allows for an easy way to define uncertainty resulting from the model definition and experimental noise. In particular, this section examines methods for sampling from the distribution $\pi(\mathbf{x})$, where in general

$$\pi(\mathbf{x}) \equiv P(\mathbf{x}|\mathbf{b}) \tag{4.10}$$

where a set of generated samples

$$\left\{\mathbf{x}_1, \mathbf{x}_2 \ldots \mathbf{x}_n\right\} \sim \pi\left(\mathbf{x}\right) \tag{4.11}$$

Having estimated $\pi(\mathbf{x})$, uncertainty can be specified by defining a credibility interval, [$\mathbf{a}_1$, $\mathbf{a}_2$], within which there is a specified percentage that the true value of $\mathbf{x}$ exists. Since $\pi(\mathbf{x})$ may be asymmetric, it is useful to define the credible interval using the highest density region (HDR) or highest density probability as suggested by Chen et al. [140]. In this case, various algorithms generate the aforementioned samples and credibility intervals are specified such that the interval [$\mathbf{a}_1$, $\mathbf{a}_2$], contains the highest density of samples while satisfying the percentage criterion. For example, the highest density 95% credibility interval is defined mathematically as

$$\left[\mathbf{a}_1, \mathbf{a}_2\right] = \left\{\mathbf{x} \in \mathbb{R} \,|\left[\pi\left(\mathbf{a}_1\right) = \pi\left(\mathbf{a}_2\right)\right] \cup \left[\int_{a_1}^{a_2} \pi\left(\mathbf{x}\right) d\mathbf{x} = 0.95\right]\right\} \tag{4.12}$$

This region can be quantified from the set of sample {$\mathbf{x}_1$, $\mathbf{x}_2$, … $\mathbf{x}_n$} using the density quantile approach suggested by Hyndman [141]. Subsequent paragraphs summarize the sampling techniques that are used in the work.

Although it can be done in a Bayesian framework, bootstrapping does not require the Bayesian framework in order to estimate uncertainty [142]. Having regressed a solution to a given problem, bootstrapping involves resampling the residuals between the experimentally collected signals and the signal representative of the regressed solution. Resampling these residuals allows one to reconstruct an artificial experimental signal with noise that is representative of the original signal. Regressing to artificial signals allows one to generate samples that are expected to be representative of the uncertainty resulting from measurement noise that transfer through the mathematical model. Although this treatment requires that the data be independent and identically distributed (i.i.d.), there are methods, such as studentizing the residuals [143], that can scale residuals that do not fit this criterion such that bootstrapping can still be used. Bootstrapping is generally considered the *quick-and-dirty* way of estimating credible interval.

Alternatively, one can apply robust Bayesian analysis by using Marcov Chain Monte Carlo (MCMC) to sample from the posterior distribution. MCMC generates a chain of samples where each subsequent sample is generated by adding information from only the current sample. Although there is a local correlation between samples, it can be shown that on the grander scale, the Metropolis-Hastings algorithm effectively samples randomly from the posterior distribution

such that Eq. 4.11 is satisfied. More specific information on MCMC and the Metropolis-Hasting algorithm are given in Appendix C.

In TiRe-LII analysis, one frequently considers two unknown parameters. When this is the case, the easiest way to visualize the optimal pairing is to generate a map of the χ^2 function as a function of the two variables

$$\chi^2 = \sum_i \frac{\left(x_i - \mu_i\right)^2}{\sigma_i^2} \qquad 4.13$$

which is proportional to the negative log-likelihood. Figure 4-1 is an example of such a plot. The result is a map showing which combinations of the parameters yield the least residual and which combinations yield the greatest residual. One can also overlay samples collected by the above methods to visualize how they reflect the contours of solution. Figure 4-2, for example, shows the contours resulting from simultaneous inferring the lognormal distribution parameters, $d_{p,g}$ and σ_g for a set of Si-Ar data. The circles represent a set of samples created using the Metropolis-Hastings algorithm. The plot shows that the samples follow the surrounding contours. The histograms on either axis show the density of points in different bins, which form the basis for

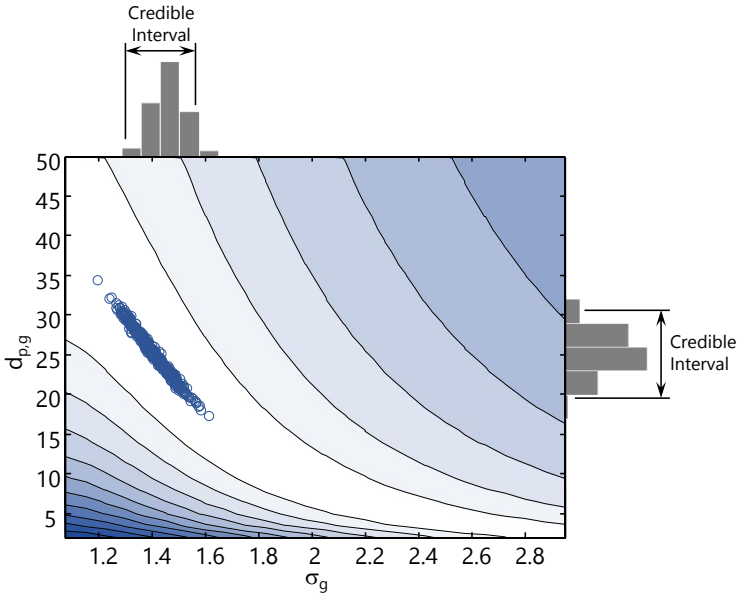

Figure 4-2: Contour plot showing the residual between the modeled and experimentally-measured T_{eff} for various values of x = $[d_{p,g}, \sigma_g]^T$. Circles represent MCMC samples that can be used to estimate uncertainty when inferring values of x.

establishing credibility intervals. The present work uses these residual maps as a way to visualize the uncertainty in inferred parameters.

4.2 Epistemic Uncertainty

Epistemic uncertainty refers to uncertainties resulting from a lack of knowledge that could, in theory, be reduced [130,131]. However, due to practical limitations, such as time or resources, these uncertainties have not been reduced and translated through the modeling process. These can be further categorized into: (i) parameter uncertainty, resulting from input parameters that are unknown or uncontrolled in experiments; (ii) parameter variability, resulting from input parameters that are known or controlled but have an uncertainty associated with their values; (iii) algorithmic uncertainties, resulting from numerical approximations in the mathematical models; and (iv) interpolation uncertainties, resulting from estimations of parameters by filling in gaps between available data [132].

4.2.1 Parameter Uncertainty and Variability

Parameter uncertainty and variability is very much dependent on the circumstance being considered. In TiRe-LII experiments, it can vary from uncertainties in the value of density at a specific temperature to errors in thermocouple measurements of the gas temperature. With the plethora of possible manifestations, it becomes difficult to estimate the uncertainty in any particular input parameter. This is further complicated by the fact that these uncertainties do not transfer through TiRe-LII models to inferred parameters in a linear fashion.

In 2011, Crosland et al. [144] examined uncertainty in laser-induced incandescence measurements due to nuisance parameters, including the optical constants and the TAC. The authors employed a Monte Carlo technique, sampling the input parameters from heuristically predefined distributions ranging from uniform distributions between two constants and normal distributions with a set mean and standard deviation. As a result, the authors estimated the uncertainty in the soot volume fraction based on the nuisance parameters.

Eremin et al. [36] took a lightly different approach. Having heuristically estimated variance in various input parameters, the authors perturbed the input parameters from their expected value by the specified variance. Repeating the minimization, the authors determined how much the perturbation of each parameter will influence the inferred values. They then create Figure 4-3

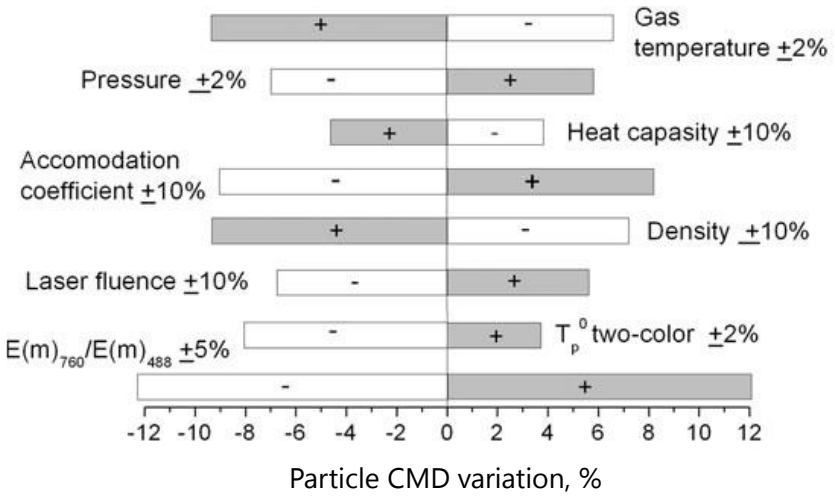

Figure 4-3: Sensitivity of the count median diameter inferred in a TiRe-LII experiment to various input parameters. Figure taken from Eremin et al. [35].

showing the percentage change in the inferred parameter, in this case the count median diameter, which for a lognormal distribution is equal to its geometric mean, $d_{p,g}$.

In this work, the impact of these uncertainties on the inferred parameters is assessed through a perturbation analysis, in which the local sensitivities (for example $[\partial d_{p,g}/\partial T_i]\cdot T_i$) are estimated through a central finite difference approximation. Values are generally stated in terms of the relative sensitivity coefficients, that is, the product of the local sensitivity and the nominal model parameter value. The error in an inferred parameter, x, due to uncertainty in a model parameter, ϕ, can be found using

$$\varepsilon(x|\phi) = PE(\phi)\times RSC(\phi,x) = PE(\phi)\times\left[\phi\frac{\partial x}{\partial\phi}\right]_{\phi_0} \qquad 4.14$$

where ε is the error in the units of the inferred parameter, PE is the percentage error in a model parameter, and RSC is the relative sensitivity coefficient.

4.2.2 Algorithmic Uncertainty

Within TiRe-LII models, algorithmic or numerical uncertainty is expected to be dominated by discretization error resulting from numerical integrations through time, wavelength, and particle size. As errors resulting from the other uncertainties are considered to be much more prominent

than any numerical errors resulting from these techniques, these uncertainties are generally ignored and do not receive any additional attention in the present work.

4.2.3 Interpolation Uncertainty

In the present TiRe-LII analysis, interpolation uncertainty may come into play in two ways. First, data collection on the nanosecond time scale may be influenced by data shift where the transmission of collected signals causes a delay in one or more of a multichannel signal. As a result, there may be an error resulting when calculating temperatures based on Eqn. 2.6 or Eqn. 2.7 while assuming that the signal were collected at exactly the same time. This error is expected to be very small except in cases where there are very dramatic changes in the particle temperature and signal intensity, as is the case during laser heating. Second, the optical properties are taken from literature where the values at any given wavelength are inferred based on linear interpolation between experimentally collected data points. As the optical properties are unlikely to change linearly between these points, this introduces a small amount of uncertainty. However, as temperature and other experimental conditions are expected to have a more dramatic effect on uncertainty in the optical properties, these errors are neglected in subsequent analysis.

Chapter 5

TiRe-LII Analysis of Molybdenum Nanoparticles

One of the earliest applications of TiRe-LII for sizing metal nanoparticles was by Murakami et al. [45] in 2005. In this work molybdenum nanoparticles were formed by laser-induced photolysis of a variety of bath gases doped with $Mo(CO)_6$. A second laser pulse was then used to carry out TiRe-LII on these nanoparticles. In their analysis, the authors derived a pyrometric effective temperature by fitting a blackbody distribution to the measured spectral incandescence. Particle sizes were then inferred by regressing simulated pyrometric temperatures, calculated using a heat transfer model, to the experimental data.

Unfortunately, subsequent progress in LII science has revealed several shortcomings in the authors' analysis of their data: (i) the fitting procedure used to derive the pyrometric temperature neglected the fact that the absorption efficiency for nanoparticles in the Rayleigh regime is inversely proportional to wavelength [49]; (ii) the particle sizes were assumed to be monodisperse, when in reality they are likely polydisperse [145]; (iii) particle cooling rates were calculated using an early heat transfer model from Roth and Filippov [133], which implicitly assumes $\alpha = 1$ (not likely true [31]) and $\gamma = 5/3$ (only true for monatomic gases); and (iv) the temperature-dependence of various gas and particle properties, which are important given the wide range temperatures during LII, were neglected.

This chapter presents a heat transfer model for molybdenum nanoparticles to facilitate re-interpretation of the TiRe-LII data from the experiment described in Ref. [45]. The model is used to produce simulated pyrometric temperatures, which are compared to experimental temperatures found by robust regression of spectral incandescence measurements made throughout the cooling process. It is useful to note that not all of the methods below identically reflect the ideas described in previous chapters (wild bootstrapping and the sensitivity analysis for example). As this work was completed early in the progress of my degree, some methods have evolved or been modified over the duration of completing my degree.

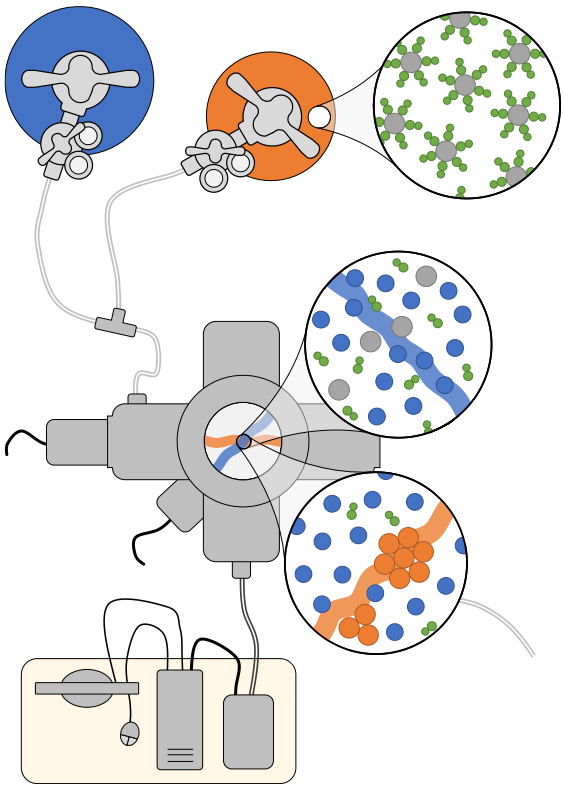

Figure 5-1: Experimental apparatus used in Ref. [38] including molybdenum nanoparticle formation through photolysis, and subsequent LII excitation.

5.1 Experimental Procedure

In their original experimental study, Murakami et al. [45] generated molybdenum nanoparticles within a reactor containing an inert buffer gas at 60 kPa (600 Torr), doped with small amounts of $Mo(CO)_6$. Molybdenum nanoparticle photolysis was initiated using a pulsed Nd:YAG laser operating at 266 nm. In the photolysis process, photons from the laser pulse dissociate the $Mo(CO)_6$ molecules into free molybdenum atoms, which then coalesce into nanoparticles through intermediate collisions with the bath gas molecules. One microsecond after the photolysis laser pulse, the mixture was irradiated with a second pulse from a Nd:YAG 1064 nm laser to produce particle incandescence. As the laser-energized nanoparticles return to the ambient gas temperature of 300 K, the incandescence signal was measured at 100 ns intervals at shorter cooling times and 500 ns intervals at longer cooling times using an intensified CCD detector

(Anchor DH501) with a multichannel imaging spectrograph (Oriel model 77441). The experimental apparatus and photolysis/LII process are summarized in Figure 5-1.

5.1.1 Interpretation of Spectral Data

The spectrally resolved incandescence was converted to a set of temperatures by regressing Eq. 2.6, repeated below for reference, with $\mathbf{x} = [C_2, T_{eff}]^T$, to the experimental data kindly provided by Prof. Y. Murakami.

$$J_\lambda(t_i) = C_2(t_i)\frac{E(\mathbf{m}_\lambda)}{\lambda} I_{b,\lambda}\left[T_{eff}(t_i)\right] \qquad 5.1$$

An example fit is shown in Figure 5-1. The signal-to-noise ratio drops with increasing wavelength due to the diminishing spectral intensity of the nanoparticles, and the intensity data was truncated at 650 nm due to the extreme amount of noise beyond this threshold. To account for the wavelength-dependent measurement noise a robust regression procedure [146] was used that weighted the spectral incandescence data based on the estimated uncertainty of the data at a particular wavelength.

The polydispersity of particle sizes also causes $C_2(t_i)$ to change with measurement time. Since the nanoparticles are heated to approximately the same peak temperature, $T^{eff}(t)$ closely

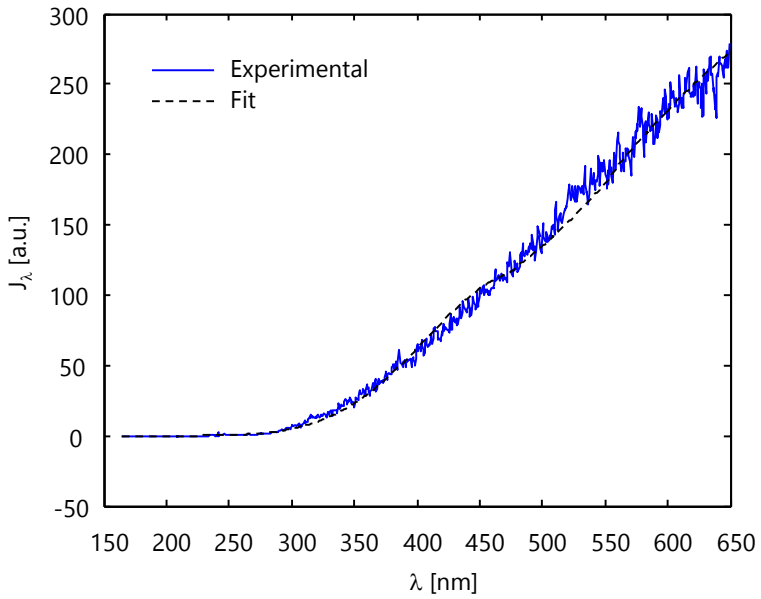

Figure 5-2: Calculation of Teff(t) by robust regression of the spectroscopic incandescence data, Eq. 2.6.

approximates the true particle temperature at short cooling times. The size-dependent cooling rate of the nanoparticles, however, means that the distribution width of $T_p(t)$ increases with time. Consequently, the residual between Eq. 2.6, which effectively models the aerosol particles as isothermal, and the true spectral incandescence distribution will grow with increasing cooling time, causing $C_2(t)$ to change. The resulting set of experimentally-derived effective temperatures is then used as a basis for particle sizing by minimizing the least-squares function, previously given by Eq. given $b_j = T_{eff,j}$,

$$F(\mathbf{x}) = \sum_{j=1}^{n} w_j \left[T_{eff,j}^{exp} - T_{eff,j}^{mod}(\mathbf{x}) \right]^2 \tag{5.2}$$

where, in this case, the elements of **x** specify $P(d_p)$. As mentioned previously in §2.1, most often, the coalescence and aggregation in the aerosol give rise to a self-preserving size distribution, which can be modeled as lognormal [34],

$$P(d_p, \mathbf{x}) = \frac{1}{d_p \sqrt{2\pi (\ln \sigma_g)^2}} \exp\left[-\frac{(\ln d_p - \ln d_{p,g})^2}{2(\ln \sigma_g)^2} \right] \tag{5.3}$$

where $\mathbf{x} = [d_{p,g}, \sigma_g]^T$. The modeled effective temperature is generated by numerically solving Eq. 2.1

$$J_\lambda(t) = C \int_0^\infty \frac{\pi d_p^2}{4} P(d_p) Q_{abs,\lambda}(d_p) I_{b,\lambda}\left[T_p(t, d_p) \right] d(d_p) \tag{5.4}$$

where T_p is evaluated by numerically solving a simplified form of Eq. 2.9

$$\frac{dT_p}{dt} = \frac{6}{\rho c_p \pi d_p^3} \left[-q_{cond}(t, d_p) \right] \tag{5.5}$$

for values of d_p chosen based on discretization on the integration algorithm. Simplification of Eq. 2.9 to only considering conduction is based on plots in §2.2.4 showing that the other heat transfer modes are negligible.

5.2 Material Properties

5.2.1 Optical Constants

Solving Eq. 5.7 requires knowledge of the adsorption coefficient, $Q_{abs,\lambda}$ previously defined by Eq. 2.5

$$Q_{abs,\lambda}\left(d_p\right) \equiv -4xE\left(\mathbf{m}_\lambda\right) \tag{5.6}$$

The complex absorption function, $E(\mathbf{m}_\lambda)$, along with the real and imaginary indices of refraction, of molybdenum are plotted as a function of wavelength up to 0.6 μm, the maximum wavelength reported by Juenker et al. [147], in Figure 5-3. Error bars are not included for clarity, but the authors report experimental uncertainties of 5% for both n_λ and k_λ. Values of n_λ and k_λ measured at room temperature [51] along with the corresponding $E(\mathbf{m}_\lambda)$ are also included to illustrate the temperature-dependence of these parameters. Figure 5-3 shows that, although both data sets exhibit a peak in $E(\mathbf{m}_\lambda)$ at short wavelengths followed by a monotonic decay, the high temperature data shows this peak value to be smaller in magnitude compared to the room temperature data, and occurs at a shorter wavelengths. This result is consistent with the

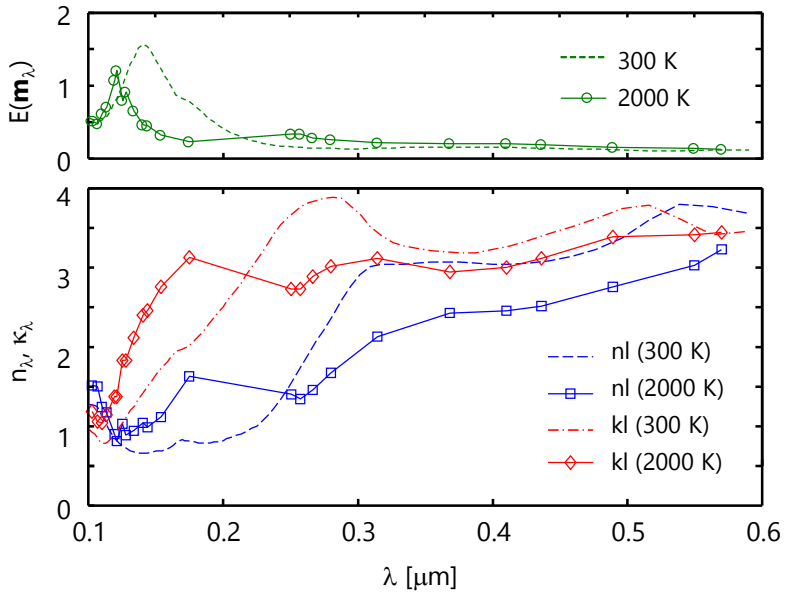

Figure 5-3: Indices of refraction and the absorption function for molybdenum at 2200 K [140] and 300 K [44].

expected trend of n_λ and k_λ with temperature, since the wavelengths important to incandescence are shorter than the crossover point for this metal [148]. At wavelengths longer than the crossover point of the metal, absorptivity increases with temperature according to Hagen-Rubens theory, while at shorter wavelengths the absorptivity drops [50]. The data from Palik et al. [51] shows $E(\mathbf{m}_\lambda)$ to be approximately constant in the near infrared, so in our analysis $E(\mathbf{m}_\lambda)$ is taken to be 0.14 for wavelengths longer than 0.6 μm.

5.2.2 Sensible Heat Properties

The density and specific heat of molybdenum at various temperatures, needed to solve the left hand side of Eq. 5.5, are given by Paradis et al. [149]

$$\rho(T) = \begin{cases} 9100 - 0.6(T - T_m) & \text{if } T \geq T_m \\ 9100 - 0.5(T - T_m) & \text{if } T < T_m \end{cases} \tag{5.7}$$

and

$$c_p(T) = \begin{cases} 56.5 + 0.01177(T - T_m) & \text{if } T \geq T_m \\ \left[1582.03 + 0.0589(T - T_m)\right] \times \left[0.29 + 9.89 \times 10^{-4}(T - T_m)\right] & \text{if } T < T_m \end{cases} \tag{5.8}$$

where T_m = 2898 K is the melting point of molybdenum.

5.2.3 Conduction Properties

The conduction heat transfer is given by Eq. 2.19

$$q_{cond}(t, d_p) = \alpha \pi d_p^2 \left(\frac{p_g c_{g,t}}{4T_g} \right) \left(2 + \frac{\zeta_{rot}}{2} \right) (T_p - T_g) \tag{5.9}$$

Subsequent calculations will use α = 0.15 for Mo-Ar and α = 0.03 for Mo-He, found using molecular dynamics discussed in §3.3. The gas pressure and temperature are determined by the experimental conditions: P_g = 60 kPa and T_g = 298 K [45]. The rotational degrees of freedom are assigned values according to Table 2-2 in §2.2.1.

5.3 Results

First attempts were aimed at trying to recover α and $d_{p,g}$ by assuming $P(d_p)$ obeys a lognormal distribution with σ_g = 1.5, following [34], and allowing T_i to vary, minimizing

$$F\left(\alpha, d_{p,g}, T_i\right) = \sum_{j=1}^{n}\left[T_{eff,j}^{exp} - T_{eff,j}^{mod}\left(\alpha, d_{p,g}, T_i\right)\right]^2 \qquad 5.10$$

following Kock et al. [8]. In contrast to this study, however, we were unable to find a unique solution for $d_{p,g}$ and α. Figure 5-4 shows a contour plot of the sum-of-squares function, Eq. 5.10, (T_i is set to its most probable value for each point) revealing a locus of solutions that all minimize the objective function. Examining the differential equation governing the particle cooling curves from the nanoparticles, neglecting evaporation and radiation, reveals that α and $d_{p,g}$ always appear as a ratio,

$$\frac{dT_p}{dt} = -\frac{\alpha}{d_p}\left[\frac{3P_g c_g}{4\rho c T_g}\frac{\gamma+1}{\gamma-1}\right]\left(T_p - T_g\right) \qquad 5.11$$

As such, α and $d_{p,g}$ are not linearly independent and a unique solution cannot exist. The discrepancy between this outcome and that of Kock et al. [8], is likely due to the fact that iron nanoparticles are more prone to evaporation, introducing an additional term in Eq. 5.5 that is independent of α.

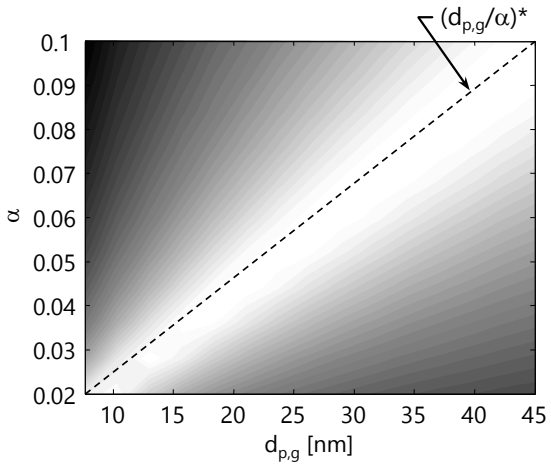

Figure 5-4: Contour plot of Eq. 5.10 minimizing $F(\alpha, d_{p,g}, T_i)$ for Mo-Ar, which shows no distinct minimum. (Contours are log-scale.)

Based on this observation, we next attempt to recover σ_g and the ratio $d_{p,g}/\alpha$ by minimizing

$$F\left(\sigma_g, d_{p,g}/\alpha, T_i\right) = \sum_{j=1}^{n}\left[T_{eff,j}^{exp} - T_{eff,j}^{mod}\left(\sigma_g, d_{p,g}/\alpha, T_i\right)\right]^2 \qquad 5.12$$

Figure 5-5 reveals a distinct local minimum corresponding to the most likely solution, $[\sigma_g, (d_{p,g}/\alpha)]^*$. The most probable solution is summarized in Table 5-1, and corresponding curves of modeled T_{eff} are shown in Figure 5-6, along with the experimental data. All the curves have the same general shape with an initially steep decay in T_{eff} with respect to time that gradually decreases in magnitude as the driving heat transfer potential, $T_p(t) - T_g$, becomes smaller. Studies on the gas phase production of nanoparticles from a precursor gas by Nunomura et al. [150] show that nanoparticle coalescence occurs over a duration of 2 s, while the LII measurement duration lasts 5.5 μs. Accordingly, it is safe to assume that the particle size distribution remains constant during the duration of measurement period. Regression of the carbon dioxide data resulted in

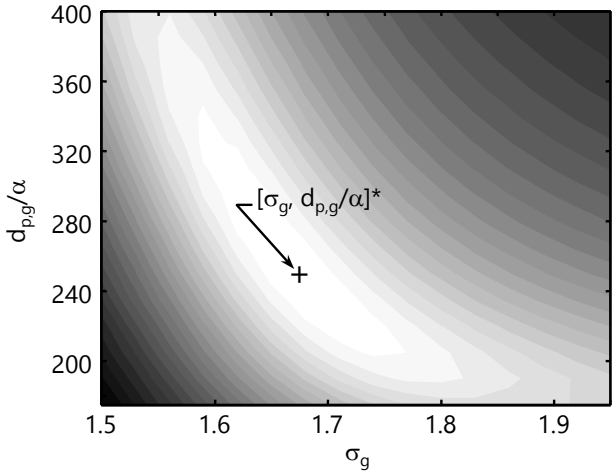

Figure 5-5: Contour plot of Eq. 5.12 minimizing $F(\sigma_g, d_{p,g}/\alpha, T_i)$ for Mo-Ar, which has a distinct minimum. (Contours are log-scale.)

Table 5-1: Size distribution parameters recovered by minimizing Eq. 5.12. Error bounds correspond to 95% credible intervals found by the bootstrapping method summarized in §4.1.3.

	Ar	N_2	CO_2
σ_g	1.7 ±0.1	1.5 +0.1 -0.2	1.3 ±0.1
$d_{p,g}/\alpha$ [nm]	250 +100 -70	180 +110 -60	270 +120 -110

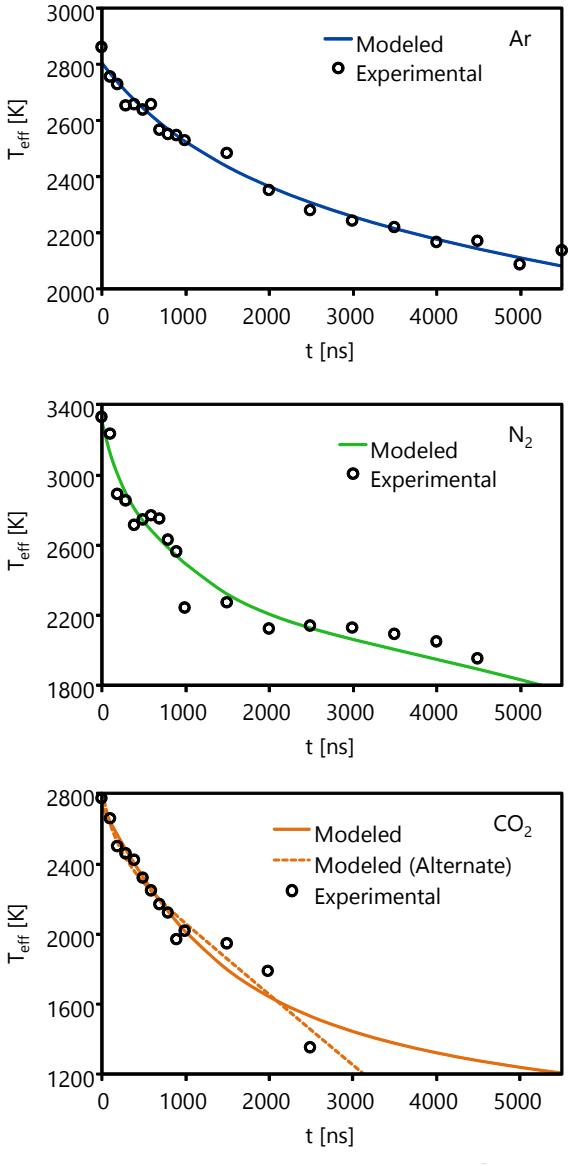

Figure 5-6: Experimentally-determined effective temperatures and the best-fit modeled cooling rates found using the parameters in Table 5-1.

two distinct minima, corresponding to the dashed line and the solid line which differ in their inflection at later points in time. The solid line is more consistent with the expected trends.

Inspection of Eq. 5.5 and Eq. 5.9 reveals that the temperatures of individual particles decays approximately exponentially and, neglecting the temperature-dependence of c_p and ρ,

$$\ln\left(T_p - T_g\right) \propto \frac{\alpha}{d_p} t \qquad 5.13$$

Therefore, if the nanoparticles all had the same size we would thus expect $\ln[T_{eff}(t) - T_g]$ to decay linearly with time. Plotting the effective temperatures obtained from the LII measurements made on molybdenum nanoparticles formed argon, shown in Figure 5-7, reveals that this curve is approximately linear at short timescales, but becomes less steep with increasing cooling time. Plots for the other gases show similar features. This phenomenon has also been observed in TiRe-LII studies on soot [151]. If the particle sizes obey a lognormal distribution, it can be shown that the observed effective temperature decay will initially be exponential; matching that expected from a hypothetical aerosol with uniform particle sizes equal to the Sauter mean diameter, $d_{p,32}$, defined in Eq. 4.3. At longer times, however, the effective temperature decay becomes non-exponential due to the delayed cooling and enhanced emission efficiency of larger particles in the "tail" of $P(d_p)$. Figure 5-7 also shows the best fit assuming uniform particle sizes, highlighting that the particle size distribution is certainly polydisperse.

5.3.1 Aleatoric Uncertainty

The error bounds accompanying the results in Table 1 are 95% credible intervals found using wild bootstrapping which is well-suited for determining the confidence interval for regression with a small sample size [143]. In addition to bootstrapping summarized in §4.1.3, in wild bootstrapping the residuals are resampled from the original set of residuals and multiplied by an

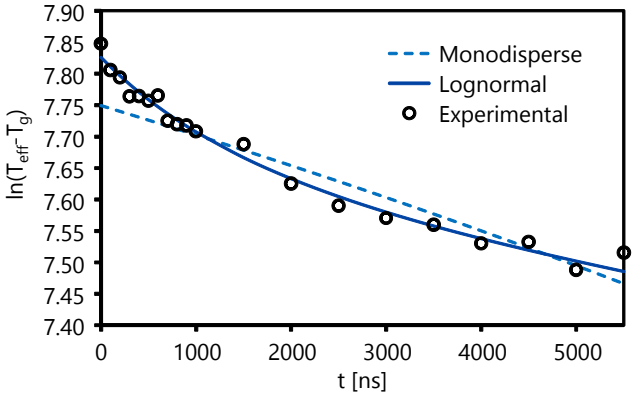

Figure 5-7: Plot of $\ln[T^{eff}(t) - T_g]$ versus cooling time for Mo-Ar, highlighting the influence of particle size dispersity on the data. A lognormal distribution results in a comparably better result than a monodisperse distribution of particles.

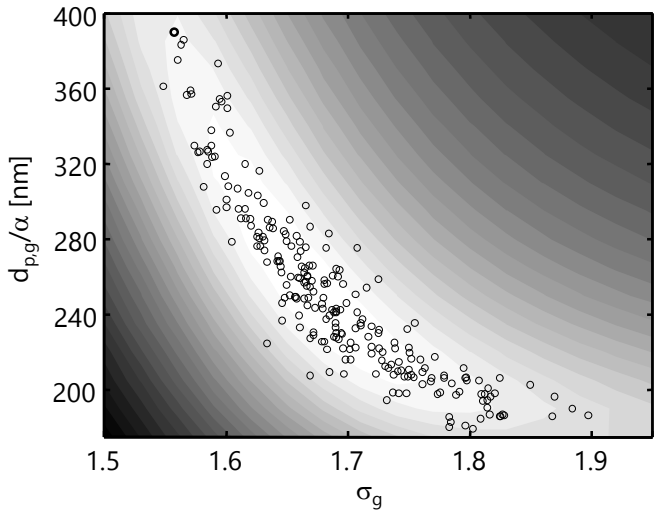

Figure 5-8: Contour plot of Eq. 5.12 minimizing $F(\sigma_g, d_{p,g}/\alpha, T_i)$ for Mo-Ar overlaid with samples from a wild bootstrapping analysis. (Contours are log-scale.)

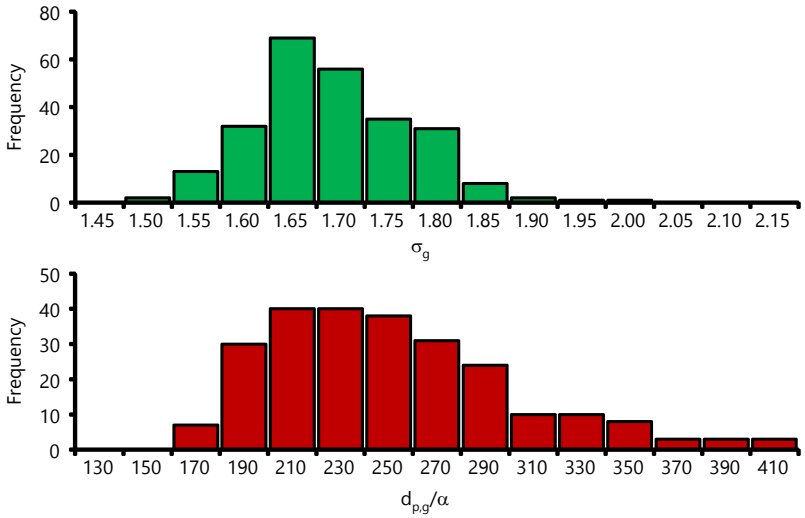

Figure 5-9: Histogram showing the result of 250 bootstrap samples for Mo-Ar yielding from which one can derive an average and an error bound.

additional factor randomly selected from a normal distribution with a mean of zero and a variance of one. Possible heteroscedasticity in the data was accounted for by studentizing [152] and rescaling the residuals with their standard deviation. The results of the repeated regressions using the perturbed data for argon are plotted over the contours of Eq. 5.12, in Figure 5-8. The histograms in Figure 5-9 illustrate the same data but explicitly show the range of results for each

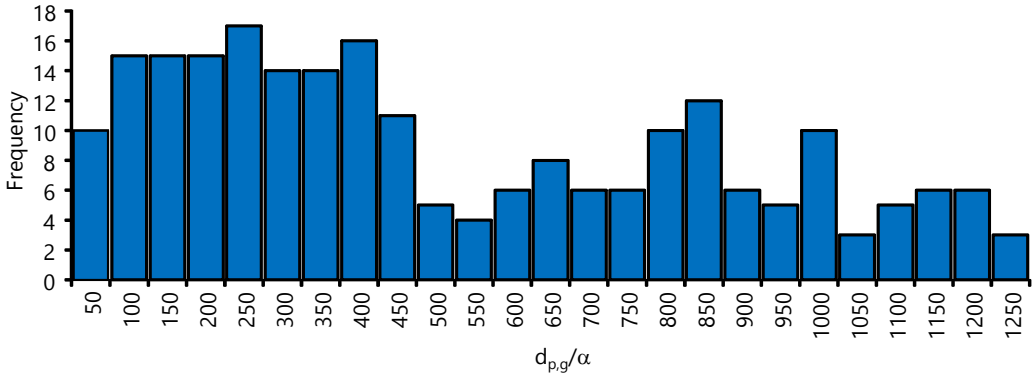

Figure 5-10: Histogram showing the results of the wild bootstrapping analysis on Mo-He data with a great deal of spread. In consequence, this data set was deemed as unusable.

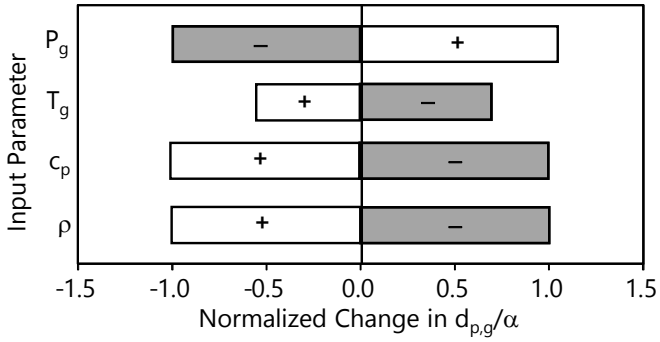

Figure 5-11: Sensitivity of $d_{p,g}/\alpha$ to selected input properties.

variable with a defined peak. The error bars are defined using the average and standard deviation of these values.

The sum-of-squares function for LII measurements made on nanoparticles formed in helium did not give a reliable result. Figure 5-10 shows the wide spread of results when the original data is perturbed using the wild bootstrap method. We speculate that this is due to the comparatively high scatter seen in the effective temperatures and comparatively high noise levels observed in the raw spectral incandescence data. This, in turn, may be evidence that the volume fraction of molybdenum nanoparticles is much smaller (due to smaller and/or fewer nanoparticles) compared to nanoparticles formed in Ar, N2, and CO2. This result is consistent with the hypothesis that the bigger gas molecules have an important catalytic role in gas synthesis [153]. The bath gas molecules are thought to collide with nascent clusters of molybdenum atoms and absorb some of the cluster's energy, preventing fragmentation of the cluster. Larger, more

Table 5-2: Comparison of $d_{p,g}$ for Mo-Ar with published values for Fe-Ar, using TACs for Fe-Ar

Study	α	$d_{p,g}$ (Referenced Study)	$d_{p,g}$ (Present Study)
Kock et al.	0.13	30	33
Starke et al.	0.33	15	83
Eremin et al.	0.1	11	25

complex gas molecules are able to absorb more energy from the cluster, resulting in larger nanoparticle growth rates.

5.3.2 Epistemic Uncertainty

A sensitivity analysis was also performed to determine the epistemic uncertainty due to p_g, T_g, c_p, and ρ, summarized in Figure 5-11. In many ways, this sensitivity analysis is analogous to that performed by Eremin et al. [36]. It differs, however, in that the percentage change in the inferred value, $d_{p,g}/\alpha$ in this case, is normalized by the percentage change in the input parameters. It is found that other than T_g, to which $d_{p,g}/\alpha$ is less sensitive than the other parameters, a one percent change in a property will result in approximately the same percent change in $d_{p,g}/\alpha$. This again is likely due to the direct or inverse proportionality seen in Eq. 5.11.

Uncertainties in the MD-derived TACs can further be addressed by considering TACs found experimentally for similar materials in TiRe-LII experiments. As previous mentioned, Fe-Ar is one of the most studied non-carbonaceous pairings in TiRe-LII experiments. Consider for a moment that Fe-Ar is close enough to Mo-Ar to use the experimentally-derived values as an estimate for α. Assuming α = 0.13, given by Kock et al. [33] for Fe-Ar, the present analysis yields $d_{p,g}$ = 33 nm. This value, representing a two order of magnitude decrease from the value originally published by Murakami et al. [45], lies in the same order to magnitude as $d_{p,g}$ = 26.9 nm found in the study by Kock et al. [33]. Similar logic can be applied to the studies for Fe-Ar by Starke et al. [32] and Eremin et al. [35] with similar results summarized in Table 5-2. The latter two studies derived their values using TEM images of the nanoparticles, a well-established technique that adds to the reliability of those values.

Chapter 6

TiRe-LII Analysis of Silicon Nanoparticles

Interest in the application of silicon nanoparticles at the University of Duisburg-Essen (UDE) in Germany has led to investigation of gas-borne silicon synthesis [154]. Consequently, researchers working with the Center for Nanointegration Duisburg-Essen (CENIDE) at UDE have reactors capable of synthesizing large quantities of silicon nanoparticles using microwave-induced electrical discharge of silane (SiH_4) in a low pressure flow plasma reactor [155]. Despite the usefulness of these particles, very few studies have examined how one can apply TiRe-LII in their characterization. This chapter summarizes one of the first efforts to size silicon nanoparticles using TiRe-LII in collaboration with researchers at CENIDE.

6.1 Experimental Procedure

Gas-borne non-agglomerated silicon nanoparticles are produced from silane (SiH_4) in a low-pressure microwave plasma flow reactor shown schematically in Figure 6-1. The chamber is first evacuated and then purged with argon to remove potential contaminants (e.g., O_2) that could react with the nanoparticles. Silane is premixed with dilution gases H_2 and Ar at a pressure of 12 kPa so that the volume ratio of the constituents is approximately 1:12:60 for SiH_4, H_2, and Ar respectively. The core flow of 3.7 L/min is surrounded by a Ar/H_2 coflow that stabilizes the plasma. The microwave radiation of a 1200 W magnetron is focused in the center of a 7.7 cm diameter quartz tube, producing a visible purple plasma in the lower region of the reactor shown in Figure 6-2. Due to unipolar particle charging, plasma reactors form non-aggregated, electrostatically confined nanoparticles with a narrow nanoparticle size distribution; the microwave plasma reactor used here is known to produce single crystalline silicon nanoparticles with a geometric standard deviation of approximately σ_g = 1.2 and nanoparticle sizes in the 5-50 nm range, depending on pressure and precursor concentration [156].

Time-resolved laser-induced incandescence measurements are carried out 20 cm downstream of the plasma zone using an Artium 200M TiRe-LII system shown in Figure 6-2. The instrument consists of a transmitter module containing a 1064 nm Nd:YAG laser and optics, a receiver module containing collection optics and two photomultiplier tubes, and a computer for

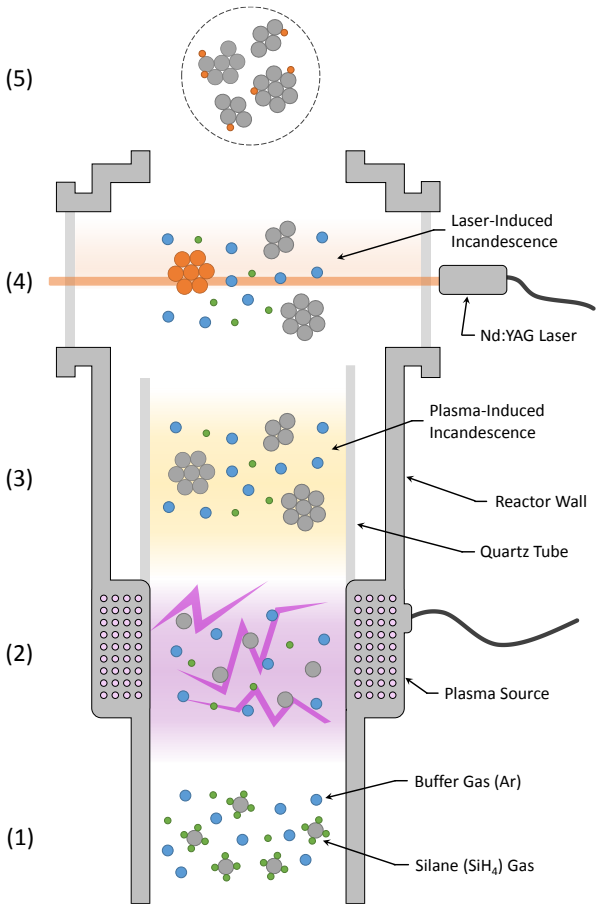

Figure 6-1: Experimental setup shown schematically including (1) the inlet gas, (2) the plasma region of the reactor, (3) silicon atoms collecting into glowing silicon nanoparticles, (4) TiRe-LII analysis on the nanoparticles, and (5) ex-situ BET analysis.

instrument control and data acquisition. Optical access to the aerosol is obtained through three quartz windows in the reactor walls. Inert gas flushing prevents particle deposition on the windows and allows continuous operation of the reactor for several hours. A laser pulse is shone across the reactor chamber through two opposite windows. The laser was operated with a repetition rate of 10 Hz. A nearly uniform "top-hat" beam profile with a square 2.8 mm × 2.8 mm cross section was generated by relay-imaging an aperture into the measurement location where fluences were in the 0.12–0.16 J/cm^2 range. The resulting incandescence signal of the laser-heated nanoparticles is detected through the third quartz window, perpendicular to the laser pulse; the probe volume is defined by intersection of the laser beam and the detector solid angle. The incandescence signal is split by a dichroic mirror, passed through two band-pass filters

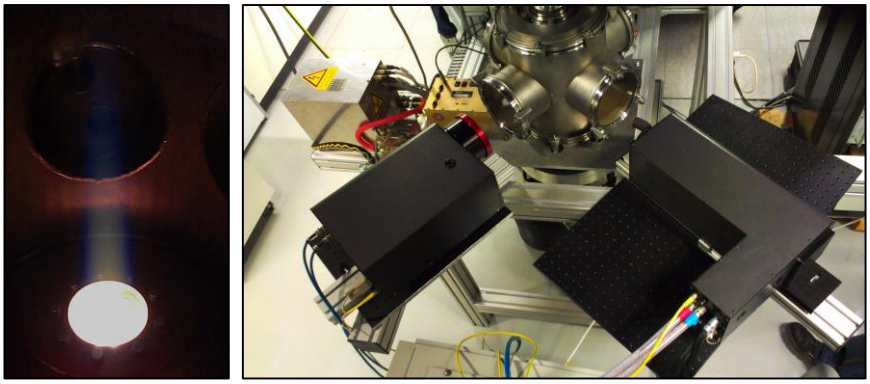

Figure 6-2: Left, a heated stream of particles leaving the glowing plasma region lower in the reactor. Right, Artium 200M LII system, including the transmitter and detector, aimed at viewing windows in the reactor.

centered at 442 and 716 nm (full width at half maximum of 50 nm), and imaged onto the photomultiplier tubes. Further details of this procedure are provided in Ref. [157].

The in situ size measurements of the silicon nanoparticles by TiRe-LII are complemented with the measurement of an average nanoparticle size calculated from their specific surface as measured by nitrogen adsorption (Brunauer-Emmett-Teller, BET, Quantachrome Nova 2200) of silicon powder collected via a filter behind the reactor [158]. BET infers the specific surface area of nanoparticles from the physisorption of N_2 by a sample of nanoparticle powder, which was kept at 150°C and under vacuum over night to remove residual water. Assuming that the nanoparticles are monodisperese spheres, these measurements can be converted to a representative nanoparticle diameter based on the knowledge of the sample mass and density. This technique is commonly used to determine the size of non-aggregated nanoparticles and has also been applied to size silicon nanoparticles produced from the reactor in previous studies [154]. Typical measurements from the CENIDE lab showed a repeatability with <1% variation in particle size. A previous study compared the results of BET measurements across several labs with variation below 5% [159].

6.1.1 Interpretation of Spectral Data and Effective Temperature

The spectral incandescence from the laser-heated nanoparticles can be modeled by integrating the incandescence emitted by all nanoparticle sizes, given by Eq. 2.1

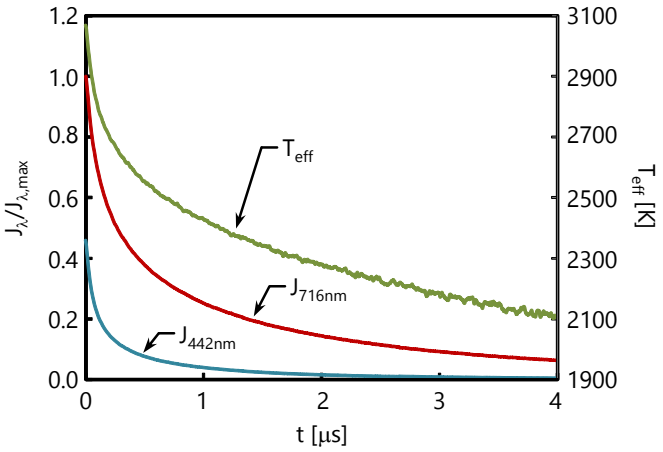

Figure 6-3: TiRe-LII experimental data: scaled monochromatic incandescence and pyrometrically-defined effective temperature.

$$J_\lambda(t) = C\int_0^\infty \frac{\pi d_p^2}{4} P(d_p) Q_{abs,\lambda}(d_p) I_{b,\lambda}\left[T_p(t,d_p)\right] d(d_p) \tag{6.1}$$

The spectral incandescence data at the two wavelengths is used to derive a pyrometrically-defined effective temperature given by Eq. 2.7

$$T_{eff}(t_i) = \frac{hc_o}{k_B}\left(\frac{1}{\lambda_2}-\frac{1}{\lambda_1}\right)\frac{1}{\ln\left\{K_{opt}\left(\frac{J_{\lambda_1}(t_i)}{J_{\lambda_2}(t_i)}\right)\left(\frac{E_{m_{\lambda_2}}}{E_{m_{\lambda_1}}}\right)\left(\frac{\lambda_1}{\lambda_2}\right)^6\right\}} \tag{6.2}$$

where K_{opt} contains the spectral transmissivity of the quartz window. Window transmissivity was determined using a deuterium lamp over ultraviolet wavelengths and a xenon lamp over visible wavelengths, and was found to be 0.89 and 0.9 for wavelengths of 442 nm and 716 nm, respectively. A sample incandescence trace (averaged over 300 shots) and its corresponding effective temperature are shown in Figure 6-3.

6.2 Material Properties

6.2.1 Optical Constants

The optical constants, used to find the complex absorption function, $E(\mathbf{m}_\lambda)$, are taken from Fuchs [52] for silicon in the liquid phase. These values were derived from theoretical work that estimated the optical constants from density function theory. As validation, Fuchs compared the theoretical work to several other sources for the optical constants, including Jellison and Lowndes [55], Shvarev et al. (T = 1450 K and T = 1600 K, not liquid) [160], and Li and Fauchet [161,162], with reasonable consistency across all of the sources. Figure 6-5 shows Fuchs [52] and Jellison and Lowndes [55] plotted with the room temperature complex absorption function of silicon from Palik [51]. The plot shows that there is an appreciable difference between the room temperature values and two of the sources for liquid, highlighting the importance of the optical properties in this analysis.

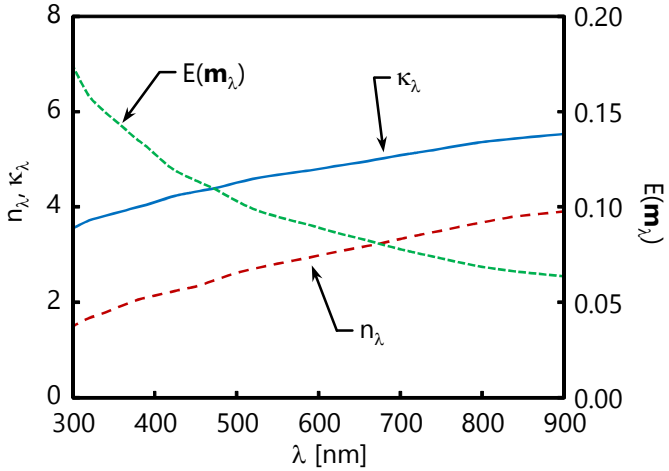

Figure 6-4: Indices of refraction and the absorption function for silicon taken from Fuchs [45].

6.2.2 Sensible Heat Properties

The bulk density is taken from Rhim and Ohsaka [128]

$$\rho(T) = 2.58 - 1.59(T - T_m) - 1.15(T - T_m)^2 \qquad 6.3$$

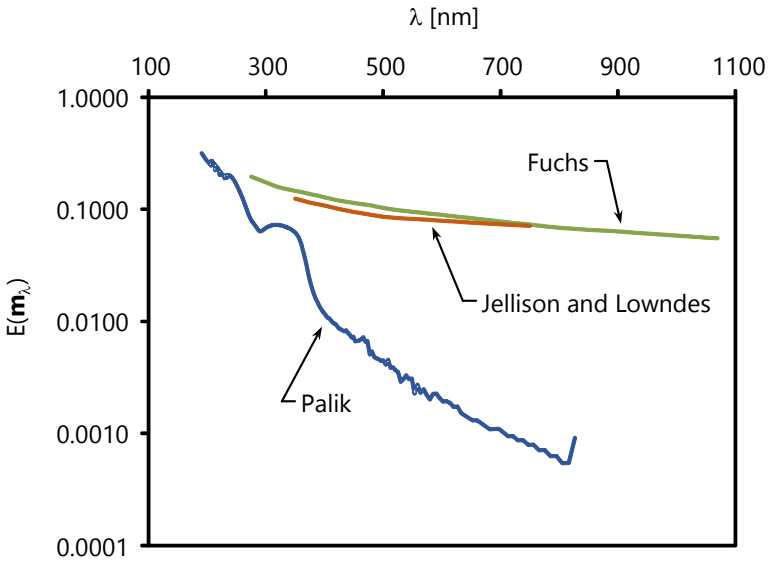

Figure 6-5: The complex absorption function, *E*(m$_\lambda$), of liquid silicon from Fuchs [45] and Jellison and Lowndes [48] and room temperature silicon from Palik [44]. Note that *E*(m$_\lambda$) is plotted on a logarithmic scale.

which is shown to be in good agreement with experimentally derived values in the range 1350 K < T < 1850 K. The bulk specific heat is taken from Desai [163]

$$c_p\left(T > T_m\right) = \frac{27.2}{M} \tag{6.4}$$

where M is the molar mass of silicon.

6.2.3 Conduction Properties

Conduction from the nanoparticles is based Eq. 2.19

$$q_{cond}\left(t, d_p\right) = \alpha\pi d_p^2\left(\frac{p_g c_{g,t}}{4T_g}\right)\left(2 + \frac{\zeta_{rot}}{2}\right)\left(T_p - T_g\right) \tag{6.5}$$

Modifications to this equation are required as a consequence of the gas being a mixture of H_2 and Ar. As conduction occurs in the free molecular regime, it is assumed that the H_2 and Ar molecules do not interact either shortly before or shortly after they collide with the particle surface. As a result, the gases can be treated independently with the total conduction being the superposition of the conduction from each gas with the conduction from argon given by

$$q_{cond,Ar}\left(t,d_p\right)=\alpha_{Ar}\pi d_p^2\left(\frac{p_{g,Ar}}{4T_g}\right)\left(2+\frac{\zeta_{rot,Ar}}{2}\right)\sqrt{\frac{8k_BT_g}{\pi m_{g,Ar}}}\left(T_p-T_g\right) \quad 6.6$$

And the conduction from hydrogen is given by

$$q_{cond,H_2}\left(t,d_p\right)=\alpha_{H_2}\pi d_p^2\left(\frac{3p_{g,H_2}}{4T_g}\right)\left(2+\frac{\zeta_{rot,H_2}}{2}\right)\sqrt{\frac{8k_BT_g}{\pi m_{g,H_2}}}\left(T_p-T_g\right) \quad 6.7$$

where $p_{g,i}$ is the partial pressure of the i^{th} gas. Accounting for free-molecular heat conduction by the H_2 molecules requires knowledge of the α_{H2}, which was not quantified using MD due to the complexity of deriving *ab initio* potentials for a polyatomic molecule. Since previous work has shown that the mass ratio and the TAC are closely related [75], H_2 was modeled as monatomic and α_{H2} was assigned the value of α_{He} due to the similar mass of the two gases. Uncertainty introduced by this assumption is addressed in §6.3.2. Considering the sum of these terms and that both gases will be treated as monatomic gases, the total conduction becomes

$$q_{cond}\left(t,d_p\right)=\left(\frac{\alpha_{Ar}p_{g,Ar}}{2\sqrt{m_{g,Ar}}}+\frac{\alpha_{H_2}p_{g,H_2}}{2\sqrt{m_{g,H_2}}}\right)d_p^2\sqrt{\frac{8k_B\pi}{T_g}}\left(T_p-T_g\right) \quad 6.8$$

It is useful to define Eq. 6.8 in terms of weights of the i^{th} gas, $w_{cond,i}$, such that

$$w_{cond,i}=\frac{\alpha_i p_{g,i}}{4\sqrt{m_{g,i}}}\left(2+\frac{\zeta_{rot,i}}{2}\right) \quad 6.9$$

This allows for a simple comparison of the significance of each gas by comparing their weights. In this case, the TAC is given by the MD simulations in §3.4, with α_{Ar} = 0.35 and α_{H2} = α_{He} = 0.11, based on estimates at T_p = 2500 K and T_g = 1000 K. Using these values and the partial pressures stated above for this experiment, Eq. 6.9 can be evaluated to give the ratio of the weights for each gas, $w_{cond,Ar}/w_{cond,H2}$ = 3.66. This suggests that the conduction is dominated by argon and, in consequence, uncertainties resulting from conduction due to hydrogen will not be as prevalent.

To affirm the gas temperature, a thermocouple was inserted in the central gas flow slightly above the TiRe-LII probe volume. After correcting for radiation losses from the probe, it indicated T_g = 1300 K, which is consistent with temperatures found through planar laser-induced florescence measurements carried out in a similar reactor [164]. Uncertainty in this value is also addressed in §6.3.2.

6.2.4 Evaporation Properties

Evaporation from the nanoparticles is given by Eq. 2.22

$$\dot{q}_{evap} = \left(\frac{p_v c_{v,t}}{4 k_B T_p} \right) \pi d_p^2 \Delta h_v \beta \tag{6.10}$$

For the purposes of this work, β is assumed to be unity. The heat of vaporization, Δh_v, is given by the aforementioned Watson's equation [67,68]

$$\Delta h_v = K \left(1 - T_r\right)^{0.38} \tag{6.11}$$

The critical temperature, used in the reduced temperature, T_r, is 5193 K taken from [165]. The material constant, K, is solved based on the heat of vaporization at atmospheric pressure, such that

$$K = \frac{\Delta h_{v,b}}{\left(1 - T_b / T_{cr}\right)^{0.38}} \tag{6.12}$$

where $h_{v,b}$ = 359 kJ/mol and T_b = 3538 K are taken from [166]. The vapor pressure is then defined based on the Clausius-Claperon equation [36], previous defined in Eq. 2.23 as

$$\ln\left(p_v\right) = -\frac{\Delta h_v}{R} \frac{1}{T_p} + C \tag{6.13}$$

6.3 Results

Silicon nanoparticle diameters are initially found by nonlinear regression of the experimental pyrometrically-defined effective temperature, T_{eff}, to the same effective temperature derived from a simulated incandescence signal found by solving Eq. 6.1. Since the procedure for inferring the nanoparticle size distribution from TiRe-LII data requires an initial condition of uniform nanoparticle temperatures (taken to be the peak temperature in the case of a "top-hat" beam profile) and because of a smoothing effect lasting several nanoseconds around the peak temperature, it is necessary to extrapolate a hypothetical peak nanoparticle temperature that would be compatible with the conduction and evaporation cooling models. Accordingly, instead of the experimentally-observed peak temperature of 3075 K, a somewhat higher initial

temperature, Ti = 3100 K, was chosen as an initial condition to account for the smoothing effect at the peak.

Based on detailed TEM studies of nanoparticles extracted from the same reactor (e.g. [159]) the nanoparticle sizes are known to follow the aforementioned lognormal distribution

$$P(x) = \frac{1}{x\sqrt{2\pi}\ln\sigma_g}\exp\left[\frac{-\left(\ln x - \ln d_{p,g}\right)^2}{2\left(\ln\sigma_g\right)^2}\right] \qquad 6.14$$

defined by the geometric standard deviation, σ_g, and geometric mean particle diameter, $d_{p,g}$, which is also the median diameter for a lognormal distribution. Figure 6-6 compares the modelled data corresponding to the maximum a posteriori (MAPs) of the lognormal distribution parameters, $d_{p,g}$ = 24.2 nm and σ_g = 1.43, reported in Table 6-1. On the other hand, if the aerosol were monodisperse, the MLE nanoparticle diameter is 37.3 nm. Note, however, that the monodisperse model is unable to predict the incandescence decay at measurement times greater than 2 μs, which one would expect as the influence of polydisperse nanoparticle sizes on the incandescence decay becomes more pronounced at longer cooling times [74]. The maximum a posteriori (MAP) estimate of σ_g = 1.43 is well aligned with the σ_g = 1.50, typical of a self-preserving distribution for an aerosol in which nanoparticle growth mechanisms have stabilized [145]. On the other hand, this value is larger than the σ_g = 1.2 typically found from in situ particle mass spectrometry and *ex situ* TEM analysis [155]; the narrower distribution is also what one would expect based on the Coulomb repulsion of the charged nanoparticles [156].

6.3.1 Aleatoric Uncertainty

Uncertainty in the distribution parameters caused by noise in the monochromatic incandescence measurements (due mainly to photomultiplier shot noise) was quantified using robust Bayesian analysis summarized in §4.1.3, where the posterior probability, $P(\mathbf{x}|\mathbf{b})$, of the hypothesized set of distribution parameters in $\mathbf{x} = [d_{p,g}, \sigma_g]^T$ is defined by

$$P(\mathbf{x}|\mathbf{b}) = \frac{P(\mathbf{b}|\mathbf{x})P_{pr}(\mathbf{x})}{P(\mathbf{b})} \qquad 6.15$$

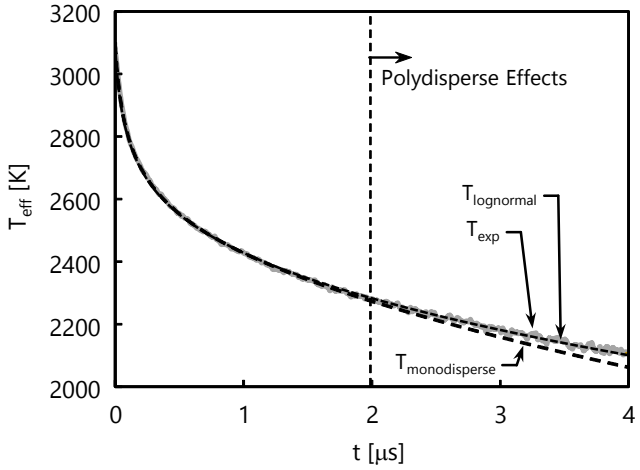

Figure 6-6: Experimentally observed pyrometric temperatures (solid line), and modeled temperature decays corresponding to the most probable monodisperse (long dash) and lognormal (short dash) nanoparticle size distributions. The monodisperse assumption is incapable of reproducing the observed pyrometric temperatures at longer cooling times due to the polydispersity of nanoparticle sizes.

Table 6-1: Most probable nanoparticle size distribution parameters and credible intervals.

	Mean	Aleatoric Uncertainty
$d_{p,g}$ [nm]	24.2	(22.8, 25.7)
σ_g	1.43	(1.39, 1.46)
$d_{p,32}$ [nm]	33.2	(32.6, 33.8)

Assuming the spectral incandescence data is contaminated with independent, normally-distributed error, the likelihood is given by

$$P(\mathbf{b}\,|\,\mathbf{x}) = \prod_j \frac{1}{\sqrt{2\pi\sigma_j^2}} \exp\left\{ -\frac{\left(T_{\exp,j} - T_{\mathrm{mod},j}\right)^2}{2\sigma_j^2} \right\} \qquad 6.16$$

where σ_j is the expected standard deviation of the measured incandescence at the j^{th} measurement time. The standard deviation increases at longer cooling times, as the signal-to-noise ratio in the incandescence traces drops with decreasing signal intensity [137]. In order to account for this fact, σ_j is modeled by a quadratic function fitted to the standard deviations of the mean of 300 independent sets of incandescence data evaluated at every measurement time. The

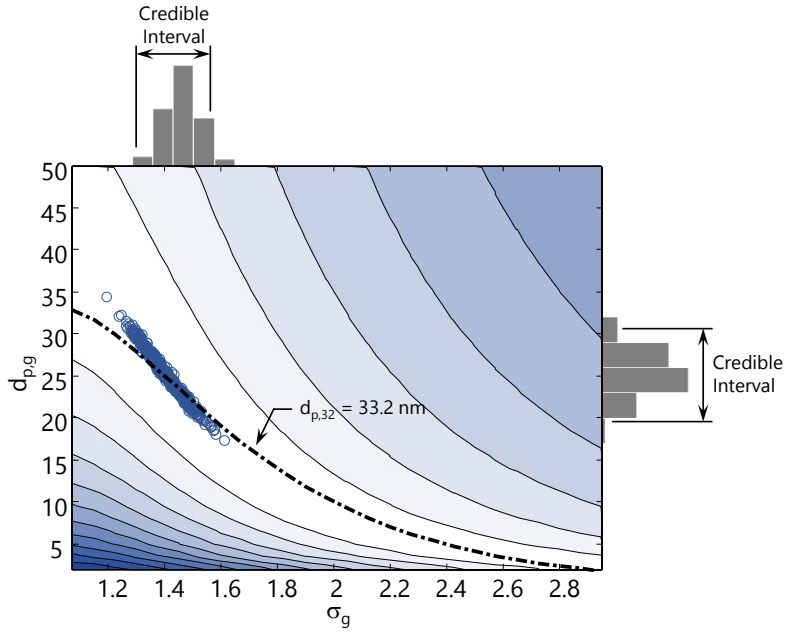

Figure 6-7: MCMC samples laid over contours of the logarithmic posterior distribution. Histograms show the posterior distribution resulting from MCMC sampling, while the solid line corresponds to lognormal nanoparticle sizes that share a Sauter mean of $d_{p,32}$ = 33.2 nm.

prior probability is defined analogous to Eq. 4.7, only considering the lognormal distribution parameters, such that

$$P_{pr}\left(\mathbf{x}\right)=\begin{cases}1 & \text{if } d_{p,g}\geq 0 \text{ and } \sigma_g \geq 1\\ 0 & \text{else}\end{cases} \qquad 6.17$$

While Eq. 6.17 defines a two-dimensional space of the probability density of $\mathbf{x}$, it is more convenient to quantify the uncertainty of a distribution parameter of interest with a credible interval over the marginalized probability densities of each variable. A set of 10,000 samples, $\mathbf{X} = \{\mathbf{x}_1, \mathbf{x}_2, \ldots \mathbf{x}_n\}$, generated using a Markov Chain Monte Carlo (MCMC) algorithm [167] following §4.1.3, are used to form marginalized posterior distributions for $d_{p,g}$ and σ_g through kernel density estimation [168]. The 95% credible intervals resulting from this procedure are given in Table 6-1. The MCMC samples are plotted over contours of the residual norm in Figure 6-7, showing the relationship between the samples and the region of minimal residual.

The large credible intervals associated with $d_{p,g}$ and σ_g are typical of ill-posed inverse problems, since a wide range of nanoparticle size distributions exist that explain the experimental data within the standard deviation due to signal noise. Figure 6-7 shows that these solutions lie along a specified thin region of minimal residual. Daun et al. [48] demonstrated that this family of solutions approximately shares a narrow distribution of Sauter mean diameters, defined for a lognormal distribution in Eq. 4.3 as

$$d_{p,32} = d_{p,g} \exp\left[5/2 \ln\left(\sigma_g\right)^2 \right] \tag{6.18}$$

Credible intervals for $d_{p,32}$ are also reported in Table 6-1. As one would expect, the credible interval is considerably smaller than that found for $d_{p,g}$ since the ill-posedness of the problem is due to the narrow curvature of the residual function along the locus of distributions that share a common Sauter mean diameter.

Ex situ measurements made by BET analysis on a nanoparticle powder consisting of spherical, non-aggregated particles loosely connected by point contacts give an approximate diameter of 33.3nm. This diameter can also be interpreted as the Sauter mean diameter since the nanoparticle size is derived from the ensemble volume of nanoparticles (found from the mass of the sample and bulk density of Si), divided by the specific surface area, which is inferred from N_2 adsorption. This value is in excellent agreement with the TiRe-LII derived Sauter mean of 33.2 nm, and lies well within the aleatoric uncertainty.

6.3.2 Epistemic Uncertainty

We must also consider, separately, how model parameter uncertainty affects the recovered nanoparticle size distribution parameters. As noted above, the gas temperature within the probe volume is difficult to measure precisely due to the limited access afforded by the reactor geometry, but is approximately 1300 K based on a thermocouple measurement in near the probe volume. An uncertainty of ±200 K is assigned as a conservative estimate of this uncertainty, primarily due to uncertainty in laser position with respect to the thermocouple location. The extrapolated initial nanoparticle temperature used in the sizing analysis is assigned an uncertainty of ±25 K, based on the difference between the experimentally-observed peak temperature (3075 K) and the assumed value (3100 K). The TAC for H_2 is assigned a conservative

uncertainty of ±50%. Uncertainties in ρ, c_p, p_g, γ_s, T_{cr}, and the MD-derived α_{Ar} are taken to be 10% of their nominal values.

The impact of these uncertainties on the inferred size parameters is assessed through a perturbation analysis, in which the local sensitivities (for example $[\partial d_{p,g}/\partial T_i]|T_i$) are estimated through a central finite difference approximation, following §4.2.1. Values reported in Table 6-2 are the relative sensitivity coefficients where the error can be found using Eq. 4.14

$$\varepsilon(x|\phi) = PE(\phi) \times RSC(\phi, x) = PE(\phi) \times \left[\phi \frac{\partial x}{\partial \phi} \right]_{\phi_0} \tag{6.19}$$

where ε is the error in the units of the inferred parameter, *PE* is the percentage error in a model parameter stated in the previous paragraph, and *RSC* is the relative sensitivity coefficient. These error bounds are comparable in magnitude to the credible intervals associated with aleatoric uncertainty.

Table 6-2: Relative sensitivity coefficients (eg. $T_i \cdot \partial d_{p,g}/\partial T_i$) and estimated error for inferred nanoparticle size distribution parameters due to model parameters.

	$d_{p,g}$ [nm]		σ_g		$d_{p,32}$ [nm]	
	RSC	**ε**	**RSC**	**ε**	**RSC**	**ε**
T_i	-148.0	±1.2	3.90	±0.03	-75.0	∓0.6
T_g	73.4	±11.3	-2.38	∓0.37	8.7	±1.3
p_g	-33.8	∓3.4	1.10	±0.11	-1.7	∓0.2
c_p	-21.7	∓2.2	-0.05	-	-31.9	∓3.2
ρ	-24.3	∓2.4	-	-	-33.4	∓2.4
α_{Ar}	-21.8	∓2.2	0.70	±0.07	-1.1	∓0.1
α_{H2}	-11.7	∓5.9	0.37	±0.19	-0.6	∓0.3
γ_s	2.6	±0.3	-0.05	-	1.5	±0.2
T_{cr}	47.9	±4.8	-0.70	∓0.07	38.7	±3.9

Chapter 7

TiRe-LII Analysis of Iron Nanoparticles

Iron is one of the most studied non-carbonaceous nanoparticles in TiRe-LII. However, despite thorough study, the TAC remains uncertain in most analyses. The present experiment works particularly on quantifying the TAC for a number of gas-surface pairs of interest in the TiRe-LII community. Most TiRe-LII experiments do not have *a priori* knowledge of the particle size distribution as it is dependent on some synthesizing process. The present experiments are aimed at isolating the heat transfer mechanisms by decoupling the synthesizing process from the TiRe-LII experiments. This chapter discusses the finding of the preliminary set of experiments using this technique.

7.1 Experimental Procedure

Zero-valent iron monomers were synthesized by reducing ferrous iron (Fe^{2+}) with a solution of sodium borohydride ($NaBH_4$), using the procedure described in Liu et al. [169,170]. For a final volume of 100 mL, a 1:2.4 volume ratio of iron (II) sulfate heptahydrate ($FeSO_4 \cdot 7H_2O$) solution at a concentration 1.28 mol/L, carboxymethylcellulose (CMC) (~250 kDa) solution (to a final concentration of 0.85 wt. %), and ultrapure de-ionized water, respectively, are added to a flask. This dilution ensures that each atomized droplet, estimates at 0.3 μm in diameter, contains, on average, one iron monomer. Adding the CMC stabilizer to the iron salt solution under vigorous agitation for approximately 20 minutes ensures formation of the CMC-Fe^{2+} complex, effectively capping the iron monomers such that they don't agglomerate. Following titration of 15 mL sodium borohydride solution, at a concentration of 4.26 mol/L, under continuous vigorous stirring, a black colloid suspension of CMC-stabilized zero valent iron monomers is obtained from

$$Fe^{2+} + 2BH_4^- + 6H_2O \rightarrow Fe^0 + 2B(OH)_3 + 7H_2 \qquad 7.1$$

The mean hydrodynamic diameter and the number-based size distribution of the iron monomers were determined by dynamic light scattering (DLS) using a Malvern Instruments Zetasizer Nano-ZS90 and a refractive index of 2.87 [171]. TEM samples of the iron monomers were obtained by placing drop of the diluted colloidal solution on a 200-mesh copper grid and left to dry in air

The colloid suspension is then aerosolized using a TSI Model 3076 pneumatic atomizer operating in recirculation mode. As shown in Figure 7-1, compressed gases (He, Ar, N_2, and CO_2) at 30 psig flow through an orifice into a low-pressure mixing chamber; the nanoparticle solution is drawn up a vertical channel into the mixing chamber, where it is atomized by the gas stream. The gas stream then impacts a wall; the larger droplets condense and flow back into the solution container, while the smallest droplets are carried into the diffusion dryer. The water droplets then flow through a diffusion dryer filled with a silica gel desiccant, which removes the water leaving the iron nanoparticles in the gas stream.

The dry aerosol then enters the measurement chamber of an Artium 200 M TiRe-LII system. A 1064 nm Nd:YAG laser pulse energizes the nanoparticles and two photomultiplier tubes measure the time-resolved incandescence at 442 nm and 716 nm. The complete experimental method is summarized schematically in Figure 7-1.

7.1.1 Interpretation of Spectral Incandescence and Effective Temperature

Incandescence signals were collected from 250 pulses for each aerosol type. Multishot averaging greatly reduces the amount of noise observed in the signal and provides variances used in the Bayesian analysis. The corresponding incandescence and temperature curves are shown in Figure 7-2, where the effective temperature is defined based on the definition for two-color pyromtry in Eq. 2.18

$$T_{eff}\left(t_i\right)=\frac{hc_o}{k_B}\left(\frac{1}{\lambda_2}-\frac{1}{\lambda_1}\right)\frac{1}{\ln\left\{K_{opt}\left(\frac{J_{\lambda_1}\left(t_i\right)}{J_{\lambda_2}\left(t_i\right)}\right)\left(\frac{E_{m_{\lambda_2}}}{E_{m_{\lambda_1}}}\right)\left(\frac{\lambda_1}{\lambda_2}\right)^6\right\}} \tag{7.2}$$

The optical constants for the experimental components, generally summarized in K_{opt}, were corrected for in the software used to collect the signals. As such, $K_{opt} = 1$ for the present analysis. Irregular cooling is observed at times shortly following the peak incandescence, that is, $t < 50$ ns. The origin of this phenomenon is unclear, but it may be due to non-incandescent laser-induced emission [172].

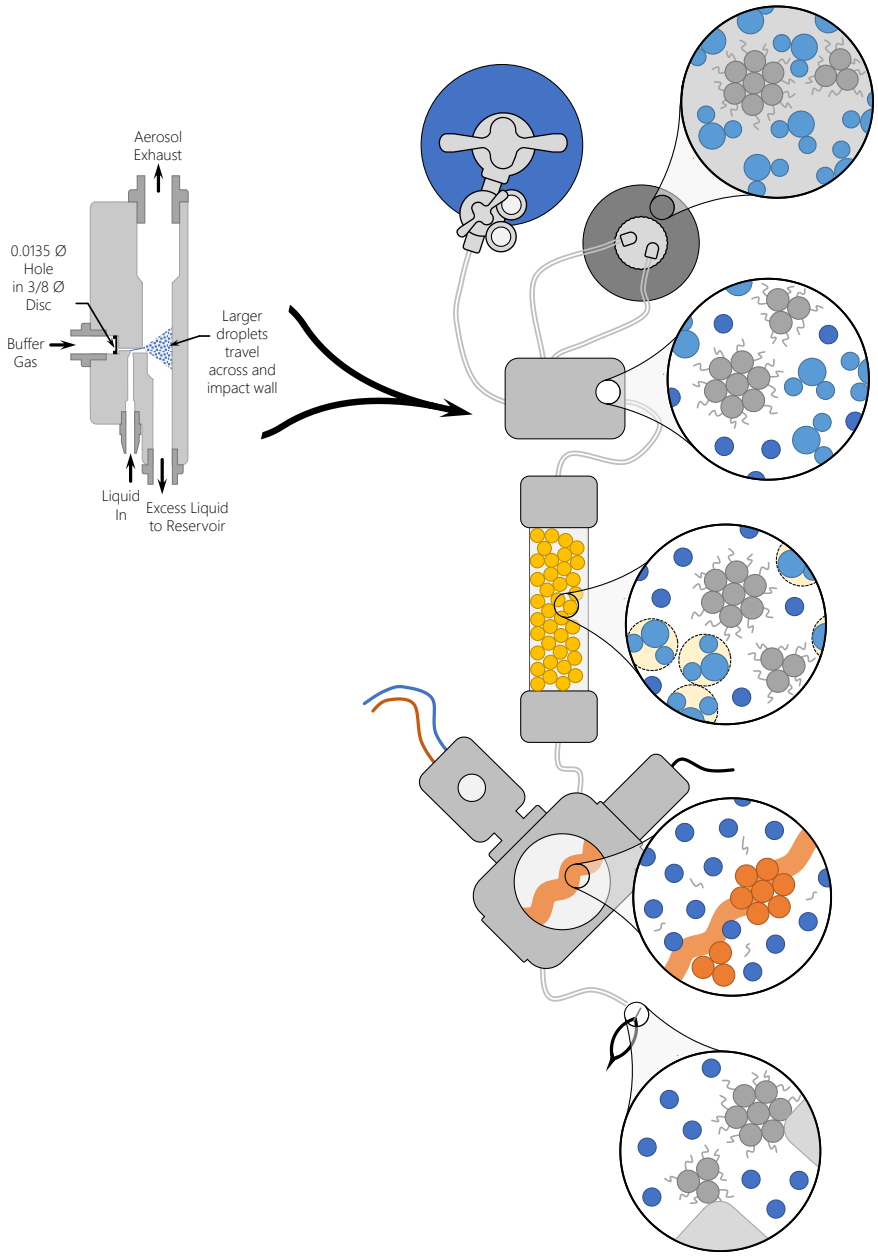

Figure 7-1: Experimental procedure: iron monomers contained in solution are induced into a TSI Model 3076 pneumatic atomizer by the motive gas and leave as 0.3 µm droplets. The droplets then pass through a diffusion dryer with a desiccant to remove water, leaving a dry aerosol of iron monomers. The monomers flow into the TiRe-LII measurement chamber and are then exhausted.

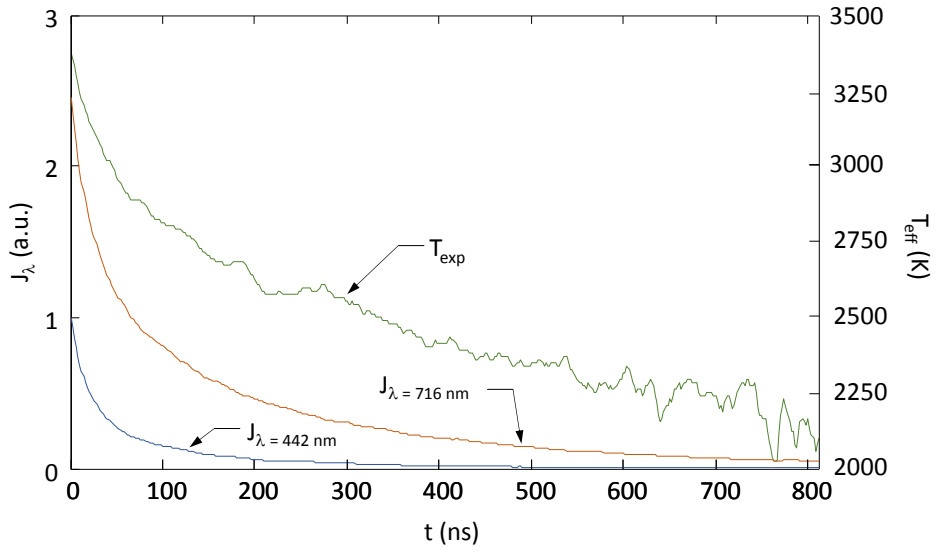

Figure 7-2: Multishot averaged incandescence and temperature decay used to infer parameters in the TiRe-LII experiments.

7.2 Material Properties

7.2.1 Optical Constants

The optical constants, used to find the complex absorption function, $E(\mathbf{m}_\lambda)$, are taken from Miller [56] who used ellipsometry measurements on a molten iron surface. Several other sources are available that report the optical constants of iron under various conditions. Krishnan et al. [57], for example, also quantified the optical constants for liquid iron using ellipsometry. Alternatively, the optical constants for solid iron are reported in Johnson and Christy [173] and Palik [51], among others. Figure 7-3 compares $E(\mathbf{m}_\lambda)$ from Miller, Krishnan et al., and Johnson and Christy. The optical properties show similar characteristics to molybdenum seen in §5.2.1, with $E(\mathbf{m}_\lambda)$ increasing towards a peak at lower wavelengths where the peak is shifted to lower temperatures for higher temperatures.

7.2.2 Sensible Heat Properties

The bulk density is taken from Hixson et al. [174] for liquid iron

$$\rho(T) = -0.64985T + 8171 \qquad 7.3$$

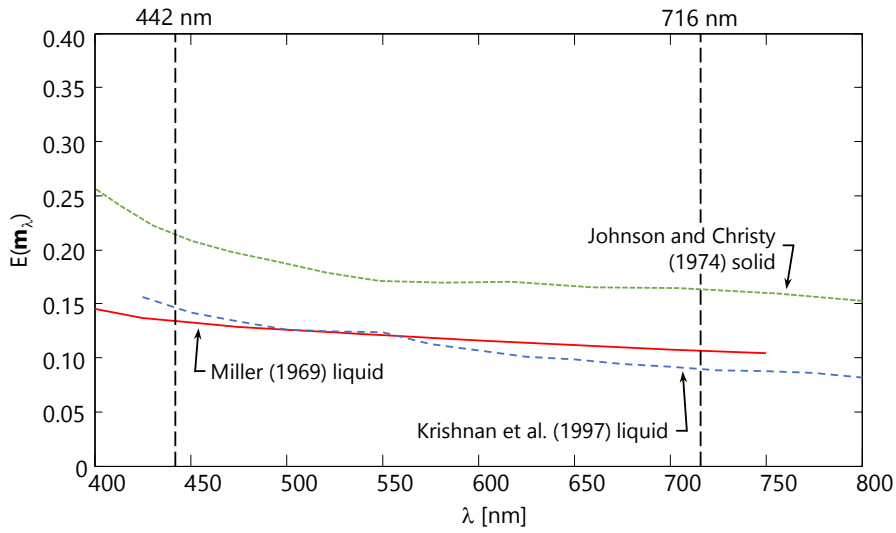

Figure 7-3: Absorption function of liquid iron from Miller [49] and Krishnan et al. [50] and solid iron from Johnson and Christy [173].

which is shown to be in good agreement with experimentally values in the range 2125 K < T < 3950 K. The values also showed good agreement with Drotning [175]. The bulk specific heat is taken from Desai [163]

$$c_p\left(T > T_m\right) = \frac{46.6}{M} \tag{7.4}$$

where M is the molar mass of iron.

7.2.3 Conduction Properties

Conduction from the nanoparticles is given by Eq. 2.19

$$q_{cond}\left(t, d_p\right) = \alpha\pi d_p^2 \left(\frac{p_g c_{g,t}}{4T_g}\right)\left(2 + \frac{\zeta_{rot}}{2}\right)\left(T_p - T_g\right) \tag{7.5}$$

with the value of ζ_{rot} defined as outlined in §2.2.1 and Table 2-2. Pressure gauge measurements immediately prior to the TiRe-LII measurement chamber affirm that the pressure inside the chamber is nearly atmospheric. This is expected as the system exhausts to atmosphere following the TiRe-LII measurement chamber. The TAC is not specified as it is a parameter of interest to be inferred in subsequent analysis.

7.2.4 Evaporation Properties

Evaporation from the nanoparticles is given by Eq. 2.22

$$\dot{q}_{evap} = \left(\frac{p_v c_{v,t}}{4 k_B T_p} \right) \pi d_p^2 \Delta h_v \beta \tag{7.6}$$

For the purposes of this work, β is assumed to be unity, analogous to the treatment of silicon in Chapter 6. The heat of vaporization, Δh_v, is again given by the Watson's equation [67,68]

$$\Delta h_v = K \left(1 - T_r\right)^{0.38} \tag{7.7}$$

with T_{cr} = 9340 K taken from Young and Alder [176] and K defined analogous to above with $h_{v,b}$ = 340 kJ/mol and T_b = 3134 K are taken from [166]. The vapor pressure is then defined by the Clausius-Claperon equation [36], again, analogous to above.

7.3 Results

The TAC and particle size were inferred simultaneously assuming a monodisperse nanoparticle size distribution. It was found that, unlike the silicon signals shown in Figure 6-6, these signals can be modeled solely using a single nanoparticle size, giving validity to this assumption. The results of this analysis are summarized in Table 7-1. Analysis of the TiRe-LII data collected on the various aerosols reveal nanoparticle sizes consistently smaller than those from similar DLS and TEM measurements made on a sample of nanofluid produced by the same technique. The discrepancy in the DLS can be attributed to the presence of the CMC which will artificially inflate the nanoparticle size measured by that technique. The discrepancy in the TEM may be due to poor sampling. TEM samples were collected using. The reported particle sizes are however generally of the same order of magnitude as the values suggested in literature by Liu et al. [169], who found a range between 30-40 nm, and He and Zhao [170], who found a range between 15-20 nm.

As previously noted by Daun et al. [75] and the present work, the TAC of monatomic gases is generally expected to increase asymptotically with increases in the reduced mass. Further, the polyatomic gases are generally expected to lie below this trend implying that energy is accommodated less efficiently into the rotational modes over the translational modes, as

Table 7-1: Inferred TACs and nanoparticle diameters for TiRe-LII experiments on iron along with particle sizes from DLS and TEM. Included error is a result of epistemic uncertainty. Credibility intervals associated with aleatoric uncertainity are shown in square brackets below each value.

Surface-Gas Pair	α	d_p
Fe-He	0.05 ±0.01 [0.048,0.051]	26 ±8 [25.8,26.6]
Fe-Ne	0.18 ±0.05 [0.174,0.192]	25 ±7 [24.6,26.2]
Fe-Ar	0.19 ±0.07 [0.173,0.190]	20 ±6 [18.9,20.0]
Fe-N_2	0.09 ±0.02 [0.082,0.087]	21 ±6 [21.0,21.8]
Fe-CO	0.14 ±0.04 [0.134,0.146]	28 ±8 [26.9,28.2]
Fe-N_2O	0.11 ±0.03 [0.107,0.116]	21 ±6 [20.6,21.6]
Fe-CO_2	0.15 ±0.04 [0.139,0.152]	22 ±7 [21.6,22.8]
DLS	-	150 ±13
TEM	-	~150
Literature	-	~15-40

observed in carbon by Daun [23]. To this effect, the TACs observed in the present experiment are plotted against reduced mass in Figure 7-4. The trends match those observed in the previous experimentation with the monatomics increasing asymptotically and all of the polyatomics lying below that observed trend.

Further comparison is provided by comparing current literature values for the TAC provided from the MD study above and experimental work by Kock et al. [33] and Eremin et al. [35], summarized in Table 7-2. A special note must be made for the value of Fe-N_2 reported by Kock et al. [33]. In that work, Kock et al. only considered the translational degrees of freedom in evaluating the conduction from the nanoparticles. In consequence, the TAC will be overestimated. To correct for this, an additional factor must be included based on the following equivalence

$$2\alpha_{trans} = \left(2 + \frac{\zeta_{rot}}{2}\right)\alpha_{rot} \tag{7.8}$$

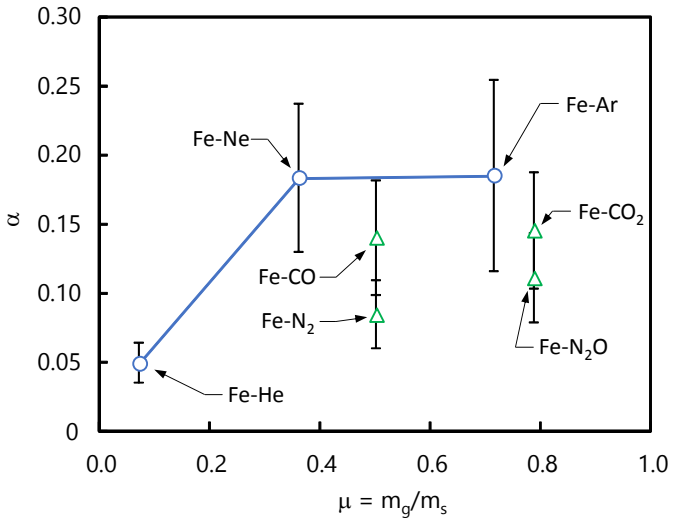

Figure 7-4: The TACs plotted against reduced mass, $\mu = m_g/m_s$,. Triangles represent polyatomic gas molecules and circles represent monatomic gas molecules. Error bars represent the epistemic uncertainty estimated in §7.3.2.

where the left hand side comes from only considering the translational degrees of freedom, that is $\zeta_{rot} = 0$, and the right hand side comes from considering $\zeta_{rot} \neq 0$. Given that $\zeta_{rot} = 2$ for nitrogen, this can be simplified

$$\alpha_{rot} = \frac{2\alpha_{trans}}{3} \tag{7.9}$$

which, in the case of $\alpha_{trans} = 0.13$ reported by Kock et al., gives $\alpha_{rot} = 0.09$. As it so happens, this value corresponds quite well to the one found in the present experimental study.

Agreement among the other gases is not as prominent. Fe-Ar is the most studied pair, but also has a considerable amount of spread across the range of studies. Adding to the situation, Kock et al. [33] and Eremin et al. [35] did not attempt to estimate the alleatoric and epistemic uncertainty in their studies where they inferred the TAC. This is particularly of note in the case of Eremin, et al., where only one significant digit is reported. The precise reason for the discrepancy remains unknown. The results for Fe-He span a full order of magnitude ranging from 0.11 in the MD studies to 0.01 by Eremin et al. The reason for this discrepancy also remains unknown.

7.3.1 Aleatoric Uncertainty

The posterior probability density, shown in Figure 7-5 for Fe-Ar, confirms an elongated valley of solutions that give high values for the posterior probability, similar to what was observed in molybdenum in Chapter 5. Unlike molybdenum, there is some curvature in the valley which can be attributed to the greater significance of evaporation in the cooling of the nanoparticle. Alleatoric uncertainty in the inferred parameters is evaluated by MCMC, analogous to §5.3.1 for silicon, and reported in Table 7-1. The MCMC samples are also overlaid on the posterior density of Fe-Ar in Figure 7-5.

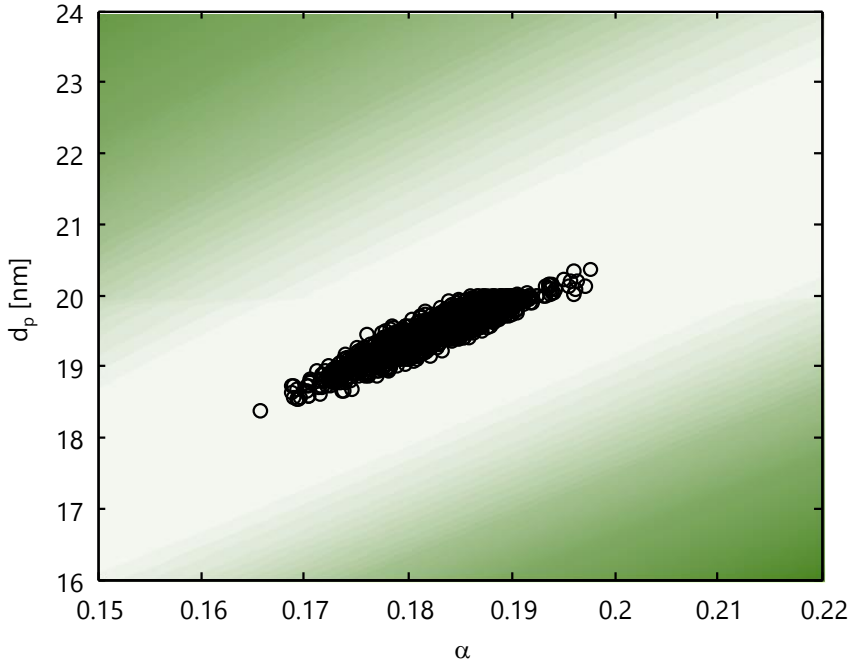

Figure 7-5: MCMC samples laid over contours of the logarithmic posterior distribution.

Table 7-3: Relative sensitivity coefficients and estimated error for the particle size and TAC due to model parameters.

	d_p [nm]		α	
	RSC	**ε**	**RSC**	**ε**
T_g	0.15	±0.015	0.12	±0.012
p_g	0.044	±0.0044	-0.18	∓0.018
c_p	-17	∓1.7	0.023	±0.0023
ρ	-20	∓2.0	-0.0044	∓0.00044
γ_s	0.78	±0.078	-0.00016	∓1.6E-5
$\frac{E(\mathbf{m}_{\lambda,2})}{E(\mathbf{m}_{\lambda,1})}$	54	±5.4	0.66	±0.066
Δh_v	-8.7	∓0.87	0.019	±0.0019
T_{cr}	0.81	±0.081	0.0038	±0.00038

7.3.2 Epistemic Uncertainty

Model parameter uncertainty is determined analogous to method used in §7.3.2 for silicon. Uncertainties in T_g, ρ, c_p, p_g, $E(\mathbf{m}_{\lambda,2})/E(\mathbf{m}_{\lambda,1})$, γ_s, Δh_v, and T_{cr} are taken to be 10% of their nominal values. Values reported in Table 7-3 are the relative sensitivity coefficients with errors found using Eq. 4.14

$$\varepsilon\left(x\,|\,\phi\right) = PE\left(\phi\right) \times RSC\left(\phi, x\right) \tag{7.10}$$

based on the above stated percentage errors. The total effect of parameter uncertainty can be estimated using the Kline-McClintock method [177]

$$\Delta x_{tot} = \left[\sum_{n=1}^{N}\left(\frac{\partial x}{\partial \phi_n}\cdot\Delta\phi_n\right)^2\right]^{1/2} \tag{7.11}$$

For Fe-Ar, this procedure results in uncertainties of $\Delta\alpha = 0.070$ and $\Delta d_p = 6.0$ nm, corresponding to 31% and 38% of the maximum likelihood estimates, respectively. The Kline-McClintock errors are also reported for other gas-surface pairs in Table 7-1. These error bounds are considerably larger in magnitude than the credible intervals associated with aleatoric uncertainty.

Chapter 8

Future Work

This work successfully shows applications of TiRe-LII to molybdenum, silicon, and iron. Much of the focus of this work was in quantifying the thermal accommodation coefficient for these different materials, including supporting molecular dynamics simulations. In all this there is much opportunity for further study. This chapter described what could be done in the future in terms of molecular dynamics simulations (§8.1), experimental work (§8.2), and modelling improvement (§8.3).

8.1 Molecular Dynamics Modeling of Accommodation Coefficients

The natural progression of this work is to include additional gas-surface pairs in the molecular dynamics simulations. As LAMMPS provides an efficient platform for calculating these values and numerous interatomic potentials, it is considered the better of the two softwares used in Chapter 3. As the iron and molybdenum pairs have not been evaluated using the LAMMPS code, it would be recommended to reevaluate these pairs using the LAMMPS code to confirm the values found by the in-house code. As an extension to this, it would be beneficial to evaluate for TAC for Fe-Ne and the various polyatomics examined experimentally in Chapter 7.

8.2 Experimental Development

8.2.1 Collaboration on TiRe-LII Analysis of Molybdenum Nanoparticles

Recently, researchers at the Joint Institute of High Temperature in Moscow have started work in analyzing molybdenum nanoparticles by TiRe-LII [178]. Due to our recent work on molybdenum, both using MD and TiRe-LII, it would be useful to work in conjunction with the institute to independently verify our molecular dynamics simulations and experimental analysis and work towards better understanding TiRe-LII analysis of molybdenum nanoparticles.

8.2.2 Collaboration with the CENIDE

Continued collaboration with the Center for Nanointegration Duisburg-Essen (CENIDE) would continue to develop an understanding of the principles underlying TiRe-LII on silicon

nanoparticles. It would be quite useful to use TEM analysis as a secondary characterization of the silicon nanoparticles. This would allow for better validation of the results than the present BET analysis, which is incapable of quantifying the particle distribution width and morphology. Work with CENIDE could also investigate the spectral distribution of emission from the nanoparticle to ensure the the TiRe-LII signal is not being contaminated with other laser-induced emission.

8.2.3 Refinement of Iron Experiments

As mentioned in Chapter 7, the iron experiments presented in this work represent preliminary studies. Further work can be done to refine these experiments in multiple ways including: further literature of the vapor and optical properties, re-evaluation of the data in Kock et al. [33] for comparison purposes, sealing the iron nanoparticle container from external contaminates, using an electrostatic TEM sample, and examining the peak temperatures to validate the results.

8.3 Model Development

8.3.1 Extended Robust Bayesian Analysis

The statistical methods used in determining uncertainty in the model parameters could be developed further. In particular, it could be useful to extend the Bayesian framework to accommodate uncertainty in the model parameters. This would allow one to develop a single uncertainty bound in the inferred parameters rather than separate uncertainties for the aleatoric and epistemic uncertainties.

8.3.2 Development of Transferable Models

There is presently a large array of models used in TiRe-LII analyses. Michelson et al. [46], for example, examined thirteen different models from an assortment of labs and showed how much the results could vary based on the different models. This gives reason to a standardized formats by which models can be exchanged between labs. The author suggests that text files be used that contain information from each of the models that can be exchanged between labs. This will allow each lab to keep its current models while easily collaborating and verifying their results with other labs. The most imminent way to do this would be to cooperate with CENIDE in developing text files that can be used to compare different silicon models while still employing different base codes.

8.3.3 Regime Based Modeling

Whether the particles are in a distribution or not, it would be effective to do regime based modeling where the particles are automatically modeled using the most simplified version of the model applicable. For example, in very small particles where size-dependent effects may become important, it would be useful to automatically model these effects. However, for large particles, possibly in the same distribution, it would also be useful to exclude these effects to allow for more efficient analysis.

8.3.4 Optical Constants

The optical constants remains a major uncertainty in TiRe-LII analysis, both when considering soot or non-carbonaceous particles. Literature also suggests that Drude theory may be adequate for modelling for both the metals and silicon [52,162]. Further study is required to examine the precise uncertainty in the optical constants used in TiRe-LII analyses.

Appendix A

The Velocity-Verlet Algorithm

The velocity verlet algorithm is an integration technique used to solve atomic trajectories in molecular dynamics simulations. The Taylor expansion of the position of an atom at any time, *b*, centered at time, *a*, is given by

$$x(b)=\sum_{n=0}^{\infty}\frac{f^{(n)}(a)}{n!}(b-a)^{n} \qquad \text{A.1}$$

Consider the case for a Taylor series approximation of the position of an atom at time

$$b=t_{i+1}=t_i+\Delta t \qquad \text{A.2}$$

based on the position of the atom at

$$a=t_i \qquad \text{A.3}$$

The Taylor series expansion then becomes,

$$x(t_{i+1})=\sum_{n=0}^{\infty}\frac{f^{(n)}(t_i)}{n!}(\Delta t)^{n} \qquad \text{A.4}$$

Considering the second order approximation of this sum, one gets

$$x(t_{i+1})=x(t_i)+f^{(1)}(t_i)\Delta t+\frac{1}{2}f^{(2)}(t_i)(\Delta t)^{2} \qquad \text{A.5}$$

which is analogous to

$$x_{i+1}=x_i+v_i\Delta t+\frac{1}{2}a_i(\Delta t)^{2} \qquad \text{A.6}$$

where v_i and a_i are the velocity and acceleration of the atom at the i^{th} time step. Performing the same steps for $x_{i\text{-}1}$, gives

$$x_{i-1}=x_i-v_i\Delta t+\frac{1}{2}a_i(\Delta t)^{2} \qquad \text{A.7}$$

Subtracting Eq. B.6 from Eq. B.5 gives

$$v_i=\frac{x_{i+1}-x_{i-1}}{2\Delta t} \qquad \text{A.8}$$

with an associated error of the order of Δt^4. Analogously, adding Eq. B.6 and Eq. B.5 gives

$$x_{i+1} = 2x_i - x_{i-1} + a_i \left(\Delta t\right)^2 \quad \text{A.9}$$

with an associated error of Δt^3. Moving forward a time step, Eq. A.8 can be expressed as

$$v_{i+1} = \frac{x_{i+2} - x_i}{2\Delta t} \quad \text{A.10}$$

and Eq. A.9 can be expressed as

$$x_{i+2} = 2x_{i+1} - x_i + a_{i+1} \left(\Delta t\right)^2 \quad \text{A.11}$$

Substituting Eq. A.11 into Eq. A.10 gives

$$v_{i+1} = \frac{x_{i+1} - x_i}{\Delta t} + \frac{1}{2} a_{i+1} \Delta t \quad \text{A.12}$$

Further algebra and substitution of Eq. A.6, gives the final form of the velocity Verlet equation,

$$v_{i+1} = v_i + \frac{1}{2}\left(a_i + a_{i+1}\right)\Delta t \quad \text{A.13}$$

Together, Eq. A.6 and Eq. A.13, define the subsequent position and velocity of the atom based solely on the current i^{th} state. This does require that Eq. A.6 be solved first, such that a_{i+1} can be determined from Newton's second law as a function of x_{i+1} such that

$$a_{i+1} = \frac{F_{i+1}\left(x_{i+1}\right)}{m} \quad \text{A.14}$$

where $F_{i+1}(x_{i+1})$ is determined based on the pre-defined interatomic potential. As this only considers the forces resulting from the interatomic potentials, this is considered the standard way of propagating a molecular dynamic simulation without adding external energy, consistent with the NVE ensemble.

Appendix B

Gas Velocity Sampling Procedure

In order for molecular dynamics simulations to model the physics of the gas-surface interaction, it is necessary to sample gas velocities in a physical way. The thermal accommodation coefficient is given by Eq. 2.13

$$\alpha = \frac{\langle E_o - E_i \rangle}{\langle E_o - E_i \rangle_{max}} \tag{B.1}$$

where E_i and E_o are the initial and final energies of the gas molecule and < … > denote the average. As stated in Eq. 2.14, the energy of a gas molecule can be calculated based on a temperature such that

$$\bar{E} = \frac{1}{2} k_B T_g \zeta_{tot} = \frac{1}{2} k_B T_g \left(\zeta_{trans} + \zeta_{rot} + \zeta_{vib} \right) \tag{B.2}$$

or, as discussed in §2.2.1, more simply as

$$\bar{E} = \left(2 + \frac{\zeta_{rot}}{2} \right) k_B T_g \tag{B.3}$$

which allows

$$\langle E_o - E_i \rangle_{max} = \left(2 + \frac{\zeta_{rot}}{2} \right) k_B \left(T_p - T_g \right) \tag{B.4}$$

In these simulations, an alternative definition of the gas molecules energy must be defined, based on the velocity of the gas molecules

$$E = \frac{1}{2} \sum_j m_j v_j^2 \tag{B.5}$$

where v_i and m_j are the velocity and mass of the j^{th} atom in the gas molecule. The average energy change can thus be expressed as

$$\left\langle E_o - E_i \right\rangle = \frac{1}{2}\int_{-\infty}^{\infty}\int_{-\infty}^{\infty}\sum_j \left[m_j \left(v_{o,j}^2 - v_{i,j}^2 \right) \right] dv_{i,j}\, dv_{o,j} \qquad \text{B.6}$$

The initial velocities, $v_{i,j}$, will follow the Maxwell-Boltzmann distribution such that the distribution of velocities are given by

$$f(v) = \sqrt{\left(\frac{m}{2\pi k_B T_g} \right)^3} 4\pi v^2 \exp\left(-\frac{mv^2}{2k_B T_g} \right) \qquad \text{B.7}$$

and the output velocities, $v_{o,j}$, are described based on the ouput to the simulations. This integral will be estimated using Monte Carlo integration such that

$$\left\langle E_o - E_i \right\rangle = \frac{1}{2N}\sum_{k=1}^{N}\sum_j \left[m_j \left(v_{o,j,k}^2 - v_{i,j,k}^2 \right) \right] \qquad \text{B.8}$$

where $v_{i,j,k}$ is randomly sampled from the Maxwell Boltzmann distribution and $v_{o,j,k}$ is the corresponding output of the simulation corresponding to that initial velocity. Due to the random nature of the Monte Carlo integration, it is assumed that the double integral can be estimated using a single sum as there will be sufficient sampling of the output distribution from the randomly chosen input distribution.

Using the Maxwell-Boltmann distribution, random samples of the initial bulk gas molecule velocities is given by

$$v_i = \frac{\left[-\ln\left(R_f \right) \right]^{1/2}}{\beta} \sin\left(2\pi R_f \right) \qquad \text{B.9}$$

where $\beta = [m/(2k_B R T_g]^{1/2}$ and R_f is a random number sampled from a uniform distribution between 0 and 1 [61]. The velocity component in the vertical direction is modified as gas atoms with a greater vertical component preferentially cross the border

$$v_z = -\frac{\left[-\ln\left(R_f \right) \right]^{1/2}}{\beta} \qquad \text{B.10}$$

Having correctly sampled the initial gas velocities, this allows for evaluation of the accommodation coefficient by

$$\alpha = \frac{1}{\left(2+\zeta_{rot}/2\right)k_B\left(T_p - T_g\right)}\frac{1}{2N}\sum_{k=1}^{N}\sum_{j}\left[m_j\left(v_{o,j,k}^2 - v_{i,j,k}^2\right)\right] \qquad \text{B.11}$$

As this is being estimated by Monte Carlo integration, the uncertainty in the solution is expected to drop according to

$$\hat{\varepsilon} = \frac{1}{\sqrt{N}} \qquad \text{B.12}$$

where N is the number of Monte Carlo samples. Figure B-1 shows this graphically, with the uncertainty in the value of α for a Si-Ar simulation diminishing with increasing N.

As an example, consider the case where one only wanted to consider the translational mode (representative of Si-Ar, Fe-Ar, Fe-He, and many others), one would only consider the velocity of the center of mass of the gas molecule, such that

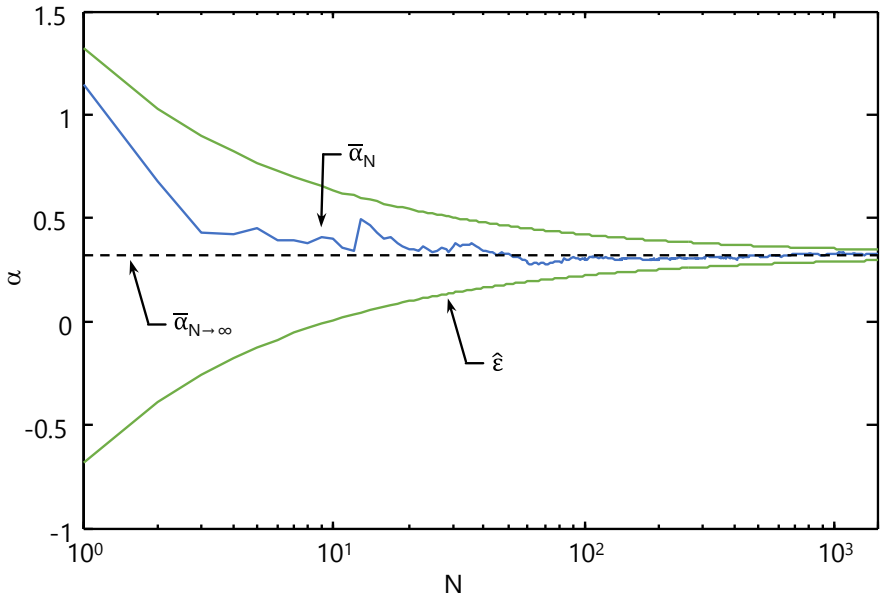

Figure B-1: The reduction in the expected uncertainty, $\hat{\varepsilon}$, associated with α for an increasing number of samples, N, given by $\hat{\varepsilon} = 1/(N)^{1/2}$. In the present figure $\bar{\alpha}_N$ is the average value of α evaluated for N samples and $\bar{\alpha}_{N\to\infty}$ is the expected value of α as the number of samples approaches infinity.

$$\alpha = \frac{m_g}{4k_B\left(T_p - T_g\right)}\frac{1}{N}\sum_{k=1}^{N}\left[\left(v_{o,k}^2 - v_{i,k}^2\right)\right] \qquad \text{B.13}$$

or

$$\alpha = \frac{m_g}{4k_B\left(T_p - T_g\right)}\left\langle v_{o,k}^2 - v_{i,k}^2 \right\rangle \qquad \text{B.14}$$

where <.> denotes the average. Normal and tangential components of the accommodation coefficient can be found analogously by

$$\alpha_n = \frac{m_g\left\langle w_{g,o}^2 - w_{g,i}^2 \right\rangle}{2k_{\mathrm{B}}\left(T_p - T_g\right)} \qquad \text{B.15}$$

and

$$\alpha_t = \frac{m_g\left\langle \mathbf{v}_{t,o}\cdot\mathbf{v}_{t,o} - \mathbf{v}_{t,i}\cdot\mathbf{v}_{t,i} \right\rangle}{2k_{\mathrm{B}}\left(T_p - T_g\right)} \qquad \text{B.16}$$

respectively, where w_g and $v_{g,t}$ are the normal and tangential velocities of the gas molecule. It is important to note that the number of degrees of freedom reduces in Eq. B.15 and Eq. B.16, resulting in a smaller denominator.

Appendix C

Minimization and Statistical Algorithms

Minimization is an important part of TiRe-LII analysis. In the present work, several minimization techniques are applied to infer parameters from experimental data. This appendix describes several of these procedures in more detail.

C.1 Levenberg-Marquardt

Levenberg-Marquardt [138,139] is an algorithm applied to least-squares curve fitting, and is built into programs such as Matlab. Generally, least squares problems can be defined by

$$S(\boldsymbol{\beta}) = \sum_{i=1}^{n} w_i \left[y_i - f\left(x_i, \boldsymbol{\beta}\right) \right]^2 \qquad \text{C.1}$$

where $S(\boldsymbol{\beta})$ is the objective function to be minimized by changing the set of parameters of interest, $\boldsymbol{\beta}$. The Levenberg-Marquardt algorithm works as an iterative algorithm changing $\boldsymbol{\beta}$ in each iteration by

$$\boldsymbol{\beta}_{j+1} = \boldsymbol{\beta}_j + \boldsymbol{\delta} \qquad \text{C.2}$$

where the function of interest is approximated by its first order Taylor series expansion

$$f\left(x_i, \boldsymbol{\beta}_j + \boldsymbol{\delta}\right) \cong f\left(x_i, \boldsymbol{\beta}_j\right) + J_i \boldsymbol{\delta} \qquad \text{C.3}$$

where

$$J_i = \left. \frac{\partial f\left(x_i, \boldsymbol{\beta}\right)}{\partial \boldsymbol{\beta}} \right|_j \qquad \text{C.4}$$

giving

$$S\left(\boldsymbol{\beta}_{j+1}\right) \cong \sum_{i=1}^{n} w_i \left[y_i - f\left(x_i, \boldsymbol{\beta}_j\right) + J_i \boldsymbol{\delta} \right]^2 \qquad \text{C.5}$$

or in vector notation

$$S\left(\boldsymbol{\beta}_{j+1}\right) \cong \left\| \mathbf{w} \left[\mathbf{y} - \mathbf{f}\left(\boldsymbol{\beta}_j\right) + \mathbf{J}_j \boldsymbol{\delta} \right] \right\|^2 \qquad \text{C.6}$$

Where $\mathbf{J}_j$ is the Jacobian calculated at the j^{th} iteration. Taking the derivative with respect to $\boldsymbol{\delta}$ and setting the approximated objective function to zero, that is its minimum possible value, yields

$$\left(\mathbf{J}_j^T \mathbf{J}_j\right)\boldsymbol{\delta} = \mathbf{w}\mathbf{J}^T\left[\mathbf{y} - \mathbf{f}\left(\boldsymbol{\beta}_j\right)\right] \qquad \text{C.7}$$

Levenberg [138] added a damping term to the left hand side of the equation such that

$$\left(\mathbf{J}_j^T \mathbf{J}_j + \lambda\mathbf{I}\right)\boldsymbol{\delta} = \mathbf{w}\mathbf{J}_j^T\left[\mathbf{y} - \mathbf{f}\left(\boldsymbol{\beta}_j\right)\right] \qquad \text{C.8}$$

where λ is a damping coefficient and $\mathbf{I}$ is the identity matrix. Subsequent iterations of $\boldsymbol{\beta}$ can be found by solving the above equation for $\boldsymbol{\delta}$ and calculating $\boldsymbol{\beta}_{j+1}$ by Eq. C.2. Iterations stops based on a predefined limit on changes in $\boldsymbol{\beta}$, that is, the value of $\boldsymbol{\delta}$.

C.2 Bootstrapping

Bootstrapping or, as Press et al. [167] refer to it, *quick-and-dirty* Monte Carlo is a powerful statistical technique that can be used to quickly estimate confidence in a set of inferred parameters even when the underlying nature of the process is unknown. The one requirement for the technique to be valid is that the data set consists of *N* independent and identically distributed (iid) data points, that is, the data is not dependent on its position within the set. Having satisfied this condition, bootstrapping involves randomly resampling the data with repetition from the original set. One then subjects the new data set to any point estimation technique, such as the one described in §C.1. The result is a series of estimators that depend on the spread in the original data set and can be used to estimate the variability in inferred parameters.

In this case, the residuals between the modeled and experimental temperature can be considered to be a set of independent data. As the residual is expected to be larger at higher temperatures, it is normalized by the modeled temperature to effectively calculate the percentage residual at each point. In this case, the data is not generally identically distributed as the signal-to-noise ratio changes as the signal decreases. To account for this, the residual can be studentized [143]. Studentization uses the hat matrix, defined as

$$H = X\left(X^T X\right)^{-1} X^T \qquad \text{C.9}$$

where

$$X = \begin{bmatrix} 1 & x_1 \\ \vdots & \vdots \\ 1 & x_N \end{bmatrix} \tag{C.10}$$

The studentized residual is given as

$$\frac{\hat{\epsilon}_i}{\hat{\sigma}\sqrt{1-h_{ii}}} \tag{C.11}$$

where ε_i is the i^{th} residual, σ is the standard deviation of the data set, and h_{ii} is the leverage given as the diagonal of the hat matrix, H. The studentized residuals can be sampled with repetition to generate new set of studentized residuals. Reversing the process of studentizing and normalizing, a new set of experimental temperature is produced allowing one to infer a new set of parameters of interest. Repeating this process will give a distribution of the inferred parameters that can be used to estimate uncertainty resulting from noise in the experimentally measured temperatures.

C.3 Marcov Chain Monte Carlo

Marcov Chain Monte Carlo (MCMC) is a random sampling technique used to characterize a probability distribution. This is of particular interest in the present work as it can provide estimates of the degree of uncertainty resulting from Bayesian inference. In Bayesian statistics, the posterior distribution, $P(\mathbf{b}|\mathbf{x})$ is defined based on Eq. 4.4 such that

$$P(\mathbf{x}|\mathbf{b}) = \frac{P(\mathbf{b}|\mathbf{x})P_{pr}(\mathbf{x})}{P(\mathbf{b})} \tag{C.12}$$

In many cases it is computationally intractable to estimate the evidence and it is easier to work with $\pi(\mathbf{x})$ such that

$$P(\mathbf{x}|\mathbf{b}) \propto \pi(\mathbf{x}) \equiv P(\mathbf{b}|\mathbf{x})P_{pr}(\mathbf{x}) \tag{C.13}$$

MCMC estimates $\pi(\mathbf{x})$ based on two insights [167]. First, one should sample from a Marcov chain instead of unrelated, independent points. A Marcov chain involves sampling in a chain wherein every sample in the generated set $\{\mathbf{x}_0, \mathbf{x}_1, \mathbf{x}_2, \ldots \mathbf{x}_n\}$ is sampled based on information added from one preceding sample, that is

$$p\left(\mathbf{x}_{i+1}\right) = p\left(\mathbf{x}_{i+1} \mid \mathbf{x}_i\right) \tag{C.14}$$

Second, each sample is chosen such that it satisfies the equation of detailed balance

$$\pi\left(\mathbf{x}_1\right) p\left(\mathbf{x}_2 \mid \mathbf{x}_1\right) = \pi\left(\mathbf{x}_2\right) p\left(\mathbf{x}_1 \mid \mathbf{x}_2\right) \tag{C.15}$$

which effectively states that is $\mathbf{x}_1$ is sampled from $\pi(\mathbf{x})$, then so is $\mathbf{x}_2$. When combined, it can be shown that these two insights with result in a set $\{\mathbf{x}_0, \mathbf{x}_1, \mathbf{x}_2, \ldots \mathbf{x}_n\}$ that efficiently samples $\pi(\mathbf{x})$, that is, the set of samples is ergodic. The real difficulty is coming up with algorithms that can generate a transition functions, $p(\mathbf{x}_i|\mathbf{x}_{i+1})$, that satisfies Eq. C.15. There are several algorithms available for this task.

In this work, MCMC is performed using the Metropolis-Hasting algorithm. In this algorithm, one picks a proposal distribution, $q(\mathbf{x}_{i+1}|\mathbf{x}_i)$, that satisfies one condition: it can sample anywhere in the region being considered [167]. Using this proposed distribution, one generates a candidate sample, $x_{i+1,c}$, and calculates an acceptance probability, $\alpha(\mathbf{x}_i, \mathbf{x}_{i+1,c})$, using

$$\alpha\left(\mathbf{x}_i, \mathbf{x}_{i+1,c}\right) = \min\left(1, \frac{\pi\left(\mathbf{x}_{i+1,c}\right) q\left(\mathbf{x}_i \mid \mathbf{x}_{i+1,c}\right)}{\pi\left(\mathbf{x}_i\right) q\left(\mathbf{x}_{i+1,c} \mid \mathbf{x}_i\right)}\right) \tag{C.16}$$

Having calculated an acceptance probability, one either accepts or rejects the candidate sample such that

$$\mathbf{x}_{i+1} = \begin{cases} x_i & \text{if } \alpha\left(\mathbf{x}_i, \mathbf{x}_{i+1,c}\right) < \left\{R \sim U\left(0,1\right)\right\} \\ x_{i+1,c} & \text{if } \alpha\left(\mathbf{x}_i, \mathbf{x}_{i+1,c}\right) \geq \left\{R \sim U\left(0,1\right)\right\} \end{cases} \tag{C.17}$$

This acceptance probability preferentially selects candidate samples with a higher probability while allowing for some acceptance of points with a lower probability, effectively allowing the algorithm to move around points near a minima and climb out of local minima. A common choice for the proposed distribution is a normal distribution centered on the previous sample with a standard deviation heuristically chosen to optimize the ratio of accepted to rejected candidate samples generally following [179], that is

$$\mathbf{x}_{i+1,c} \sim N\left(x_i, \sigma\right) \tag{C.18}$$

In this work, the author uses the normal distribution to sample the distribution proportional to the logarithmic posterior

$$\pi(\mathbf{x}_i) \propto \log\left[P(\mathbf{x}|\mathbf{b})\right] \tag{C.19}$$

In this work, this can simply be simplified to the logarithmic likelihood, within a certain range of **x**.

References

[1] Moisala, A. et al., 2005, "On-Line Detection of Single-Walled Carbon Nanotube Formation During Aerosol Synthesis Methods," *Carbon*, **43**(10), pp. 2066-2074.

[2] Maier, S. A. and Atwater, H. A., 2005, "Plasmonics: Localization and Guiding of Electromagnetic Energy in Metal/Dielectric Structures," *J. Appl. Phys.*, **98**(1), No. 011101.

[3] Atwater, H. A. and Polman, A., 2010, "Plasmonics for Improved Photovoltaic Devices," *Nat. Mater.*, **9**(3), pp. 205-213.

[4] Huber, D. C., 2005, "Synthesis, Properties, and Applicatins of Iron Nanoparticles," *Small*, **1**(5), pp. 482-501.

[5] O'Farrell, Norah, Houlton, Andrew, and Horrocks, Benjamin R., 2006, "Silicon Nanoparticles: Applications in cell Biology and Medicine," *Int. J. Nanomed.*, **1**(4), pp. 451-472.

[6] Konstantatos, G. et al., 2006, "Ultrasensitive Solution-Cast Quantum Dot Photodetectors," *Nature*, **442**(7099), pp. 180-183.

[7] Wu, Hui et al., 2013, "Stable Li-ion Battery Anodes by In-Situ Polymerization of Conducting Hydrogel to Conformally Coat Silicon Nanoparticles," *Nat. Commun.*, **4**, No. 1943.

[8] Pavesi, Lorenzo and Turan, Rasit, 2010, *Silicon Nanocrystals - Fundamentals, Synthesis and Applications*, John Wiley & Sons.

[9] Boiarciuc, A., Foucher, F., and Mounaim-Rousselle, C., 2006, "Soot Volume Fractions and Primary Particle Size Estimate by Means of the Simultaneous Two-Color-Time-Resolved and 2D Laser-Induced Incandescence," *Appl. Phys. B*, **83**(3), pp. 413-421.

[10] Delhay, J. et al., 2009, "Soot Volume Fraction Measurements in Aero-Engine Exhausts Using Extinction-Calibrated Backward Laser-Induced Incandescence," *Appl. Phys. B*, **95**(4), pp. 825-838.

[11] Black, J.D. and Johnson, M.P., 2010, "In-Situ Laser-Induced Incandescence of Soot in an Aero-Engine Exhaust: Comparison with Certification Style Measurements," *Aerosp. Sci. Technol.*, **14**(5), pp. 329-337.

[12] Dec, J.E., 1992, "Soot Distribution in a D.I. Diesel Engine Using 2-D Imaging of Laser-induced Incandescence, Elastic Scattering, and Flame Luminosity," *SAE Tech. Paper Ser.*, No. 920115.

[13] Dec, J. E., Loye, A. O. Zur, and Siebers, D. L., 1991, "Soot Distribution in a DI Diesel Engine using 2-D Laser-Induced Incandescence Imaging," *SAE Tech. Paper Ser.*, No. 910224.

[14] Espey, C. and Dec, J.E., 1993, "Diesel Engine Combustion Studies in a Newly Designed Optical-Access Engine using High-Speed Visualization and 2-D Laser Imaging," *SAE Tech. Paper Ser.*, No. 930971.

[15] Tait, N. P. and Greenhalgh, D. A., 1993, "PLIF Imaging of fuel Fraction in Practical Devices and LII Imaging of Soot," *Ber. Bunsenges. Phys. Chem.*, **97**(12), pp. 1619-1625.

[16] Vander Wal, R. L. and Weiland, K.J., 1994, "Laser-Induced Incandescence: Development and Characterization Towards a Measurement of Soot-Volume Fraction," *Appl. Phys. B*, **59**(4), pp. 445-452.

[17] Vander Wal, R. L. and Dietrich, D. L., 1995, "Laser-Induced Incandescence Applied to Droplet Combustion," *Appl. Opt.*, **34**(6), pp. 1103-1107.

[18] Weeks, R. W. and Duley, W. W., 1974, "Aerosol-Particle Sizes from Light Emission during Excitation by TEA CO2 Laser Pulses," *J. Appl. Phys.*, **45**(10), pp. 4661-4663.

[19] Eckbreth, A. C., 1977, "Effects of Laser-Modulated Particulate Incandescence on Raman Scattering Diagnostics," *J. Appl. Phys.*, **18**(11), pp. 4473-4479.

[20] Filippov, A.V., Zurita, M., and Rosner, D.E., 2000, "Fractal-Like Aggregates: Relation between Morphology and Physical Properties," *J. Colloid Interface Sci.*, **229**(1), pp. 261-273.

[21] Liu, F. et al., 2006, "Influence of Polydisperse Distributions of both Primary Particle and Aggregate Size on Soot Temperature in Low-Fluence LII," *Appl. Phys. B*, **83**(3), pp. 383-395.

[22] Liu, F. and Smallwood, G.J., 2008, "Study of Heat Conduction between Fractal Aggregates and the Surrounding Gas in the Transition Regime Using the DSMC Method," *40th Thermophysics Conference*, Seattle, WA, pp. 1-10.

[23] Lehre, T. et al., 2003, "Size Distributions of Nanoscaled Particles and Gas Temperatures from Time-Resolved Laser-Induced Incandescence Measurements," *Appl. Opt.*, **42**(12), pp. 2021-2029.

[24] Kuhlmann, S. A. et al., 2004, "Evaluation and Improvement of Laser-Induced Incandescence for Nanoparticle Sizing," *Proc. PARTEC*, Nuremburg, Germany.

[25] Eremin, A. V. et al., 2006, "TR-LII for Sizing of Carbon Particles Forming at Room Temperature," *Appl. Phys. B*, **83**(3), pp. 449-454.

[26] Gurentsov, E. V., Eremin, A. V., and Schulz, C., 2007, "Formation of Carbon Nanoparticles by the Condensation of Supersaturated Atomic Vapor Obtained by the Laser Photolysis of C3O2," *Kinet. Catal.*, **48**(2), pp. 194-302.

[27] Snelling, D. R. et al., 2004, "Determination of the Soot Absorption Function and Thermal Accommodation Coefficient Using Low-Fluence LII in a Laminar Coflow Ethylene Diffusion Flame," *Combust. Flame*, **136**, pp. 180-190.

[28] Kuhlmann, S. A., Reimann, J., and Will, S., 2006, "On Heat Conduction Between Laser-Heated Nanoparticles and a Surrounding Gas," *J. Aeerosol Sci.*, **37**(12), pp. 1696–1716.

[29] Vander Wal, R. L., Ticich, T. M., and West, J. R., 1999, "Laser-Induced Incandescence Applied to Metal Nanostructures," *Appl. Opt.*, **38**(27), pp. 5867-5879.

[30] Fillipov, A. V., Markus, M. W., and Roth, P., 1999, "In-Situ Characterization of Ultrafine Particles by Laser-Induced Incandescence: Sizing and Particle Structure Determination," *J. Aerosol Sci.*, **30**(1), pp. 71-87.

[31] Liu, F. et al., 2006, "Heat Conduction from a Spherical Nano-Particle: Status of Modelling Heat Conduction in Laser-Induced Incandescence," *Appl. Phys. B*, **83**(3), pp. 355-382.

[32] Starke, R., Kock, B., and Roth, P., 2003, "Nano-particle Sizing by laser-Induced Incandescence (LII) in a Shock Wave Reactor," *Shock Waves*, **12**(5), pp. 351-260.

[33] Kock, B. F. et al., 2006, "Comparison of LII and TEM Sizing During Synthesis of Iron Particle Chains," *Proceedings of the Combustion Institute*, **30**(1), pp. 1689-1697.

[34] Friedlander, S. and C., Wang, 1966, "The Self-Preserving Particle Size Distribution for Coagulation by Brownian Motion," *J. Colloid Interface Sci.*, **22**(2), pp. 126-132.

[35] Eremin, A., Gurentsov, E., and Schulz, C., 2008, "Influence of the Bath Gas on the Condensation of Supersaturated Iron Atom Vapour at Room Temperature," *J. Phys. D: Appl. Phys.*, **41**(5), pp. 1-5, No. 055203.

[36] Eremin, A. et al., 2011, "Size Dependence of Complex Refractive Index Function of Growing Nanoparticles," *Appl. Phys. B*, **104**(2), pp. 289-295.

[37] Eremin, A. et al., 2013, "Experimental Study of Carbon and Iron Nanoparticle Vaporisation Under Pulse Laser Heating," *Appl. Phys. B*, **112**(3), pp. 421-432.

[38] Reimann, J. et al., 2010, "Laser Sintering of Nickel Aggregates Produced from Inert Gas Condensation," *Proceedings of the World Conference on Particle Technology*, **6**, Nuremberg, Germany.

[39] Daun, K. J., Titantah, J. T., and Karttunen, M., 2012, "Molecular Dynamics Simulation of Thermal Accommodation Coefficients for Laser-Induced Incandescence Sizing of Nickel Particles," *Appl. Phys. B*, **107**(1), pp. 221-228.

[40] Lehre, T., Suntz, R., and Bockhorn, H., 2005, "Time-Resolved Two-Color LII: Size Distributions of Nano-Particles from Gas-to-Particle Synthesis," *Proceedings of the Combustion Institute*, **30**(2), pp. 2585-2593.

[41] Cignoli, F. et al., 2009, "Laser-Induced Incandescence of Titania Nanoparticles Synthesized in a Flame," *Appl. Phys. B*, **96**(4), pp. 593-599.

[42] Maffi, S. et al., 2008, "Spectral Effects in Laser Induced Incandescence Application to Flame-Made Titania Nanoparticles," *Spectrochim Acta B*, **63**(2), pp. 202-209.

[43] Tribalet, B. et al., 2012, "Evaluation of Particle Sizes of Iron-Oxide Nano-Particles in a Low-Pressure Flame-Synthesis Reactor by Simultaneous Application of TiRe-LII and PMS," *5th Workshop on Laser-induced Incandescence*, Le Touquet, France.

[44] Altman, I. S. et al., 2001, "Experimental Estimate of Energy Accommodation Coefficient at High Temperatures," *Phys. Rev. E*, **64**(5), No. 052202.

[45] Murakami, Y., Sugatani, T., and Nosaka, Y., 2005, "Laser-Induced Incandescence Study on the Metal Aerosol Particles as the Effect of the Surrounding Gas Medium," *J. Phys. Chem. A*, **109**(40), pp. 8994-9000.

[46] Michelson, H. A. et al., 2007, "Modeling Laser-Induced Incandescence of Soot: A Summary and Comparison of LII Models," *Appl. Phys. B*, **87**(3), pp. 503-521.

[47] Melton, Lynn A., 1984, "Soot Diagnostics Based on Laser Heating," *Appl. Opt.*, **23**(13), pp. 2201-2208.

[48] Daun, K.J. et al., 2007, "Determining Aerosol Particle Size Distributions using Time-Resolved Laser-Induced Incandescence," *Appl. Phys. B*, **87**(2), pp. 363-372.

[49] Bohren, C. F. and Huffman, D. R., 1983, *Absorption and Scattering of Light by Small Particles*, John Wiley & Sons, New York.

[50] Modest, M. F., 2003, *Radiative Heat Transfer*, 3rd ed., Academic Press, New York.

[51] Palik, E. D., 1998, *Handbook of Optical Constants of Solids*, Academic Press, San Diego.

[52] Fuchs, M. S. K., 2000, "Optical properties of liquid silicon: the integral equation approach," *J. Phys. Condens. Matter*, **12**(19), pp. 4341-4351.

[53] Jellison, G. E. and Modine, F. A., 1983, "Optical Functions of Silicon between 1.7 and 4.7 eV at Elevated Temperatures," *Phys. Rev. B*, **27**(12), pp. 7466-7472.

[54] Jellison, G. E. and Modine, F. A., 1994, "Optical Functions of Silicon at Elevated Temperatures," *J. Appl. Phys.*, **76**(6), pp. 3758-3761.

[55] Jellison, G. E. and Lowndes, D. H., 1987, "Measurements of the Optical Properties of Liquid Silicon and Germanium using Nanosecond Time Resolved Ellipsometry," *Appl. Phys. Lett.*, **51**(5), pp. 352-354.

[56] Miller, J. C., 1969, "Optical Properties of Liquid Metals at High Temperatures," *Phil. Mag.*, **20**(168), pp. 1115-1132.

[57] Krishnan, S., Yugawa, K. J., and Nordine, P. C., 1997, "Optical Properties of Liquid Nickel and Iron," *Phys. Rev. B*, **55**(13), pp. 8201-8206.

[58] Elsayed-Ali, H. E. et al., 1987, "Time-Resolved Observation of Electron-Phonon Relaxation in Copper," *Phys. Rev. Lett.*, **58**(12), pp. 1212-1215.

[59] Williams, M. M. R. and Loyalka, S. K., 1991, *Aerosol Science: Theory and Practice*, Pergamon Press, Oxford.

[60] Atkins, P. and Paula, J., 2006, *Physical Chemistry*, 8th ed., W. H. Freeman and Company, New York.

[61] Bird, G. A., 2011, *Molecular Gas Dynamics and the Direct Simulation of Gas Flows*, Oxford University Press.

[62] Incopera, F. P., Bergman, D. P. DeWitt T. L., and Lavine, A. S., 2006, *Fundamentals of Heat and Mass Transfer*, 6th ed., John Wiley & Sons, USA.

[63] Daun, K.J. and Huberman, S.C., 2012, "Influence of Particle Curvature on Transition Regime Heat Conduction from Aerosolized Nanoparticles," *Int. J. Heat Mass Trans.*, **55**(25), pp. 7668–7676.

[64] Filippov, A. V. and Rosner., D. E., 2000, "Energy Transfer between an Aerosol Particle and Gas at High Temperature Ratios in the Knudsen Transition Regime," *Int. J. Heat Mass Transfer*, **43**(1), pp. 127-138.

[65] Daun, K. J., 2009, "Thermal Accommodation Coefficients Between Polyatomic Gas Molecules and Soot in Laser-Induced Incandescence Experiments," *Int. J. Heat Mass Transfer*, **52**(21), pp. 5081-5089.

[66] Bird, R. B., Stewart, W. E., and Lightfoot, E. N., 1966, *Transport Phenomena*, John Wiley & Sons, New York.

[67] Velasco, S. et al., 2006, "Prediction of the Enthalpy of Vaporization of Metals and Metalloids," *Fluid Phase Equilib.*, **244**(1), pp. 11-15.

[68] Watson, K. M., 1943, "Thermodynamics of the Liquid State," *Ind. Eng. Chem.*, **35**(4), pp. 398-406.

[69] Nanda, K. K., Kruis, F. E., and Fissan, H., 2002, "Evaporation of Free PbS Nanoparticles: Evidence of the Kelvin Effect," *Phys. Rev. Lett.*, **89**(25), No. 256103.

[70] Nanda, K. K. et al., 2003, "Higher Surface Energy of Free Nanoparticles," *Phys. Rev. Lett.*, **91**(10), No. 106102.

[71] Lu, H. H. and Jiang, Q., 2005, "Size-Dependent Surface Tension and Tolman's Length of Droplets," *Langmuir*, **21**(2), pp. 779-781.

[72] Saxena, S. C. and Joshi, R. K., 1981, *Thermal Accommodation and Adsorption Coefficients of Gases*, McGraw-Hill Book Company.

[73] Michelsen, H. A., 2009, "Derivation of a Temperature-Dependent Accommodation Coefficient for use in Modeling Laser-Induced Incandescence of Soot," *Appl. Phys. B*, **94**(1), pp. 103-117.

[74] Daun, K. J., Smallwood, G. J., and Liu, F, 2008, "Investigation of Thermal Accommodation Coefficients in Time-Resolved Laser-Induced Incandescence," *J. Heat Trans.*, **130**(12), No. 121201.

[75] Daun, K. J., Smallwood, G. J., and Liu, F., 2009, "Molecular Dynamics Simulations of Translational Thermal Accommodation Coefficients for Time-Resolved LII," *Appl. Phys. B*, **94**(1), pp. 39-49.

[76] Hu, L. and McGaughey, A. J. H., 2013, "Energy Accommodation between Noble Gases and Carbon Nanotubes," *J. Phys. Chem. C*, **117**(37), pp. 18804-18808.

[77] Li, J., Lu, Y., Ye, Q., Cinke, M., Han, J., Meyyappan, M., 2003, "Carbon Nanotube Sensors for Gas and Organic Vapor Detection," *Nano Lett.*, **3**(7), pp. 929-933.

[78] Modi, A., Koratkar, N., Lass, E., Wei, B., Ajayan, P.M., 2003, "Miniaturized gas ionization sensors using carbon nanotubes," *Nature*, **424**(6945), pp. 171-174.

[79] Kinefuchi, I. et al., 2013, "Gas−Surface Energy Exchange in Collisions of Helium Atoms with Aligned Single-Walled Carbon Nanotube Arrays.," *J. Phys. Chem.*, **117**(27), pp. 14254-14260.

[80] Dillon, A. C. et al., 1997, "Storage of Hydrogen in Single-walled Carbon Nanotubes," *Nature*, **386**(6623), pp. 377-379.

[81] Liu, C. et al., 1999, "Hydrogen Storage in Single-Walled Carbon Nanotubes at Room Temperature," *Science*, **286**(5442), pp. 1127-1129.

[82] Zhu, W. et al., 1999, "Current Density from Carbon Nanotube Field Emitters," *Appl. Phys. Lett.*, **75**(6), pp. 873-875.

[83] Allen, M. P. and Tildesley, D. J., 1989, *Computer Simulation of Liquids*, Clarendon Press.

[84] Lümmen, N. and Kraska, T., 2004, "Investigation of the Formation of Iron Nanoparticles from the Gas Phase by Molecular Dynamics Simulation," *Nanotechnology*, **15**(5), pp. 525-533.

[85] Chirita, V., Pailthorpe, B., and Collins, R., 1993, "Molecular Dynamics Study of Low-Energy Ar Scattering by the Ni (001) Surface," *J. Phys. D: Appl. Phys.*, **26**(1), pp. 133-142.

[86] Cheng, Y.Y. and Lee, C.C., 2009, "Molecular Dynamics Simulations of Argon Cluster Impacts on a Nickel Film Surface," *Nucl. Instrum. Methods Phys. Res., Sect. B*, **267**(8), pp. 1428-1431.

[87] Delhommelle, J. and Millié, P., 2001, "Inadequacy of the Lorentz-Berthelot Combining Rules for Accurate Predictions of Equilibrium Properties by Molecular Simulation," *Mol. Phys.*, **99**(8), pp. 619-625.

[88] Bodaa, D. and Henderson, D., 2008, "The Effects of Deviations from Lorentz–Berthelot Rules on the Properties of a Simple Mixture," *Mol. Phys.*, **106**(20), pp. 2367-2370.

[89] Forsman, Jan and Woodward, Clifford E., 2010, "Limitations of the Derjaguin Approximation and the Lorentz-Berthelot Mixing Rule," *Langmuir*, **26**(7), pp. 4555–4558.

[90] Chase, D. et al., 2000, "Argon Scattering from Liquid Indium: Simulations with Embedded Atom Potentials and Experiment," *J. Chem. Phys.*, **113**(20), pp. 9279-9287.

[91] Blaha, P. et al., 2001, *WIEN2k: An Augmented Plane Wave plus Local Orbitals Program for Calculating Crystal Properties*, Techn. Universitat, Wien.

[92] Perdew, J.P., Burke, K., and Ernzerhof, M., 1996, "Generalized Gradient Approximation Made Simple," *Phys. Rev. Lett.*, **77**(18), pp. 3865-3868.

[93] Frenkel, D. and Smit, B., 2002, *Understanding Molecular Simulation: From Algorithms to Applications*, Academic Press, San Diego.

[94] Swope, W.C. et al., 1982, "A Computer Simulation Method for the Calculation of Equilibrium Constants for the Formation of Physical Clusters of Molecules: Application to Small Water Clusters," *J. Chem. Phys.*, **76**(1), pp. 637-648.

[95] Berendsen, H. J. C. et al., 1984, "Molecular-Dynamics with Coupling to an External Bath," *J. Chem. Phys.*, **81**(8), pp. 3684-3690.

[96] Hünenberger, P. H., 2005, "Thermostat Algorithms for Molecular Dynamics Simulations," *Adv. Polym. Sci.*, **173**, pp. 105-149.

[97] Koopman, E. A. and Lowe, C. P., 2006, "Advantages of a Lowe-Andersen Thermostat in Molecular Dynamics Simulations," *J. Chem. Phys.*, **124**(20), No. 204103.

[98] Någård, M.B. et al., 1998, "Scattering and Trapping Dynamics of Gas-Surface Interactions: Theory and Experiments for the Xe-Graphite System," *J. Chem. Phys.*, **109**(23), pp. 10339-10349.

[99] Lennard-Jones, J. E., 1924, "On the Determination of Molecular Fields," *Proc. R. Soc. Lond. A*, **106**(738), pp. 463-477.

[100] Steele, W.A., 1978, "The Interaction of Rare Gas Atoms with Graphitized Carbon Black," *J. Phys. Chem.*, **82**(7), pp. 817-821.

[101] Bojan, M.J. and Steele, W.A., 1987, "Interactions of Diatomic Molecules with Graphite," *Langmuir*, **3**(6), pp. 1123-1127.

[102] Peters, C. and Klein, M., 1985, "Monte Carlo Calculations for Solid CO and N2 Overlayers," *Mol. Phys.*, **54**(4), pp. 895-909.

[103] Leinböck, B. et al., 2000, "Orientational Ordering of N2O Molecules Adsorbed on Graphite (0 0 0 1): A Novel Commensurate Pinwheel Structure," *Phys. Rev. Lett.*, **84**(9), pp. 1954-1957.

[104] Zhao, X. and Johnson, J.K., 2005, "An Effective Potential for Adsorption of Polar Molecules on Graphite," *Mol. Simulat.*, **31**(1), pp. 1-10.

[105] Vidal-Madjar, C. and Minot, C., 1987, "Adsorption Potential of Alkanes on Graphite," *J. Phys. Chem.*, **91**(15), pp. 4004-4011.

[106] Daun, K. J., Titantah, J. T., and Karttunen, M., 2013, "Erratum to: Molecular Dynamics Simulation of Thermal Accommodation Coefficients for Laser-Induced Incandescence Sizing of Nickel Particles," *App. Phys. B*, **112**(4), pp. 599-600.

[107] Sutton, A. P. and Chen, J., 1989, "Long-Range Finnis–Sinclair Potentials," *Phil. Mag. Lett.*, **61**(3), pp. 139-146.

[108] Rafii-Tabar, H. and Sulton, A. P., 1991, "Long-Range Finnis-Sinclair Potentials For F.C.C. Metallic Alloys," *Phil. Mag. Lett.*, **63**(4), pp. 217-224.

[109] Casimir, H. and Polder, D., 1948, "The Influence of Retardation on the London-Van Der Waals Forces," *Phys. Rev.*, **73**(4), pp. 360-372.

[110] Çagin, T. et al., 1999, "Bulk Metallic Glasses," *MRS Symposia Proceedings*, **554**, pp. 43-48.

[111] Qi, Y. et al., 1999, "Molecular-Dynamics Simulations of Glass Formation and Crystallization in Binary Liquid Metals: Cu-Ag and Cu-Ni," *Phys. Rev. B*, **59**(5), p. 3527.

[112] Finnis, M. W. and Sinclair, J. E., 1984, "A Simple Empirical N-Body Potential for Transiation Metals," *Phis. Mag. A*, **50**(1), pp. 45-55.

[113] Finnis, M. and Sinclair, J., 1986, "Erratum," *Phil. Mag. A*, **53**(1), p. 161.

[114] Shibuta, Y. and Suzuki, T., 2008, "A Molecular Dynamics Study of the Phase Transition in BCC Metal Nanoparticles," *J. Chem. Phys.*, **129**(14), No. 144102.

[115] Goodman, F. O. and Wachman, H. Y., 1976, *Dynamics of Gas-Surface Scattering*, Academic Press, New York.

[116] Rodriguez, A. W., Capasso, F., and Johnson, S. G., 2011, "The Casimir Effect in Microstructured Geometries," *Nature Photon.*, **5**(4), pp. 211-221.

[117] Kao, C. L., Carlsson, A., and Madix, R. J., 2004, "Mass and Lattice Effects in Trapping: Ar, Kr, and Xe on Pt(1 1 1), Pd(1 1 1), and Ni(1 1 1)," *Surf. Sci.*, **565**(1), pp. 70-80.

[118] Trapnell, B. M. W. and Hayward, D. O, 1955, *Chemisorption*, Butterworth, London.

[119] Gundry, P. M. and Tompkins, F. C., 1960, "Chemisorption of Gases on Metals," *Q. Rev. Chem. Soc.*, **14**(3), pp. 257-291.

[120] Vidali, G. et al., 1991, "Potentials of Physical Adsorption," *Surf. Sci. Rep.*, **12**(4), pp. 135–181.

[121] Titantah, J. et al., 2006, "The Effect of Hydrogen on the Electronic and Bonding Properties of Amorphous Carbon," *J. Phys.: Cond. Matt.*, **18**(48), No. 10803.

[122] Titantah, J. T. et al., 2009, "Bond length variation in Ga1−xInxAs crystals from the Tersoff potential," *J. Appl. Phys.*, **101**(12), No. 123508.

[123] Hedin, L., 1965, "New Method for Calculating the One-Particle Green's Function with Application to the Electron-Gas Problem," *Phys. Rev.*, **139**(3), pp. 796-823.

[124] Grimme, S., 2004, "Accurate Description of Van Der Waals Complexes by Density Functional Theory Including Empirical Corrections," *J. Comput. Chem.*, **25**(12), pp. 1463-1473.

[125] Plimpton, S., 1995, "Fast Parallel Algorithms for Short-Range Molecular Dynamics," *J. Comput. Phys.*, **117**(1), pp. 1-19.

[126] Stillinger, F. H. and Weber, T. A., 1985, "Computer Simulation of Local Order in Condensed Phases of Silicon," *Phys. Rev. B: Condens. Matter*, **31**(8), pp. 5263-5270.

[127] Dozhdikov, V. S., Basharin, A. Y., and Levashov, P. R., 2012, "Two-Phase Simulation of the Crystalline Silicon Melting Line at Pressures from –1 to 3 GPa," *J. Chem. Phys.*, **137**(5), p. 054502.

[128] Rhim, W. K. and Ohsaka, K., 2000, "Thermophysical Properties Measurement of Molten Silicon by High-Temperature Electrostatic Levitator: Density, Volume Expansion, Specific Heat Capacity, Emissivity, Surface Tension and Viscosity," *J Cryst. Growth*, **208**(1), pp. 313-321.

[129] Sipkens, T. et al., 2013, "Sizing of Molybdenum Nanoparticles using Time-Resolved Laser-Induced Incandescence," *J. Heat Transfer*, **135**(5), No. 052401.

[130] Matthies, H. G., 2007, *Extreme Man-Made and Natural Hazards in Dynamics of Structures*, Springer, pp. 105-135.

[131] Kiureghian, A. D. and Ditlevsen, O., 2007, "Aleatory or epistemic? Does it matter?," *Special Workshop on Risk Acceptance and Risk Communication*, Stanford.

[132] Kennedy, M. C. and O'Hagan, A., 2001, "Bayesian Calibration of Computer Models," *J. R. Statist. Soc. B*, **63**(3), pp. 425-464.

[133] Roth, P. and Filippov, A. V., 1996, "In Situ Ultrafine Particle Sizing by a Combination of Pulsed Laser Heatup and Particle Thermal Emission," *J. Aerosol Sci.*, **27**(1), pp. 95-104.

[134] Twomey, S., 1977, *Introduction to the Mathematics of Inversion in Remote Sensing and Indirect Measurement*, Elesvier, Amsterdam.

[135] Markowski, G. R., 1987, "Improving Twomey's Algorithm for Inversion of Aerosol Measurement Data," *Aerosol Sci. Technol.*, **7**(2), pp. 127-141.

[136] Charnigo, R. et al., 2012, "Credible Intervals for Nanoparticle Characteristics," *J. Quant. Spectrosc. Radiat. Transfer* , **113**(2), pp. 182-193.

[137] Yariv, A., 1971, *Introduction to Optical Electronics*, Holt, Rinehart, and Winston, Inc., New York, NY.

[138] Levenberg, K., 1944, "A Method for the Solution of Certain Problems in Least Squares," *Quart. Appl. Math.*, **2**, pp. 164-168.

[139] Marquardt, D., 1963, "An Algorithm for Least-Squares Estimation of Nonlinear Parameters," *SIAM J. Appl. Math.*, **11**(2), pp. 431-441.

[140] Chen, M. H. and Shao, Q. M., 1999, "Monte Carlo Estimation of Bayesian Credible and HPD Intervals," *J. Comp. Graph. Stat.*, **8**(1), pp. 69-92.

[141] Hyndman, R. J., 1996, "Computing and Graphing Highest Density Regions," *Am. Stat.*, **50**(2), pp. 120-126.

[142] Fox, J., 2008, *Applied Regression Analysis and Generalized Linear Models*, 2nd ed., Sage Publications.

[143] Wu, C. F. J., 1986, "Jackknife, Bootstrap and Other Resampling Methods in Regression Analysis," *Ann. Stat.*, **14**(4), pp. 1261-1295.

[144] Crosland, B.M., Johnson, M.R., and Thomson, K.A., 2011, "Analysis of Uncertainties in Instantaneous Soot Volume Fraction Measurements using Two-Dimensional, Auto-Compensating, Laser-Induced Incandescence (2D-AC-LII)," *Appl. Phys. B*, **102**(1), pp. 173-183.

[145] Hinds, W. C., 1982, *Aerosol Technology: Properties, Behaviour, and Measurement of Airborne Particles*, John Wiley and Sons, New York.

[146] Holland, P. W. and Welsch, R. E., 2007, "Robust Regression using Iteratively Reweighted Least-Squares," *Commun. Stat. Theory*, **6**(9), pp. 813-827.

[147] Juenker, D. W., Leblanc, L. J., and Martin, C. R., 1968, "Optical Properties of Some Transition Metals," *J. Opt. Soc. Am.*, **58**(2), pp. 164-171.

[148] Price, D. J., 1947, "The Temperature Variation of the Emissivity of Metals in the Near Infra-Red," *Proc. Phys. Soc.*, **59**(1), pp. 131-138.

[149] Paradis, P. F., Ishikawa, T., and Nosaka, Y., 2002, "Noncontact Measurements of Thermophysical Properties of Molybdenum at High Temperatures," *Int. J. Thermophys.*, **23**(2), pp. 555-569.

[150] Nunomura, S., Yoshida, I., and Kondo, M., 2009, "Time-Dependent Gas Phase Kinetics in a Hydrogen Diluted Silane Plasma," *Appl. Phys. Lett.*, **94**(7), p. 071502.

[151] Liu, F. et al., "Effects of Primary Soot Particle Size Distribution on the Temperature of Soot Particles Heated by a Nanosecond Pulsed Laser in an Atmospheric Laminar Diffusion Flame," *Int. J. Heat Mass Transfer*, **49**(3), pp. 777-778.

[152] Cook, D. R. and Weisberg, S., 1982, *Residuals and Influence in Regression*, Chapman and Hall, New York.

[153] Wooldridge, M. S., 1998, "Gas-Phase Combustion Synthesis of Particles," *Prog. Energy Combust. Sci.*, **24**(1), pp. 63-87.

[154] Petermann, N. et al., 2011, "Plasma Synthesis of Nanostructures for Improved Thermoelectric Properties," *J. Phys. D: Appl. Phys.*, **44**(17), p. 174034.

[155] Knipping, J. et al., 2004, "Synthesis of High Purity Silicon Nanoparticles in a Low Pressure Microwave Reactor," *J. Nanosci. Nanotechnol.*, **4**(8), pp. 1039-1044.

[156] Kortshagen, U., Mangolini, L., and Bapat, A., 2007, "Plasma Synthesis of Semiconductor Nanocrystals for Nanoelectronics and Luminescence Applications," *J. Nanoparticle Research*, **9**(1), pp. 39-52.

[157] Snelling, D. R. et al., 2005, "A Calibration-Independent Laser-Induced Incandescence Technique for Soot Measurement by Detecting Absolute Light Intensity," *Applied Optics*, **44**(31), pp. 6773-6785.

[158] Brunauer, S., Emmett, P. H., and Teller, E., 1938, "Adsorption of Gases in Multimolecular Layers," *J. Am. Chem. Soc.*, **60**(2), pp. 309-319.

[159] Hackley, V. A. and Stefaniak, A. B., 2013, ""Real-World" Precision, Bias, and Between-Laboratory Variation for Surface Area Measurement of a Titanium Dioxide Nanomaterial in Powder Form," *J. Nanopart. Res.*, **15**(6), p. 1742.

[160] Shvarev, K. M., Baum, B. A., and Gel'd, P. V., 1975, "Optical Properties of Liquid Silicon," *Sov. Phys. Solid State*, **16**(11), pp. 2111-2112.

[161] Li, K. D. and Fauchet, P. M., 1987, "Picosecond Determination of the Dielectric Function of Liquid Silicon at 1064 nm," *Solid State Commun.*, **61**(3), pp. 207-209.

[162] Li, K. D. and Fauchet, P. M., 1987, "Drude Parameters of Liquid Silicon at the Melting Temperature," *Appl. Phys. Lett.*, **51**(21), pp. 1747-1749.

[163] Desai, P. D., 1985, "Thermodynamic Properties of Iron and Silicon," *J. Phys. Chem. Ref. Data*, **15**(3), pp. 967-983.

[164] Hecht, C. et al., 2011, "Gas-Temperature Imaging in a Microwave-Plasma Nanoparticle-Synthesis Reactor Using Multi-Line NO-LIF Thermometry," *Z. Phys. Chem.*, **225**(11-12), pp. 1225-1235.

[165] Švrček, V. et al., 2008, "Blue Luminescent Silicon Nanocrystals Prepared by Nanosecond Laser Ablation and Stabilized in Electronically Compatible Spin on Glasses," *J. Appl. Phys.*, **103**(2), No. 023101.

[166] Dean, J. A., 1999, *Lange's Handbook of Chemistry*, 15th ed., McGraw-Hill.

[167] Press, W. H. et al., 2007, *Numerical Recipes: The Art of Scientific Computing*, 3rd ed., Cambridge University Press, Cambridge, UK.

[168] Bowman, A. W. and Azzalini, A., 1997, *Applied Smoothing Techniques for Data Analysis*, Oxford University Press, Oxford, UK.

[169] Liu, Y. et al., 2005, "TCE Dechlorination Rates, Pathways, and Efficiency of Nanoscale Iron Particles with Different Properties," *Environ. Sci. Tech.*, **39**(5), pp. 1338-1345.

[170] He, F. and Zhao, D., 2007, "Manipulating the Size and Dispersibility of Zerovalent Iron Nanoparticles by use of Carboxymethyl Cellulose Stabilizers," *Environ. Sci. Technol.*, **41**(17), pp. 6216-6221.

[171] Phenrat, T et al., 2009, "Particle Size Distribution, Concentration, and Magnetic Attraction Affect Transport of Polymer-modified Fe0 Nanoparticles in Sand Columns," *Environ. Sci. Technol.*, **43**(13), pp. 5079-5085.

[172] Vander Wal, R. L., 2009, "Laser-Induced Incandescence: Excitation and Detection Conditions, Material Transformations and Calibration," *Appl. Phys. B*, **96**(4), pp. 601-611.

[173] Johnson, P. B. and Christy, R. W., 1974, "Optical Constants of Transition Metals: Ti, V, Cr, Mn, Fe, Co, Ni, and Pd," *Phys. Rev. B*, **9**(12), pp. 5056-5070.

[174] Hixson, R. S., Winkler, M. A., and Hodgdon, M. L., 1990, "Sound Speed and Thermoyhysical Properties of Liquid Iron and Nickel," *Phys. Rev. B*, **42**(10), pp. 6485-6491.

[175] Drotning, W. D., 1981, "Thermal Expansion of Iron, Cobalt, Nickel, and Copper at Temperatures up to 600 deg K Above Melting," *High Temp. High Pressures*, **13**(4), pp. 441-458.

[176] Young, D. A. and Alder, B. J., 1971, "Critical Point of Metals from the van der Waals Model," *Phys. Rev. A*, **3**(1), pp. 364-371.

[177] Kline, S. J. and McClintock, F. A., 1953, "Describing Uncertainties in Single-Sample Experiments," *ASME Mechanical Engineering*, **75**(1), pp. 3–8.

[178] Eremin, A., Gurentsov, E., and Yurischev, M., 2014, "Mo Nanoparticle Sizing by Ti-Re LII and TEM," *6th International Workshop and Meeting on Laser-Induced Incadescence*, Ven, Sweden.

[179] Gelman, A., Gilks, W. R., and Roberts, G. O., 1997, "Weak Convergence and Optimal Scaling of Random Walk Metropolis Algorithms," *Ann. Appl. Probab.*, **7**(1), pp. 110-120.